Functional materials derived from block copolymer self-assembly

Li, Tao

Publication date:
2015

Document Version
Publisher's PDF, also known as Version of record

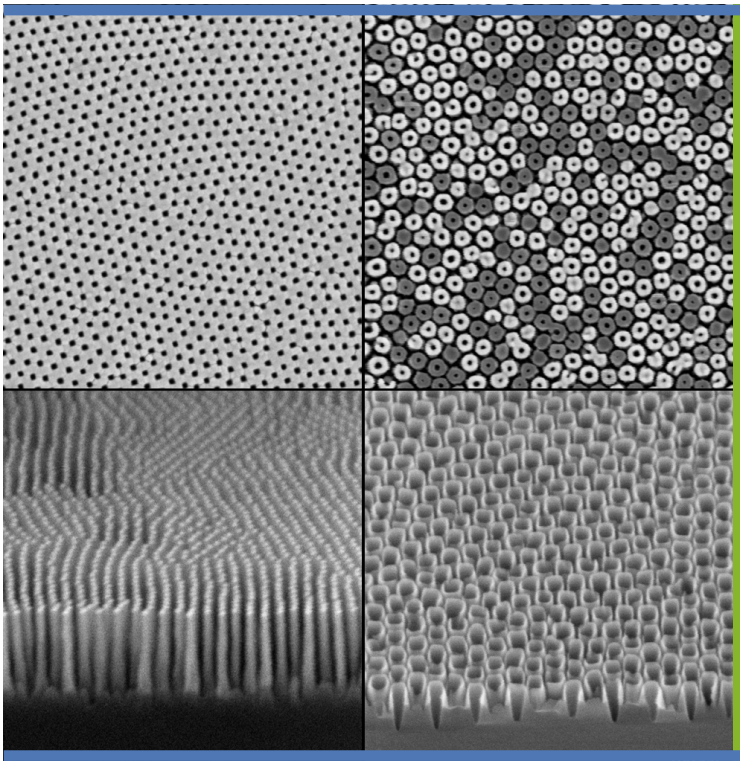

Functional materials derived from block copolymer self-assembly

Tao Li
PhD Thesis October 2015

DTU Nanotech
Department of Micro- and Nanotechnology

Functional materials derived from block copolymer self-assembly

Tao Li

Ph.D. Thesis

October 2015

Department of Micro- and Nanotechnology

Abstract

The main objective of this project is to explore block copolymer self-assembly for generating functional materials with well-defined morphology on sub-20 nanometer length scale, which can be utilized in many important applications such as solar cells and nanolithography.

One of the specific targets is to fabricate interconnected and highly ordered metal oxide films by using a nano-porous polymer with gyroid morphology as the template. This unique structure is ideal for the solar cell application where a mesoscopic metal oxide scaffold functions as the electron collection and transport material. Two deposition methods, namely nanocasting and atomic layer deposition (ALD) will be applied to fabricate compact, inter-connected, and continuous metal oxide films. In this way, the structure integrity will be preserved after template removal during the annealing procedure.

Another objective of this project is to employ block copolymer (BC) self-assembly for nanolithography. We present a procedure that significantly simplifies the main stream BC lithography process, showing a broad substrate tolerance and allowing for efficient pattern transfer. The masks are directly applied on substrates with broadly varying surface energy, including polymers, silicon and graphene, thus bypassing the laborious and delicate substrate chemical pre-modification. To push the boundary even further for minimal lithography steps, a scalable ultra-fast block copolymer lithography procedure is developed. Using selective solvent spin-casting, the block copolymer self-organizes into monolayer packed sphere pattern, without any surface treatment of the substrate and annealing process. Arrays of nano-pillars and nano-wells of various materials are fabricated in dry etch processes over wafer scale without defects. We also show an in situ Al_2O_3 hard mask formation process by ALD to obtain high aspect ratio nanostructured silicon.

This Ph.D. project has led to fruitful scientific contributions and technological developments, which have already allowed to initiate several collaborations with other research groups at DTU Nanotech and DTU Photonics. We believe this project opens up for a number of strategies aiming at the creation of high-performance functional materials on the length scale of sub-20 nanometers that cannot be manufactured in an easy fashion by conventional top-down lithography methods.

Dansk resumé

Hovedformålet med dette projekt er at udforske blok copolymer selv-organisering til at generere funktionelle materialer med veldefineret morfologi på sub-20 nanometer længdeskala, som kan udnyttes i mange vigtige applikationer såsom solcelle og nanolithography.

Et af de specifikke mål er at fremstille co-kontinuerlige og vel ordnede metaloxid-film ved hjælp af en nanoporøse polymer med gyroid morfologi som 'skabelon'. Denne unikke struktur er ideel som materiale for solceller hvor den mesoskopiske metaloxid fungerer som elektron indsamling og transport medium. To deponerings metoder, nemlig nanocasting og atomic layer deposition (ALD) vil blive anvendt til at fabrikere kompakte, co-kontinuerlige og selvstående metaloxid film. På denne måde vil strukturens integritet bevares efter polymerskabelonens fjernelse under annealing processen.

Et andet formål med dette projekt er at udnytte blok copolymer (BC) selv-organisering for fremstilling af masker til nanolitografi. Vi præsenterer en procedure som væsentligt simplificerer de mest anvendte BC litografi processer; samtidigt viser vores proces en bred tolerance overfor den kemiske komposition af substratet og giver mulighed for en effektiv overførsel af nano-mønstrene til substratet. Maskerne er lagt direkte ovenpå substrater med bredt varierende overflade energi, herunder polymerer, silicium og graphene. Dermed undgås den komplicerede og delikate, men bredt anvendt mellemtrin af substratets kemiske overflade modifikation. Vi har også udviklet en ultrahurtig BC litografi procedure, ved at reducere til minimum antallet af de anvendte procestrin. Metoden er fuld skalerbar. Ved at bruge selektive opløsningsmidler i spin-casting trinet, blok copolymeren spontant danner et mønster af sfærer pakket i enkelt lag, uden nogen form for overfladebehandling af substratet eller annealing. Denne film bruges som litografimaske for at fremstille arrays af nano-søjler og nano-brønde af forskellige materialer vha. tørre ætse processer.

Dette Ph.D. projekt har ført til frugtbare videnskabelige og teknologi-relevante resultater, som har allerede tilladt at indlede flere samarbejder med andre forskningsgrupper på DTU Nanotech og DTU Fotonik. Vi mener, at dette projekt åbner op for en række strategier, der sigter mod at skabe højt ydende funktionelle materialer på sub-20 nanometer længdeskala som ikke kan fremstilles på en nem måde ved hjælp af konventionelle top-down litografi metoder.

Acknowledgement

First of all, I would like to thank my supervisor – Sokol Ndoni who gave me the unique opportunity to join his group and work in the superb scientific environment provided by DTU nanotech, CEN and Danchip. Whenever I need help, he always does his best to walk me through with endless patience and support. I am also deeply grateful for his constant encouragement and inspiration on my project.

Many thanks to my co-supervisor - Ole Hansen who guilds me over the solar cell research and dry etch process. These hands-on experiences greatly help me to understand the area I am not very familiar with at the early stage. And also Thomas Peterson provides me with the Pyrex substrates and gives me the help for the catalysis experiment design.

Special thanks to my colleague Lar Schulte who synthesized all the polymers I need in this project with high quality. I simply cannot make my research without his help. Not only that, he also teaches me how to process the BCP, makes membranes, sets up electrodeposition, measures solvent uptake by QCM, translates Danish, et al.

Thanks to all the members in the group of self-organized materials: Lotte Nielson, Sozaraj Rasappa and Zhongli Wang. Zhongli helps a lot in the project of the BCP nanolithography, especially with the AFM measurements. I wish you all success in your career!

This thesis is the results of my Ph.D. work carried out at DTU Nanotech at Lyngby campus from 2013 to 2015. I would also like to express my gratitude to the department financial support and superb facility in DTU. I also want to thank all the employees in our department because everyone is very willing to help each other, making my work enjoyable.

In my last Ph.D. stage, my work leads to several on-going collaborations. First I want to thank to Elizaveta Semenova and Artem Shikin on developing quantum dots photonic devices using my BCP lithography technique; second to Rafael Taboryski and Agnieszka Telecka on making mold for polymer injection; third to Kaiyu Wu on SERS substrate made by nanostructured silicon. These projects just get started but already show very promising results. I wish we can make great results in the near future.

Last but not least, I would like to thank for my parents and friends for their support and for being there for me all these years.

Tao Li

September 2015

List of Abbreviation

AFM	Atomic force microscopy
ALD	Atomic layer deposition
BCP	Block copolymer
BET	Brunauer–Emmett–Teller
CEN	Center for Electron Nanoscopy
CPTO	Cyclopentanone
DCP	Dicumyl peroxide
EDS	Energy-dispersive X-ray spectroscopy
FTO	Fluorine-doped tin oxide
ICP	Inductively coupled plasma
ITO	Indium-doped tin oxide
Mn	Molecular weight
NMR	Nuclear magnetic resonance
ODT	Order to disorder transition
P2VP	polystyrene-block-poly(2-vinylpyridine)
P4VP	polystyrene-block-poly(4-vinylpyridine)
PB	Poly-butadiene
PDI	Poly dispersive index
PDMS	Polydimethylsiloxane
PEO	Polyethylene oxide
PLA	Polylactide
PMMA	Poly(methyl methacrylate)
PS	Polystyrene
PSF	Polysulfone
QCM	Quartz crystal microbalance
RIE	Reactive ion etching
SD	PS-PDMS
SEC	Size exclusion chromatography
SEM	Scanning electron microscopy
SERS	Surface-enhanced Raman spectroscopy
TBAF	Tetra-n-butylammonium fluoride
TEM	Transmission electron microscopy
THF	Tetrahydrofuran
TMPA	2,2,4-Trimethylpentane
TMPE	2,4,4-Trimethyl-1-pentene
XPS	X-ray photoelectron spectroscopy
XRD	X-ray powder diffraction

Contents

Chapter 1

General introduction

1.1 Scope & outline

Generally speaking, nanotechnology refers to a scientific and technological area concerning the manufacture, characterization and utilization of materials with nanometer scale. Of special interest are nanostructured functional materials, can be found in all materials classes from polymers over metals to ceramics and composites, with a well-defined morphology in feature size ranging from 10 nm to 50 nm. Nanostructured materials at this length scale can show improved particular properties such as quantum effects.

So far, top-down lithography processes dominate the fabrication of nano-structured materials with a well-defined morphology. Nano-imprint, electron beam lithography, deep UV and interference lithography are widely used in scientific and industrial areas. However, most of these techniques suffer from low throughput, or high cost.

As a contrast, bottom-up processes taking advantage of self-organized materials has attracted increasing attention, as an alternative solution to these problems. Particularly, di-block copolymers consisting of two immiscible polymer blocks can self-assemble into various morphologies with well-defined structural characteristics. In the past decades, growing research on this subject has been perfomred.

The aim of this thesis is to explore the potential of block copolymers for making functional materials with well-defined morphology. Two approaches are proved to be effective, namely templated nanoporous polymer for 3D inorganic materials and block copolymer nanolithography. In this chapter, the block copolymer self-assembly is firstly reviewed. And then the background of the two approaches is given in details.

Chapter 2 summarizes the work of making 3D functional materials from gyroid polymer template. The unique property of the nanoporous template, namely cross-linked polybutadiene, provides an excellent platform for many novel processes where the traditional polymers fail. As results, a facile process is developed to make gyroid TiO_2 and SnO_2 by melt infiltration of block copolymer templates. Besides that, atomic layer deposition and direct oxygen plasma etching also show potential of fabrication of 3D functional materials.

Chapter 3 introduces an effective solvent vapor annealing procedure to make in sit mask directly on various substrates. Pattern transfers on these substrates are presented including common polymers, silicon and graphene. This approach shows unparalleled simplicity and applicability in block copolymer nanolithography.

Chapter 4 gives a scalable and fast block copolymer lithography process by selective solvent casting, in which sphere morphology is generated in less than 20 seconds. Pattern transfer is demonstrated by oxidized PDMS hard mask. And thus arrays of nano-pillars and nano-wells of various materials including polymers and silicon are fabricated over wafer scale without defects. An in situ Al_2O_3 hard mask formation process by atomic layer deposition to obtain high aspect ratio nanostructured silicon is given as well.

Chapter 5 concludes this Ph.D. project and gives future suggestions based on this work.

The overall thesis is based on the publication and the summited manuscripts in appendix.

1.2 Block copolymer self-assembly

A polymer is a large molecule, or macromolecule, consisting of many repeated subunits. Because of their broad range of properties, both synthetic and natural polymers play an essential and ubiquitous role in everyday life. Homo-polymers contain only a single type of monomer, while block copolymers are composed of two or more chemically distinct polymer chains connected at their ends via covalent bonds, as displayed in in Figure 1.1.

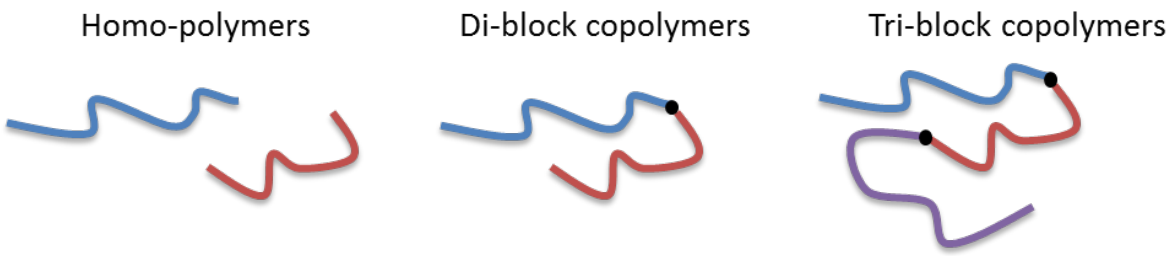

Fig. 1.1 Structural illustration of linear homo-polymers and block copolymers

Due to the collective compromise between the blocks' immiscibility and their constraint as parts of the same molecules, a block copolymer can self-assemble into structures on the nanometer scale. Even the simplest copolymer architecture, namely di-blocks, gives rise to the formation of a variety of highly ordered morphologies at length scale normally in the range of 5 - 50 nm, which is a typical length scale for a polymer coil.(*1*) As shown in Figure 1.2, an AB di-block copolymer can form the following four equilibrium morphologies: body-centered cubic spheres

(0D), hexagonally-packed cylinders (1D), lamellae (2D) or bi-continuous gyroid (3D) depending on the total block length, the composition of the blocks and the strength of interaction between the blocks.

The theory of BCP self-assembly is well-developed and successfully predicts the phase diagram of the equilibrium morphology of BCP bulk melts. Fig. 1.2, shows that an experimentally determined micro-phase diagram with the dependence of morphology on volume fraction of block A, f_A, where χ is the Flory-Huggins segmental interaction parameter, N is the total number of repeating units, or the degree of polymerization, and f is the volume fraction of one block. As χN exceeds a critical value, a disorder-to-order transition (ODT) will occur.(*2*) Below ODT, the AB diblock copolymer experiences transition through a body centered cubic spherical phase (BCC), a hexagonally packed cylindrical phase (HEX), a bi-continuous gyroid phase (GYR), and a lamellar phase (LAM). Here, χ is proportional to the unfavorable interactions between different blocks.

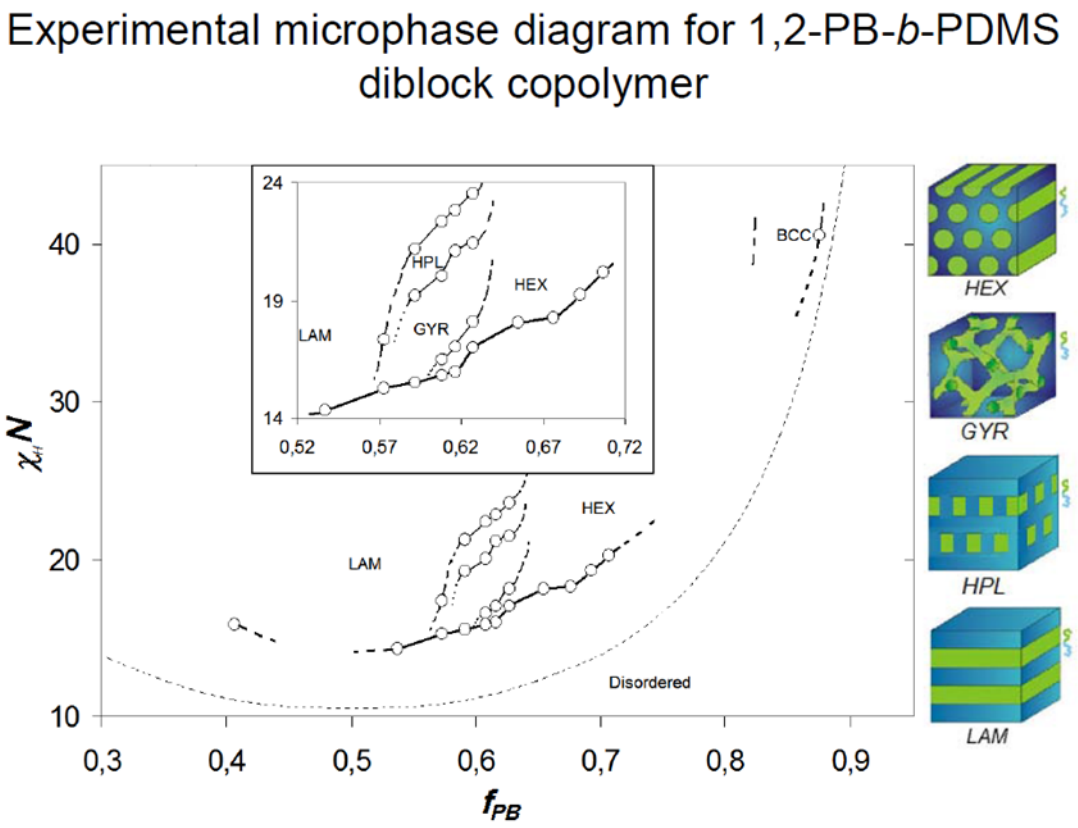

Figure 1.2 Schematic micro-phase diagram of linear di-block copolymers and representations of typical morphologies.

The equilibrium morphologies of block copolymers become more complex and diverse when the number of the blocks is increased.(*3*) For linear ABC triblock copolymers, the two composition variables and three interaction parameters greatly increase the range of morphological possibilities, some of the typical morphologies are illustrated in Figure 1.3.

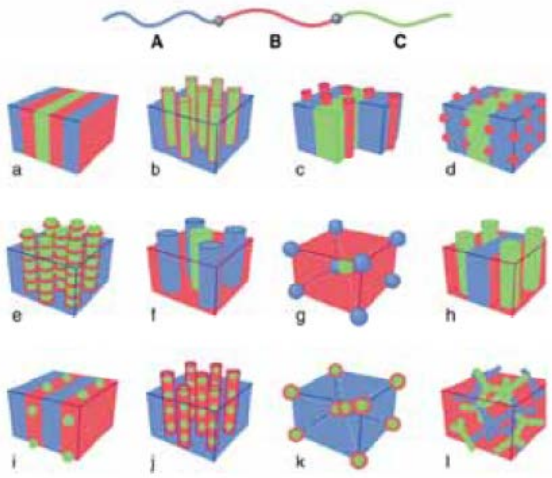

Figure 1.3 diversified morphologies from linear ABC triblock copolymers self-assembly.

Compared with homo-polymers, the synthesis of block copolymers is much more challenging to achieve good polydispersity index (PDI) with the desired composition. The difficulty of the preparation is increased with the increasing number of blocks. Generally they are synthesized via advanced polymerization technique such as living polymerization techniques, including living anionic or cationic polymerizations, atom transfer radical polymerization (ATRP), nitroxide-mediated controlled radical polymerization (NMRP), reversible addition-fragmentation chain transfer polymerization (RAFT) and ring opening metathesis polymerization (ROMP). (*4*, *5*) The solvent used in this type of synthesis has to be thoroughly cleaned. In addition to living polymerization techniques, a recently developed 'click chemistry' is extensively applied to couple two blocks to form di-block copolymers.

1.3 Block copolymers as templates for functional nanoporous materials

The self-organization of block copolymers can be exploited as a “bottom up” technique to create nano-structures for various applications. The most applicable approach of fabricating functional nanoporous materials is to replicate the nanoporous templates. The performance of the final product is dictated by the pore size, pore distribution, pore shape and morphology of the nanoporous templates. By far, a number of approaches for the fabrication of well-ordered materials have been created. Anodic aluminum oxide membrane (AAO) is firstly used to produce sub-micrometer wire arrays. (*6*) Zeolites have also been proved successful for the fabrication of microporous carbon. (*7*) Later on mesoporous silica monoliths have becoming the most popular template for nanocasting mesoporous materials.(*8, 9*) One of such an example is given in Fig. 1.4.

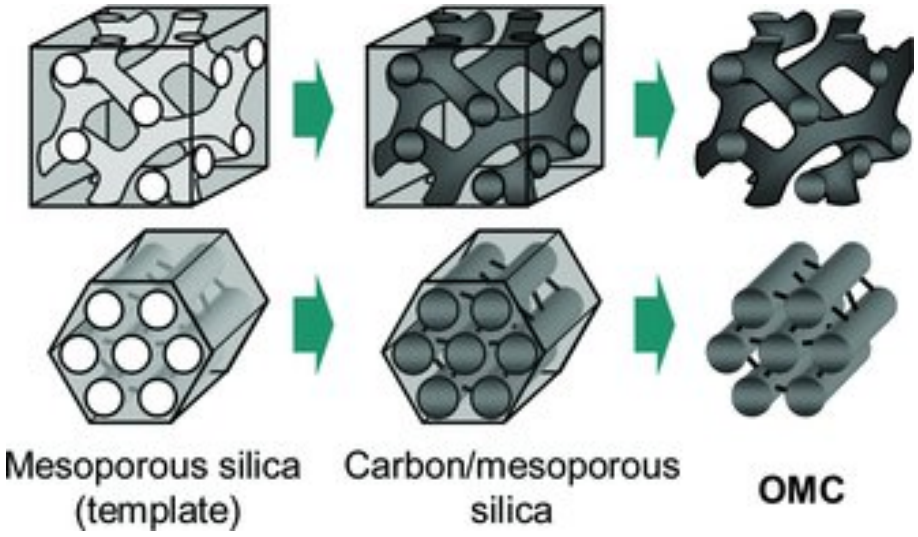

Figure 1.4. Synthesis schemes of two types of ordered mesoporous carbons (OMCs) from MCM-48 (upper) and SBA-15 (bottom), ref (*10*).

Another frequently used technique, so called “co-assembly”, utilizes amphiphilic molecules such as surfactants which contain both hydrophobic and hydrophilic domains. These molecules can co-assemble with the inorganic precursor into supra-molecules. The preferential interaction of one domain to the precursors, leads to the nano-hybrid materials with micro-phase separation, producing well-defined morphologies. The surfactant can be removed by calcination while the inorganic precursor turns into the final products. (*11*) This technique has been proved to be easy and versatile for nanoporous functional materials manufacture. (*12*) An example of co-assembly is shown in Fig. 1.5. However, since the surfactants compose the majority in the nano-hybrid, after the calcination, the remaining structure often suffers from deformation or collapse.

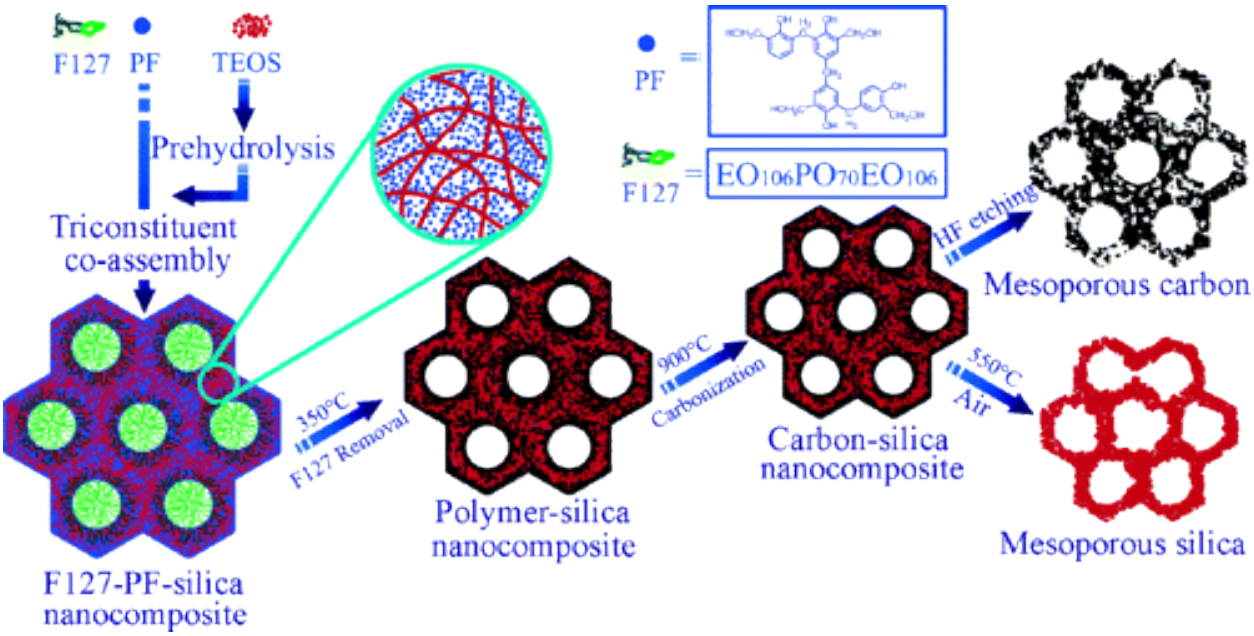

Figure 1.5. Tri-constituent co-assembly to ordered mesoporous polymer−silica and carbon−silica nanocomposites, and the corresponding ordered mesoporous silica and carbon frameworks, ref (*11*).

On the other hand, block copolymer assembly offers an elegant, cost-effective and environmentally sustainable approach to produce nanoporous templates due to their ability to self-organize into one-, two- and three-dimensional periodic nanostructures.(*3, 13, 14*) The pore size, pore distribution, pore shape and morphology can be controlled by the block copolymer precursor design such as molecular weight and composition.

The nanoporous polymer templates can be generated by selective removal of one block from self-organized block copolymer. So far, many experimental protocols have been developed to selectively degradation of one block, such as base or acid, ozone, UV, plasma etching and fluorine compounds. These methods are summarized in Table. 1.1. A typical example is the PS-PMMA system. (*15*) The PMMA block is degraded by UV irradiation while the PS block is cross-linked. The following acetic acid rinse washes away the degraded PMMA, leaving porous PS. Recently in our group, series of nanoporous PS, cross-linked PI and PB is successfully generated by selectively and quantitatively etching PDMS with anhydrous hydrogen fluoride or TBAF. (*16, 17*)

Table.1.1 Summary of reported techniques to selectively degrade one block of di-block copolymers.

BCP	Degrade method	Domain degraded	Ref
PS/PB-PDMS	HF TBAF in THF	PDMS PDMS	(*16, 17*)
PS-PEO	HI solution	PEO	(*18*)
PS-PI	Ozonolysis	PI	(*19*)
PS-PLA	NaOH solution	PLA	(*20*)
PS-PMMA	UV irradiation	PMMA	(*15*)

When the remaining nanoporous domain is used as template for replication, it is essential that this domain is continuous and self-supporting. And thus the most suitable microdomain structure adopted by di-block copolymer is the gyroid morphology which is co-continuous with high surface area to volume ratio. The most frequently used replication techniques include electrochemical deposition, atomic layer deposition (ALD), electroless plating, sol-gel reaction and melt infiltration using block copolymer as the template.

In an electrochemical deposition process, a thin layer of material, such as metals, ceramics and polymers, are coated on the substrates by electrochemical reduction in a solution. Fig. 1.6 demonstrates the transformation of nickel patterned in three-dimensional, highly interconnected, periodic gyroid morphology into a self-supporting nickel oxide array with hollow struts for high efficient electrochromic devices.

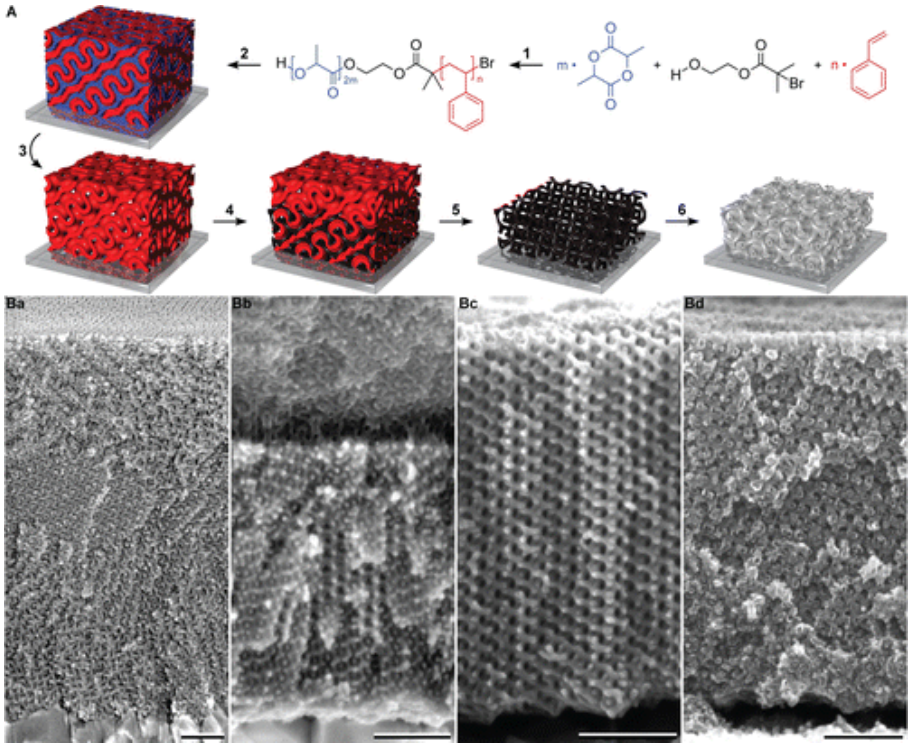

Figure 1.6. Preparation of a bicontinuous nickel oxide nanotubular array. (A) Schematic illustration of the six preparation steps: 1. Synthesis of polystyrene-*b*-poly(d,l-lactide) via atom transfer radical and organocatalytic ring-opening polymerization initiated by a bifunctional initiator. 2. Film deposition and microphase separation of PS-*b*-PLA into the DG morphology during temperature annealing. The red styrenic majority matrix encloses the blue interconnected lactide network. The front face shows the characteristic double wave pattern of the (211) plane. 3. Selective PLA removal yields a fully porous template on conducting FTO-coated glass. 4. Electrodeposition of Ni. 5. Dissolution of the polymer matrix exposes the freestanding Ni replica. 6. Thermal oxidation based on the results in a porous NiO nanotubular array with DG morphology. (B) Cross-sectional scanning electron micrographs (SEMs) of self-assembled voided DG polymer films (a), partially replicated template (b), freestanding Ni network (c), and NiO nanotube array (d). All scale bars are 200 nm. Ref: (*21*)

Electroless plating is also often used for this purpose, in which the metal ions in solution are reduced by a chemical reducing agent and deposit onto the substrates. Nickel and gold with a well-defined gyroid morphology are successfully fabricated by this method. (*22*, *23*) Well-defined multi-branched gold with surface plasmon resonance in near-infrared region from seeding growth approach using gyroid PS-PLA template are illustrated in Fig. 1.7.

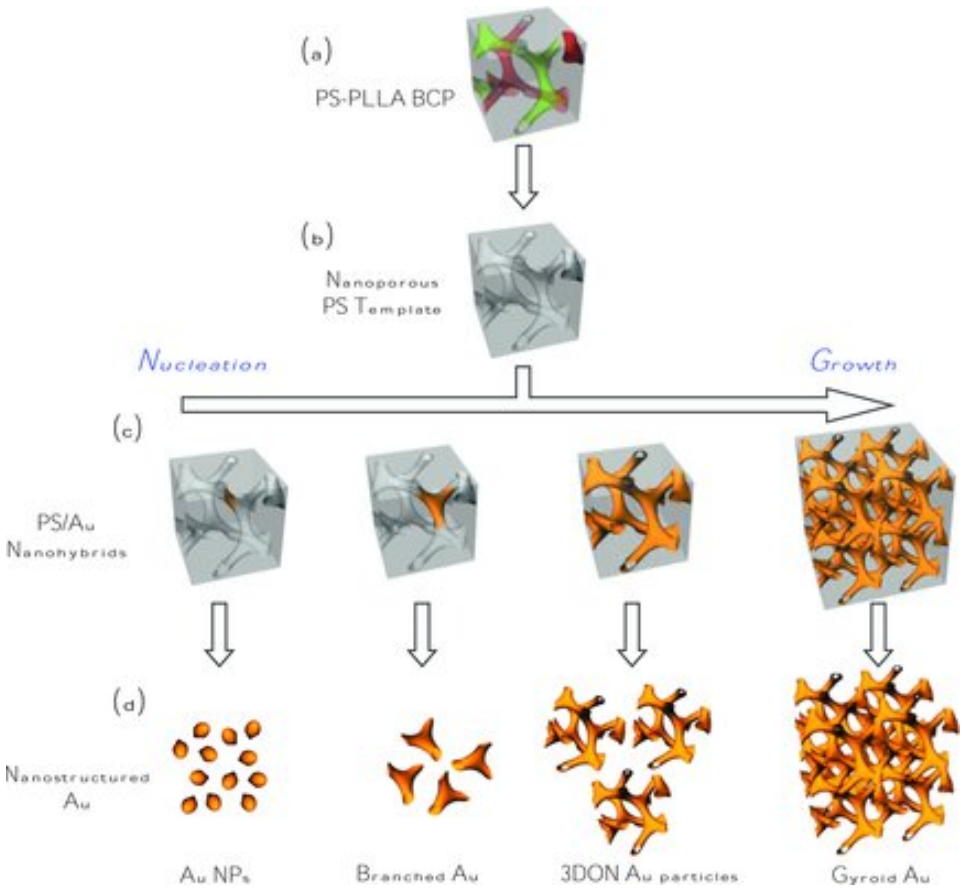

Figure 1.7. Schematic illustration for fabrication of well-defined nanostructured Au from BCP template: a) PS-PLLA DG phase (skeleton of DG structure with two identical networks (green and red)); b) Gyroid-forming nanoporous PS template after removal of PLLA network; c) PS/Au nanohybrids from controlled nucleation and growth of Au within the BCP template *via*seeding growth approach; d) Nanostructured Au after removal of PS template. Ref: (*23*)

ALD is based on the self-limiting and alternating surface reaction using at least two precursors in a sequential manner.(*24, 25*) This process allows uniform surface coating of high purity with angstrom thickness precision. (*25-28*) In ref (28), a method is developed for the robust and reliable synthesis of fully crystalline 3D mesoporous ZnO networks by means of ALD of ZnO into a self-assembled block copolymer template.

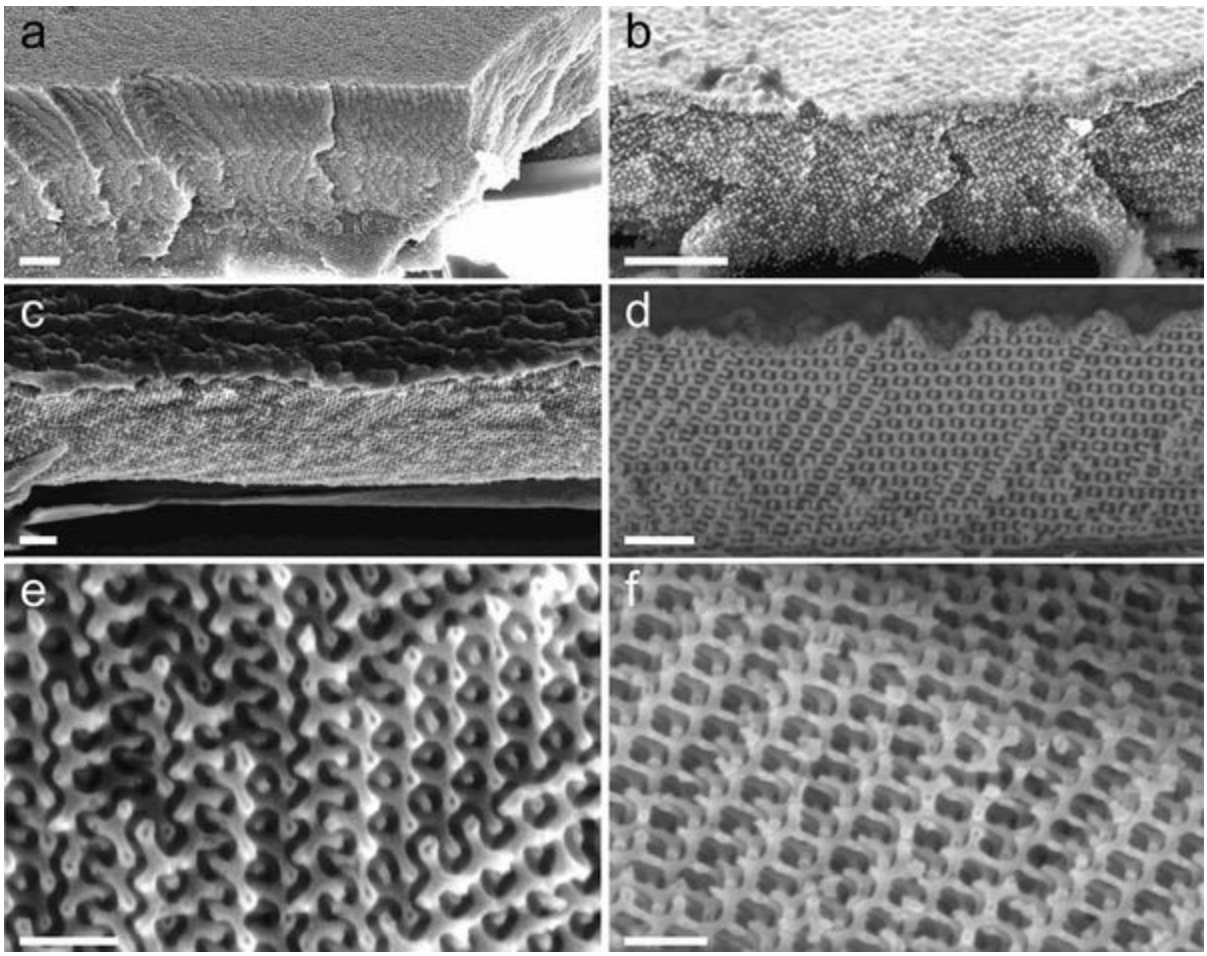

Figure 1.8. Side-view SEM images at a 45° angle of gyroid replication into ZnO: a) gyroid polystyrene template, b) as-deposited ZnO-PS hybrid, and c) ZnO gyroid after annealing at 550 °C. d,e,f) Different faces of the ZnO gyroid shown in (c). The scale bars correspond to 1 μm for (a) and (b), 400 nm for (c) and (d), 200 nm for (e) and (f). Ref: (*28*)

In a sol-gel process, precursors first form a chemical solution called “sol”. After hydrolysis and condensation, this sol starts to become interconnected network called “gel”. In Fig. 1.9, a mesoporous silica thin film with gyroid morphology is made by the templated sol-gel reaction.(*29, 30*) After degradation of the PS matrix by UV irradiation, a highly porous inorganic

gyroid network remains, yielding a single-component material with an exceptionally low refractive index

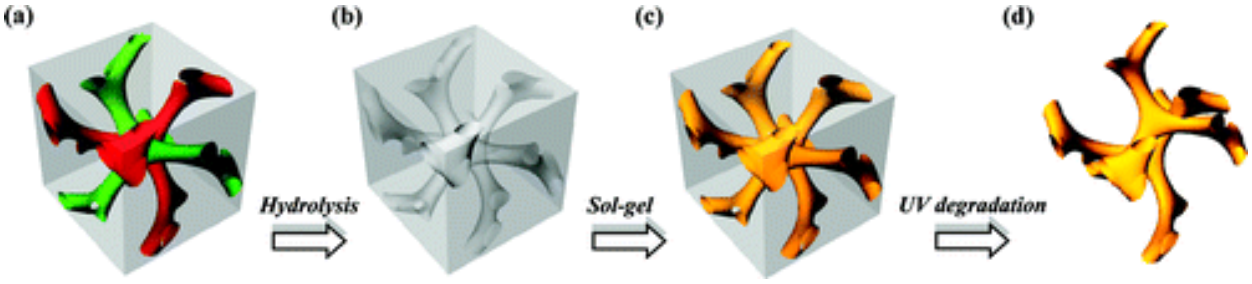

Figure 1.9. Schematic illustration for the creation of well-defined nanoporous gyroid SiO_2 from BCP templating. (a) PS-PLLA gyroid morphology (skeleton of double gyroid structure with two identical networks (green and red)). (b) Gyroid-forming nanoporous PS template after the removal of minority PLLA network. (c) PS/SiO_2 gyroid nanohybrids via the templated sol−gel process. (d) Nanoporous gyroid SiO_2 after the UV removal of PS template. Ref: (*29*)

Similar to sol-gel reaction, melt infiltration originates from the field of ceramic nanomaterials and is based on the infiltration of porous matrices with the melt of an active phase or precursor.(*31*) An advantage of this technique compared to the sol-gel reaction is a better infiltration efficiency since the hydrolysis and condensation reaction produce considerable by-products. In recent years, it has become a technique for the preparation of advanced materials like, nanocomposites, pore-confined nanoparticles, ordered mesoporous and nanostructured materials. Fig. 1.10 illustrates this simple and straightforward technique.

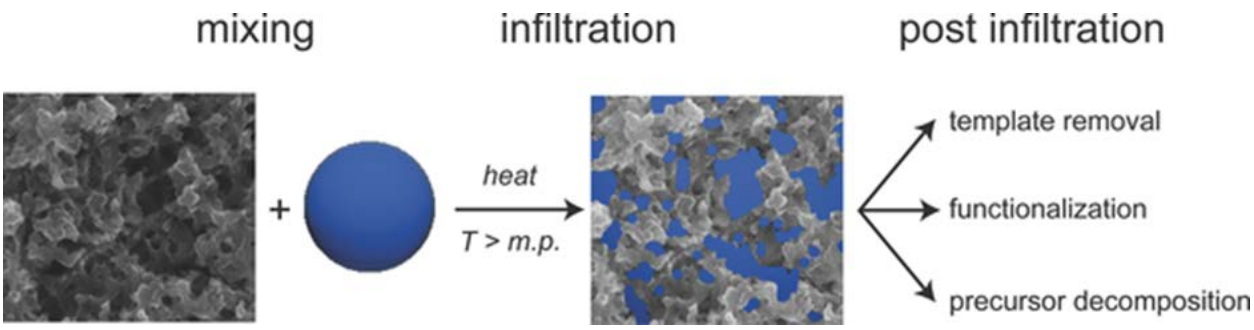

Figure. 1.10. Scheme illustrating general steps involved in melt infiltration.

To sum up, nanoporous functional materials with a well-defined morphology can improve some properties essential for nanotechnology applications. An alternative approach to the main-stream "top-down" expensive lithography technique is the "bottom-up" method utilizing self-assembly of materials on nano-scale. Block copolymers can self-organize into various morphologies with well-defined length scale. After selective removal of one block, the remaining porous polymer template offers a cost-effective and versatile route to fabricate nanoporous functional materials. The gyroid morphology is particularly suitable for 3D interconnected porous materials. Many techniques have been developed using gyroid polymer template, showing unprecedented potential for next-generation nano-device manufacture.

1.4 Block copolymers nanolithography

One of the most explored applications of BCP self-assembly is in the field of nanolithography process where BCPs can be used as masks. BCP microdomains can serve as ideal templates or scaffolds for patterning nano-scale functional materials and synthesizing nanostructured materials with size scales that exceed the limits of conventional photolithography. The cost-

effective, high throughput and scalable BCP lithography has great potential to extend Moore's law for the semiconductor and data storage industries. Conventional photolithography based on 193nm UV lithography is used to fabricate large area semiconductor chips with features down to 22 nm. Electron beam lithography offers down to sub 10 nm resolution. However, it is limited by low throughput and high fabrication costs. For this reason, BCP nano-lithography has been under extensive research both in academia and industry. After years of research and developments, now BCP lithography has been recognized by the International Technology Roadmap for Semiconductor (ITRS) as a potential candidate lithography technique to go below the 14nm node.

When a thin film of BCP is cast from solution, normally by spin-casting which can ensure high uniformity over large area, the polymer chains are often trapped after fast solvent evaporation, giving random, disordered morphology which is far from the equilibrium states. In order to increase the polymer chain mobility, an annealing process needs to be performed after casting. Thermal and solvent vapor annealing are the most frequently used annealing methods to remove the defects from as-cast films.

In a typical thermal annealing process, the BCP think film is heated above its glass transition temperature and thus the polymer chains become mobile and find their equilibrium morphology. This technique is a widely used and simple, however it also suffers from several disadvantages. It can take very long annealing time. For an example, for a typical PS-PMMA system, it requires 72 hours at 180 degree C. (*32*) And it certainly cannot applied to polymer blocks which are sensitive to heat, such as PLA. The polymeric domains can also be damaged during the heating, for an example, by oxidation.

On the other hand, solvent vapor annealing is becoming a very useful technique to anneal BCP thin films. In a typical solvent annealing process, the BCP thin films are exposed to the vapor of one or more solvents, normally at temperatures below the glass transition temperature to form a swollen and mobile polymer film on the substrate. (*33*) Extensive research works have been carried out since its first demonstration in 2004. (*34*) Despite its widespread use and proven capability to make well-defined morphologies with long range order, a comprehensive understanding of the solvent annealing process has not been established yet. Many factors collectively play a key role in dictating the experiment results, such as the substrate preparation, the nature of BCP, solvent selection, exposure methods and de-swelling process.

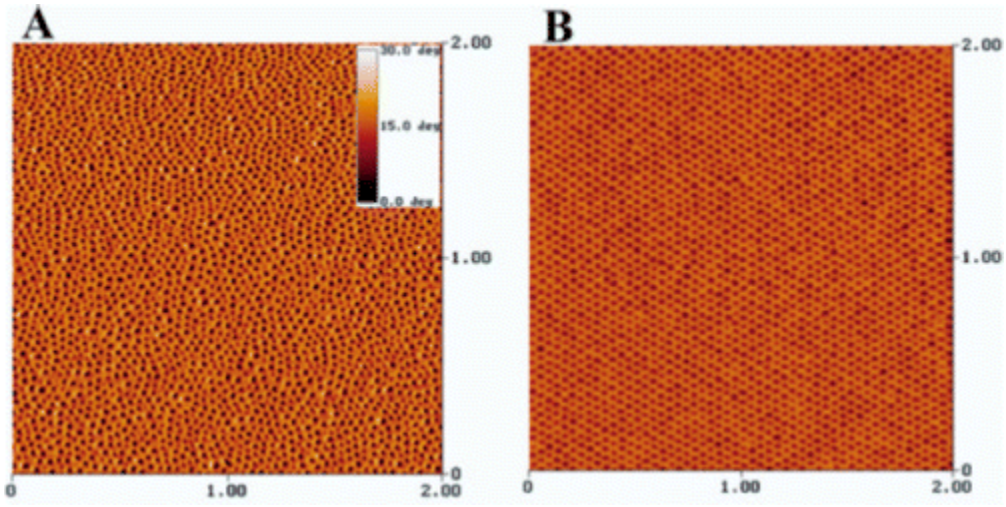

Figure 1.11 As-cast (A) and solvent vapor annealed (B) thin films of poly(styrene)-*b*-poly(ethylene oxide) block polymers. ref (*34*)

Another difficulty for understanding this process is that no standardized solvent vapor annealing has been developed. The set-up can be either very simple or complicated. In Fig. 1.11a, the substrate with surface coating of BCP is put into a closed system of solvent reservoir. After some time, the sample is taken out by simply opening the cap. Despite its extremely facile operation,

in some cases, the results are sensitive to the amount of the solvent in the reservoir, the geometry of the vessel or the solvent evaporation rate. To better control the operation parameters, some more complex systems are developed, as shown in Fig. 1.11b, where the vapor pressure, mixing ratio of the solvent, temperature and solvent evaporation rate can be finely tuned.

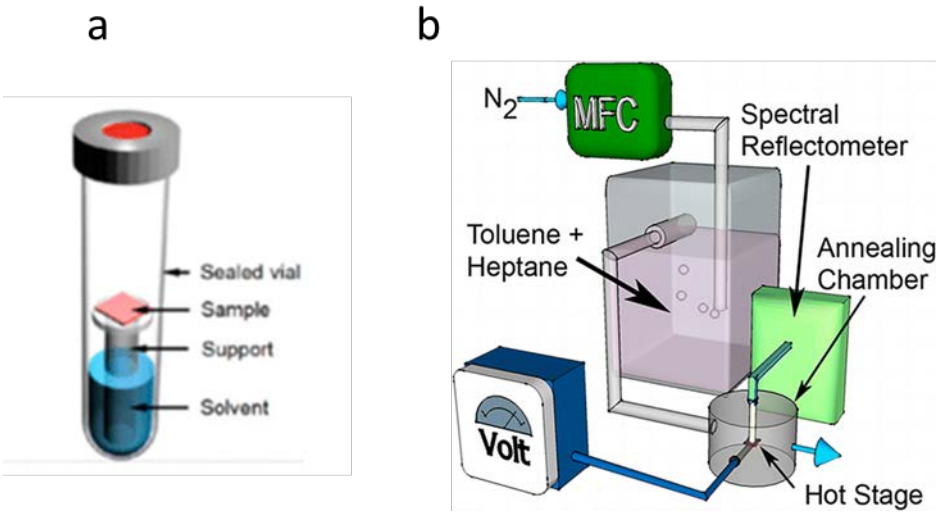

Figure 1.11. A schematic of (a) a simple solvent annealing set_up and (b) a complicated annealing system used for solvothermal annealing, which enabled a solvent vapor anneal and a thermal quenching step to remove the solvent in the film. A N_2 carrier gas passed through a solvent bubbler to provide a saturated stream of solvent vapor to an annealing chamber where a Si substrate coated with a polymer film rested on a silicon nitride resistive heater controlled by a variable voltage regulator. In situ spectral reflectometry monitored film thickness changes throughout the entire anneal. Ref: (*35*, *36*)

In 1997, the first demonstration of BCP lithography by Park et al, is shown in Figure 1.12.(*7*) Periodic arrays of holes and dots have been fabricated on a silicon nitride substrate. Spin-coated PS-PI and PS-PB thin films with well-ordered spherical or cylindrical microdomains after thermal annealing are used as the templates for pattern transfer.

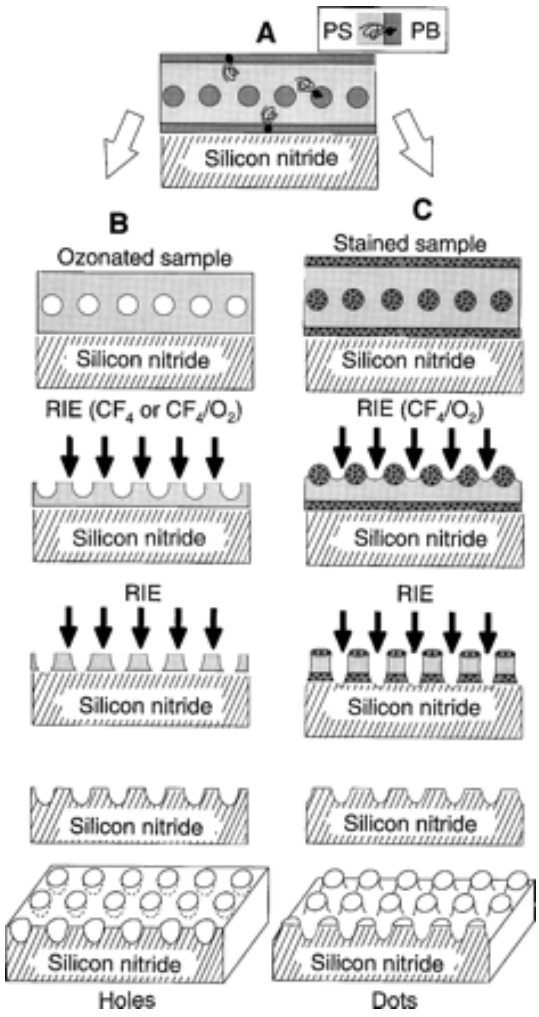

Figure 1.12. (**A**) Schematic cross-sectional view of a nanolithography template consisting of a uniform monolayer of PB spherical microdomains on silicon nitride. PB wets the air and substrate interfaces. (**B**) Schematic of the processing flow when an ozonated copolymer film is used, which produces holes in silicon nitride. (**C**) Schematic of the processing flow when an osmium-stained copolymer film is used, which produces dots in silicon nitride. Ref: (*37*)

In the example shown in Fig 1.12, the pattern transfer is through 0-D sphere morphology. For other morphologies, such as cylinder and lamella, it is important to control the orientation of microdomains; especially the perpendicular orientation is favored for a successful pattern

transfer. However, this orientation is not equilibrium-stable due to the different surface energies of the two blocks of the copolymer. As a result, preferential interaction of one block with either air or substrate causes a segregation of a thin layer at the interface of air or substrate, which in many cases causes the BCP orientating parallel to the substrate. Several techniques have been investigated to control the orientation, such as by applying shear (*38, 39*), electric field (*15, 40, 41*), magnetic field (*42, 43*), zone annealing (*44-46*), surface modification (*47-49*), and solvent vapor annealing (*50-52*).

Electric field can also be used to align the BCP orientation. The contrast in dielectric permittivity between the constituent blocks makes the domains align to the electric field. An example is given in Fig.1.13. This method is normally used for a relatively thicker film because the surface interaction can be dominant when the film is very thin. Similarly, magnetic fields are used for this purpose as well (Fig. 1.14). However, this technique is limited to the BCP systems with large dielectric or magnetic susceptibility contrasts, such as PS-PMMA, PS-PLA and PS-PEO.

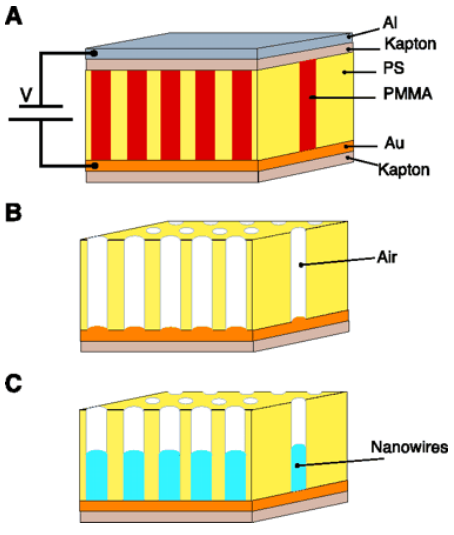

Figure 1.13. A schematic representation of high-density nanowire fabrication in a polymer matrix. (A) An asymmetric diblock copolymer annealed above the glass transition temperature of

the copolymer between two electrodes under an applied electric field, forming a hexagonal array of cylinders oriented normal to the film surface. (B) After removal of the minor component, a nanoporous film is formed. (C) By electrodeposition, nanowires can be grown in the porous template, forming an array of nanowires in a polymer matrix. Ref: (*15*)

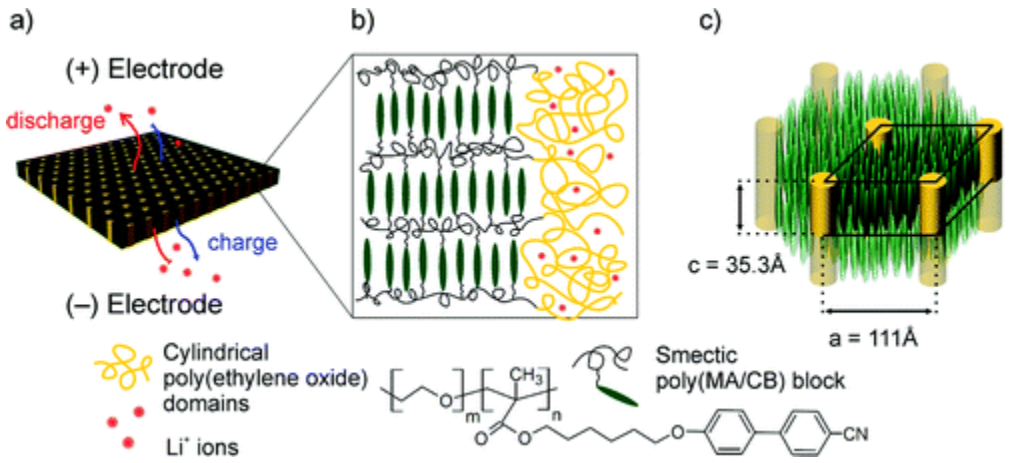

Figure 1.14. (a) Structure of the PEO-b-PMA/CB block copolymer membrane with lithium-conducting poly (ethylene oxide) cylindrical domains aligned uniformly in the current flow direction. (b) The zoomed-in views show the details of the structure of the polymer. (c) The liquid-crystalline unit cell with mesogenic backbone residues anchored in the layers transverse to the long axes of PEO cylinders. Ref: (*42*)

By far, the most widely used alignment technique is surface modification, which can be found in nearly all the BCP lithography reports. Among this technique, applying a brush layer onto the substrate is a typical example. The brush layer is a random copolymer which has functional group such as hydroxyl group, so that it can be anchored on the substrate, for an example by heating (Scheme 1). The interfacial energies of a BCP to this brush layer can be finely controlled

by the composition of the random copolymer. Perpendicular orientation can be achieved when the interface energy is equal for the two blocks. However, this extra step and the requirement of the anchoring group, indeed complicates the lithography process, as shown in Fig.1.15.

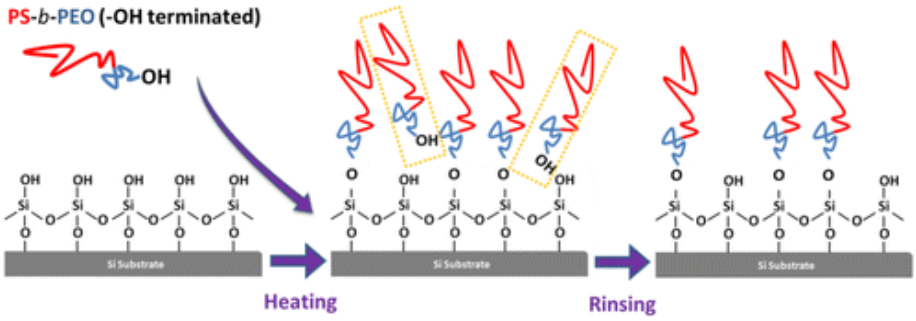

Scheme 1. Diagrammatic representation for the surface modification of Si substrates with block copolymers. Ref: (*47*)

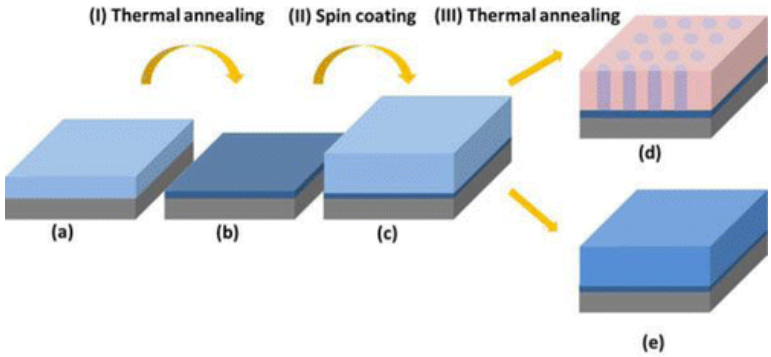

Figure 1.15. (a) Thin films composed of hydroxyl-terminated homopolymers or hydroxyl-terminated BCPs are prepared on Si substrates; (b) an anchored brush layer was left on the Si substrates after thermal annealing followed by successive solvent washing; (c) thin films of PS-b-PEO (S32EO11) are prepared on the anchored brush layer; (d) highly ordered hexagonal arrays oriented normal to the substrate are achieved after thermal annealing on the BCP brushes; (e)

microdomains oriented parallel to the substrate are achieved after thermal annealing on the homopolymer brushes. Ref: (*47*, *48*)

The lateral ordering of BCP microdomain is equally, if not more, important to some applications which require nearly perfect orientation and translation order. The most effective and widely applied way to control the lateral order is to use topographic or chemical pre-patterned features on the substrate surface. Commensurability between surface heterogeneity can guide the lattice orientation of BCP microdomain when certain boundary conditions are matched. An example of directed self-assembly of block copolymer domains on chemically patterned surfaces is demonstrated in Fig. 1.16.

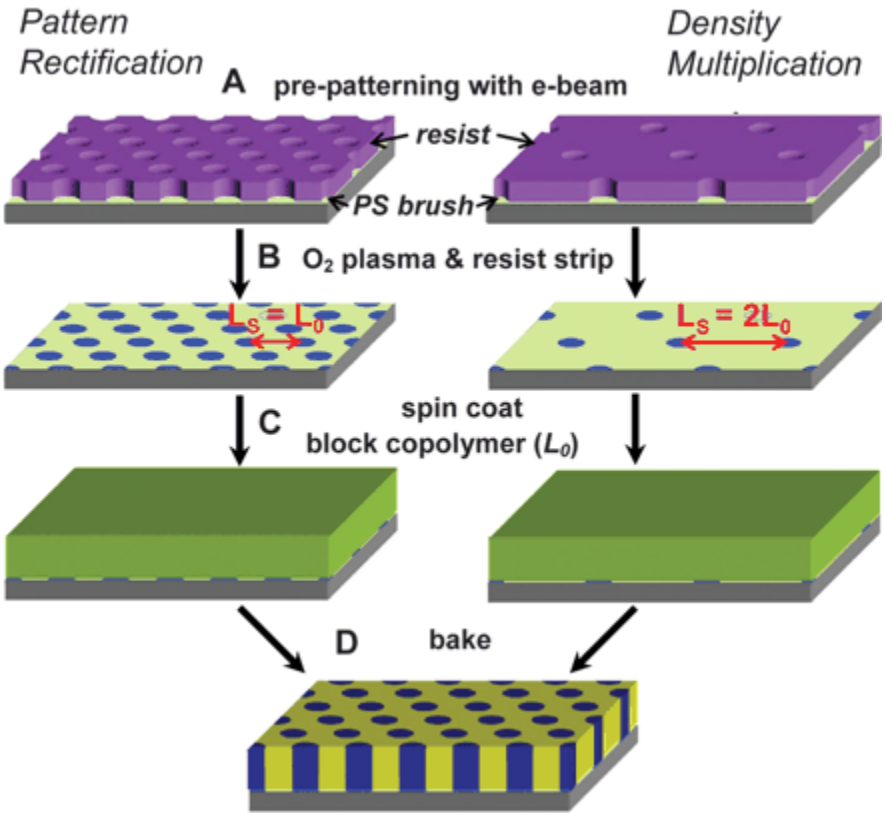

Figure 1.16. Process to create lithographically defined chemically prepatterned surfaces and subsequent directed assembly. (A) Electron-beam lithography patterns at Ls = L_0 (left) and Ls =

$2L_0$ (right). (B) Chemical contrast on the substrate after O_2 plasma exposure on the e-beam–defined spots above. (C) Block copolymer thin film. (D) Guided self-assembly in registration with the underlying chemical pattern. Ref: (*53*)

Reference

1. **F. S. Bates, G. H. Fredrickson, Block Copolymer Thermodynamics - Theory and Experiment. *Annu Rev Phys Chem* 41, 525 (1990).**
2. **F. S. Bates, Polymer-Polymer Phase-Behavior. *Science* 251, 898 (Feb 22, 1991).**
3. **F. S. Bates, G. H. Fredrickson, Block copolymers - Designer soft materials. *Phys Today* 52, 32 (Feb, 1999).**
4. **D. J. Keddie, A guide to the synthesis of block copolymers using reversible-addition fragmentation chain transfer (RAFT) polymerization. *Chem Soc Rev* 43, 496 (2014).**
5. **J. Jennings *et al.*, Advantages of Block Copolymer Synthesis by RAFT-Controlled Dispersion Polymerization in Supercritical Carbon Dioxide. *Macromolecules* 46, 6843 (Sep 10, 2013).**
6. **C. R. Martin, Nanomaterials - a Membrane-Based Synthetic Approach. *Science* 266, 1961 (Dec 23, 1994).**
7. **T. Kyotani, T. Nagai, S. Inoue, A. Tomita, Formation of new type of porous carbon by carbonization in zeolite nanochannels. *Chem Mater* 9, 609 (Feb, 1997).**
8. **C. G. Goltner, M. C. Weissenberger, Mesoporous organic polymers obtained by "twostep nanocasting". *Acta Polym* 49, 704 (Dec, 1998).**
9. **A. D. Roberts, X. Li, H. F. Zhang, Porous carbon spheres and monoliths: morphology control, pore size tuning and their applications as Li-ion battery anode materials. *Chem Soc Rev* 43, 4341 (2014).**
10. **H. Nishihara, T. Kyotani, Templated Nanocarbons for Energy Storage. *Adv Mater* 24, 4473 (Aug 28, 2012).**
11. **R. L. Liu *et al.*, Triconstituent Co-assembly to ordered mesostructured polymer-silica and carbon-silica nanocomposites and large-pore mesoporous carbons with high surface areas. *J Am Chem Soc* 128, 11652 (Sep 6, 2006).**
12. **C. J. Brinker, Y. F. Lu, A. Sellinger, H. Y. Fan, Evaporation-induced self-assembly: Nanostructures made easy. *Adv Mater* 11, 579 (May 7, 1999).**
13. **E. L. Thomas, D. M. Anderson, C. S. Henkee, D. Hoffman, Periodic Area-Minimizing Surfaces in Block Copolymers. *Nature* 334, 598 (Aug 18, 1988).**
14. **F. S. Bates, Network phases in block copolymer melts. *Mrs Bull* 30, 525 (Jul, 2005).**
15. **T. Thurn-Albrecht *et al.*, Ultrahigh-density nanowire arrays grown in self-assembled diblock copolymer templates. *Science* 290, 2126 (Dec 15, 2000).**

16. **S. Ndoni, M. E. Vigild, R. H. Berg, Nanoporous materials with spherical and gyroid cavities created by quantitative etching of polydimethylsiloxane in polystyrene-polydimethylsiloxane block copolymers. *J Am Chem Soc* 125, 13366 (Nov 5, 2003).**
17. **L. Schulte *et al.*, Nanoporous materials from stable and metastable structures of 1,2-PB-b-PDMS block copolymers. *Polymer* 52, 422 (Jan 21, 2011).**
18. **H. M. Mao, M. A. Hillmyer, Nanoporous polystyrene by chemical etching of poly(ethylene oxide) from ordered block copolymers. *Macromolecules* 38, 4038 (May 3, 2005).**
19. **J. S. Lee, A. Hirao, S. Nakahama, Polymerization of Monomers Containing Functional Silyl Groups .5. Synthesis of New Porous Membranes with Functional-Groups. *Macromolecules* 21, 274 (Jan, 1988).**
20. **H. M. Mao, M. A. Hillmyer, Macroscopic samples of polystyrene with ordered three-dimensional nanochannels. *Soft Matter* 2, 57 (Jan 7, 2006).**
21. **M. R. J. Scherer, U. Steiner, Efficient Electrochromic Devices Made from 3D Nanotubular Gyroid Networks. *Nano Lett* 13, 3005 (Jul, 2013).**
22. **H. Y. Hsueh *et al.*, Nanoporous Gyroid Nickel from Block Copolymer Templates via Electroless Plating. *Adv Mater* 23, 3041 (Jul 19, 2011).**
23. **H. Y. Hsueh *et al.*, Well-Defined Multibranched Gold with Surface Plasmon Resonance in Near-Infrared Region from Seeding Growth Approach Using Gyroid Block Copolymer Template. *Adv Mater* 25, 1780 (Mar 25, 2013).**
24. **A. Andreozzi *et al.*, The fabrication of tunable nanoporous oxide surfaces by block copolymer lithography and atomic layer deposition. *Nanotechnology* 22, (Aug 19, 2011).**
25. **S. H. Jin, G. H. Jun, S. H. Hong, S. Jeon, Conformal coating of titanium suboxide on carbon nanotube networks by atomic layer deposition for inverted organic photovoltaic cells. *Carbon* 50, 4483 (Oct, 2012).**
26. **S. J. Ku *et al.*, Highly ordered freestanding titanium oxide nanotube arrays using Si-containing block copolymer lithography and atomic layer deposition. *Nanotechnology* 24, (Mar 1, 2013).**
27. **F. B. Li *et al.*, Highly Porous Metal Oxide Networks of Interconnected Nanotubes by Atomic Layer Deposition. *Nano Lett* 12, 5033 (Sep, 2012).**
28. **E. Kim *et al.*, Gyroid-Structured 3D ZnO Networks Made by Atomic Layer Deposition. *Adv Funct Mater* 24, 863 (Feb, 2014).**
29. **H. Y. Hsueh *et al.*, Inorganic Gyroid with Exceptionally Low Refractive Index from Block Copolymer Templating. *Nano Lett* 10, 4994 (Dec, 2010).**
30. **H. Y. Hsueh, R. M. Ho, Bicontinuous Ceramics with High Surface Area from Block Copolymer Templates. *Langmuir* 28, 8518 (Jun 5, 2012).**
31. **P. E. de Jongh, T. M. Eggenhuisen, Melt Infiltration: an Emerging Technique for the Preparation of Novel Functional Nanostructured Materials. *Adv Mater* 25, 6672 (Dec, 2013).**
32. **Y. C. Tseng *et al.*, Enhanced polymeric lithography resists via sequential infiltration synthesis. *J Mater Chem* 21, 11722 (2011).**
33. **C. Sinturel, M. Vayer, M. Morris, M. A. Hillmyer, Solvent Vapor Annealing of Block Polymer Thin Films. *Macromolecules* 46, 5399 (Jul 23, 2013).**

34. **S. H. Kim, M. J. Misner, T. Xu, M. Kimura, T. P. Russell, Highly oriented and ordered arrays from block copolymers via solvent evaporation. *Adv Mater* 16, 226 (Feb 3, 2004).**

35. **K. W. Gotrik, C. A. Ross, Solvothermal Annealing of Block Copolymer Thin Films. *Nano Lett* 13, 5117 (Nov, 2013).**

36. **X. J. Zhang, K. D. Harris, N. L. Y. Wu, J. N. Murphy, J. M. Buriak, Fast Assembly of Ordered Block Copolymer Nanostructures through Microwave Annealing. *Acs Nano* 4, 7021 (Nov, 2010).**

37. **M. Park, C. Harrison, P. M. Chaikin, R. A. Register, D. H. Adamson, Block copolymer lithography: Periodic arrays of similar to 10(11) holes in 1 square centimeter. *Science* 276, 1401 (May 30, 1997).**

38. **T. A. Shefelbine *et al.*, Core-shell gyroid morphology in a poly(isoprene-block-styrene-block-dimethylsiloxane) triblock copolymer. *J Am Chem Soc* 121, 8457 (Sep 22, 1999).**

39. **Z. R. Chen, J. A. Kornfield, S. D. Smith, J. T. Grothaus, M. M. Satkowski, Pathways to macroscale order in nanostructured block copolymers. *Science* 277, 1248 (Aug 29, 1997).**

40. **M. Ruppel *et al.*, Electric Field Induced Selective Disordering in Lamellar Block Copolymers. *Acs Nano* 7, 3854 (May, 2013).**

41. **E. Gurovich, Why Does an Electric-Field Align Structures in Copolymers. *Phys Rev Lett* 74, 482 (Jan 16, 1995).**

42. **P. W. Majewski, M. Gopinadhan, W. S. Jang, J. L. Lutkenhaus, C. O. Osuji, Anisotropic Ionic Conductivity in Block Copolymer Membranes by Magnetic Field Alignment. *J Am Chem Soc* 132, 17516 (Dec 15, 2010).**

43. **M. Gopinadhan, P. W. Majewski, Y. Choo, C. O. Osuji, Order-Disorder Transition and Alignment Dynamics of a Block Copolymer Under High Magnetic Fields by In Situ X-Ray Scattering. *Phys Rev Lett* 110, (Feb 13, 2013).**

44. **G. Singh, K. G. Yager, B. Berry, H. C. Kim, A. Karim, Dynamic Thermal Field-Induced Gradient Soft-Shear for Highly Oriented Block Copolymer Thin Films. *Acs Nano* 6, 10335 (Nov, 2012).**

45. **G. Singh, K. G. Yager, H. C. Kim, A. Karim, Dynamic thermal field induced-gradient soft-shear for highly oriented and hierarchically patterned block copolymer thin films. *Abstr Pap Am Chem S* 246, (Sep 8, 2013).**

46. **B. C. Berry, A. W. Bosse, J. F. Douglas, R. L. Jones, A. Karim, Orientational order in block copolymer films zone annealed below the order-disorder transition temperature. *Nano Lett* 7, 2789 (Sep, 2007).**

47. **W. Y. Gu, S. W. Hong, T. P. Russell, Orienting Block Copolymer Microdomains with Block Copolymer Brushes. *Acs Nano* 6, 10250 (Nov, 2012).**

48. **Y. Lin *et al.*, Self-directed self-assembly of nanoparticle/copolymer mixtures. *Nature* 434, 55 (Mar 3, 2005).**

49. **I. In, Y. H. La, S. M. Park, P. F. Nealey, P. Gopalan, Side-chain-grafted random copolymer brushes as neutral surfaces for controlling the orientation of block copolymer microdomains in thin films. *Langmuir* 22, 7855 (Aug 29, 2006).**

50. **J. Peng *et al.*, Solvent-induced microphase separation in diblock copolymer thin films with reversibly switchable morphology. *J Chem Phys* 120, 11163 (Jun 15, 2004).**

51. W. Y. Gu *et al.*, Solvent-Assisted Directed Self-Assembly of Spherical Microdomain Block Copolymers to High Areal Density Arrays. *Adv Mater* 25, 3677 (Jul 19, 2013).
52. J. N. L. Albert *et al.*, Gradient Solvent Vapor Annealing of Block Copolymer Thin Films Using a Microfluidic Mixing Device. *Nano Lett* 11, 1351 (Mar, 2011).
53. R. Ruiz *et al.*, Density multiplication and improved lithography by directed block copolymer assembly. *Science* 321, 936 (Aug 15, 2008).

Chapter 2

Inorganic materials prepared by gyroid template

2.1 Introduction

Fabrication of meso-porous metal oxide thin films with high surface area is a crucial requirement for numerous applications, such as electronics, photovoltaics and catalysis. Despite considerable progress in fabrication of three-dimensional nanostructure of metal oxides, it is still quite challenging to manufacture highly ordered structures over a large area in a controlled way. Several nanoporous inorganic materials with well-defined gyroid morphology are created by replication of polymer template. The replication techniques include melt infiltration, ALD and direct plasma etching, which are discussed in detail in the following sections.

2.2 Nanoporous gyroid TiO_2 and SnO_2 by melt infiltration of block copolymer templates

Introduction: Meso-porous titania (TiO_2) and tin dioxide (SnO_2) both n-type semiconductors, are among the most promising materials for applications such as solar cells (*1-3*), batteries (*4*, *5*), photo catalysts (*6*) and gas sensors (*7*). For these applications an optimal device needs to fulfill the maximization of interfacial area per volume and the interconnectivity between each interfacial element with the external circuit simultaneously. Currently, the manufacture of well-

defined nanostructures mainly depends on top-down nanolithography processes (*8, 9*). However, the resolution of the nanostructures, the material quality and the fabrication process of complex three-dimensional structures are normally rather limited for these techniques. And also, decreasing particle or feature size is generally accompanied with a decrease in the intrinsic thermal and chemical stability. Therefore, it is a significant challenge to demonstrate local control over material assembly on the 10-nm length scale in macroscopically extended layers of micrometer thickness.

The next generation of nanostructure processing could take advantage of bottom-up process utilizing self-assembly which can overcome the problems list above. Preparation of mesoporous TiO_2 and SnO_2 has been developed by using surfactant and block copolymers (*10-13*), but those are less successful compared with syntheses of mesoporous silica materials in terms of long range order and well-defined structures. One challenge lies in the structure collapse during the mesoporous architecture formation and organic templates removal due to the high lattice energy in most metal oxides.

While only few of the functional materials self-assemble into optimal nanostructures, template-assisted precision replication utilizing self-assembled template is considerably versatile. In particular, block copolymer has been extensively developed to self-assemble into arrays of various well-defined one-, two- and three-dimensional structures because of the incompatibility of the constituent blocks. The periodicity of block copolymer can be readily adjusted by tuning its constituted compositions and molecular weight.

Recently, the material with gyroid morphology draws lots of attention because it offers the materials with a 3D inter-connected framework. Block copolymer self-assembly provides an effective, straight forward and economic way to produce mesoporous template with gyroid morphology. After adoption of an appropriate morphology during phase separation, nanoporous matrices can be derived from partially or entirely removing one block through ozonolysis (*14*), UV degradation (*15*), base or acid (*16-18*) and reactive ion etch (*19*). As a result, metals and metal oxides can be filled into the gyroid pore by many techniques, for examples, electro-deposition (*1*, *20-22*), electroless plating (*23*, *24*), solution impregnation (*25*), seed growth (*26*), and atomic layer deposition (*27*).

On the other hand, nanocasting by melt infiltration, as a rather straight-forward method, has become one of the rapidly expanding toolbox to design and fabrication functional materials for the advances in nanoscience and technology (*28*). It based on the infiltration of porous template with an active phase or precursor to form nanocomposite which is subjected to further post treatment to remove the template and give the final product.

We have successfully developed a series of cross-linked 1, 2-polybutadiene-PDMS block copolymers which yield nanoporous 1, 2-polybutadiene template by selectively and quantitatively etching PDMS with tetrabutyl ammonium fluoride (TBAF) (*29*). It features controllable morphology, pore size and orientation, high porosity and facile surface modification (*30*), making it a versatile material in many applications like membrane ultrafiltration (*31*, *32*), and liquid-core waveguides (*30*). Traditionally templates can be categorized into two groups: “hard” templates like mesoporous silica and alumina, and “soft” template like polymer. The

cross-linked nanoporous polybutadiene provides certain merits in melt filtration process: first, it can be easily processed into free-standing thin film which can be easily separated from the precursor and this is difficult to be achieved from “hard” particle template. Although the anodized aluminum oxide films are commercially available (*33*), their cylinder pore system do not qualify multi-continuity. And second, since it is cross-linked, the structure stability and chemical inertness is much stronger than the “soft” template, which is essential to maintain the structure integrity in the melt infiltration process since generally chemical and physical (dissolving) reaction of the template with the precursor is undesired.

This work explores the use of block copolymer self-assembly for the manufacture of metal oxides thin film of micrometers thickness with well-defined periodic morphology, high surface area and structure connectivity. The nanocasting procedure by melt filtration is shown in the Scheme 1: Firstly the block copolymer self-assembly into gyroid morphology at 140 degree C and at the same time it is cross-linked by dicumyl peroxide to fix PB domain. Then PDMS domain in the polymer template is removed by TBAF chemical etching. After drying, the template is immersed into the liquid inorganic precursor with ultrasound mixing at the desired temperature: For TTIP (m.p. 290k) it is conducted under room temperature and for TCN (m.p. 310-311k) it is performed at 333k. After proper post infiltration treatment, the nanocomposite materials are calcined in a furnace with air atmosphere to 450^{o}C or 500^{o}C, which can burn away the polymer template and simultaneously crystalize the metal oxides with the desired crystal phase.

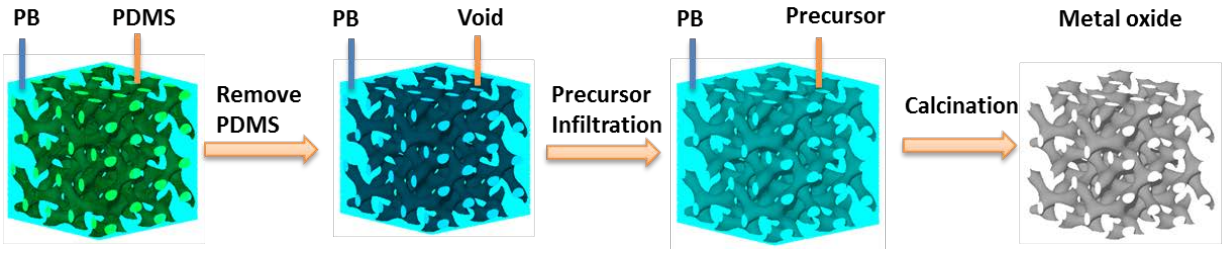

Scheme 1. Schematic illustration of creation of ordered gyroid TiO_2 and SnO_2 from cross-linked nanoporous PB.

Comparing with alternative preparation method like solution impregnation, melt filtration in this work also offers several advantages. One of the limitations in solution impregnation is that if the metal oxides precursor has low solubility, multiple infiltration steps have to be carried out in order to have a high degree of pore-filling. Another challenge is that many meal oxides precursors are not stable in normal conditions. For examples, TTIP is often used as TiO_2 precursor, however, it is sensitive to moisture and thus it can only be preserved in strong acid condition which limits its application. The TCN applied in this work is also commonly used as the precursor of SnO_2, which suffer from fast hydrolysis and precipitation in water. Recently Hsueh, et al reported making gyroid TiO_2 by solution impregnation (*25*). In this case, melt infiltration in cross-linked nanoporous PB has practical advantage of high degrees of pore filling in a single infiltration step, exclusion of solvents, stabilizer, careful experiment control and complex procedure. Ordered mesoporous SnO_2 was also reported by melt infiltration using various mesoporous silica templates (*3*, *34*, *35*), but as mentioned before, it is difficult to acquire the production of large size bulk and large area films from silica and other inorganic materials. Therefore, this new method provides an unprecedented facile way to fabricate high-surface-area, high-porosity TiO_2 and SnO_2 with self-supporting structure and controlled crystalline phase for

practical applications, which can also be extended to make other mesoporous ceramics like ZnO, et al.

Experiment:

Polymer template preparation: The 1, 2-PB-b-PDMS copolymer was synthesized by living anionic polymerization as described in ref 29. The 1, 2-PB-b-PDMS block copolymer was dissolved in tetrahydrofuran (THF, Sigma-Aldrich) containing 0.01 mols of dicumyl peroxide cross-linker (DCP, Sigma-Aldrich) per mole of 1, 2-PB repeating units. Nanoporous membrane made from 1, 2-polybutadiene-b-PDMS was fabricated by a "sandwich" method. Porosity was obtained by etching the phase of PDMS (*32*) and the thickness was controlled by adding a spacer between the two microscope glass slides.

Synthesis of gyroid TiO_2 thin film: The mesoporous TiO_2 material was synthesized by the nanocasting method using the above cross-linked nanoporous PB as the templates. Typically, the dried PB template was dropped into a glass bottle containing 5ml of TTIP ($Ti[OCH(CH_3)_2]_4$, Aldrich, 97%, m.p. 287–290 K) at room temperature. The bottle containing the mixture was sealed and under ultrasonication for 1 hour to mix the precursor and PB template. Subsequently, the film was taken out and immersed into isopropanol for several seconds with shaking to remove excess precursor hanging on the out surface. The composite materials, then, was transferred to a chamber at 353 K under saturated water vapor for 2 hours to fully hydrolyze the precursor. The resulting material was subjected to the same precursor filling and hydrolysis loop, and this step was performed three times to have a high degree of pore-filling. Finally, in order to

remove the PB template and crystalize the titania precursor, the composite was heated in an oven at 723 K under static air conditions for 2 hours with a ramping rate of 1k/min for both heating and cooling.

PB surface modification: After cross-linking of PB domain, 30–50% of the original double bonds in 1, 2-PB typically survives the cross-linking reaction (*36*) and are preferred loci for coupling of thiols by thiol-ene chemistry (*30*), where sodium 2-mercaptoethanesulfonate (MESNA, Sigma-Aldrich) are grafted onto the pendant vinyl groups of nanoporous 1, 2-PB. Briefly, 500 mM thiol (MESNA) and 10 mM of the photo initiator (2, 2-dimethoxy-2-phenylacetophenone, DMPA) were prepared in the solvent of a 25/75 v/v mixture of water and methanol. Then the nanoporous PB was immersed in this solution for 1-2 hours. Subsequently, the whole system was subjected to photo-activation under a UV-light for 30 minutes. After exposure the template was ultrasonicated in the same solvents three times to remove non-reacted compounds and dried for 8 hours under vacuum.

Synthesis of gyroid SnO_2 thin film: The mesoporous SnO_2 material was prepared by the nanocasting method using the above surface-modified nanoporous PB as the templates. Typically, the dried PB template was dropped into a glass bottle containing 6 gram of TCN ($SnCl_2 \cdot 2H_2O$, Aldrich, 98%, m.p. 310–311 K) that was melted to liquid phase at 333K. The bottle containing the mixture was sealed and under ultrasonication at 333K for 1 hour to mix the precursor and PB template. Subsequently, the film was taken out and immersed into methanol for several seconds with shaking to remove excess precursor hanging on the out surface. The composite material was heated to 473 K under static air conditions for 5 hours to solidify the precursor. Then the

temperature was raised up to 773 K under static air conditions for another 2 hours with a ramping rate of 1k/min for both heating and cooling to remove the PB template and crystalize the tin dioxide precursor.

Characterization:

Transmission electron microscopy (TEM) was performed on a FEI TECNAI T20 at acceleration voltage of 200 kV. The film sample of the ceramics was crushed into powder in a mortar. The powder was dispersed in ethanol and then was deposited onto a holey carbon-coated copper grid for TEM measurements.

Scanning electron microscopy (SEM) was done either on a SEM-Zeiss or a Quanta 200F instrument from FEI with an energy-dispersive detector (EDX). The samples were sputter-coated with 2-nm thick Au prior to SEM imaging except of the sample of SnO2 which is conductive itself.

In the BET measurement, the sample was pre-dried under vacuum overnight before the measurement. The amount of sample used for the measurements was in the range around 100 mg. The measurements were performed on a Micromerities ASAP 2020 Surface Area and Porosity Analyzer. The isothermal physisorption (adsorbed mass against pressure) was analyzed by the method of Langmuir and Brunauer–Emmett–Teller (BET), while the calculation of the pore size and distribution followed the scheme of Barrett–Joyner–Halenda (BJH).

X-ray diffraction patterns was characterized by X-ray diffractometer PANalytical X’pert Pro using Cu Kα radiation (λ = 1.5416 Å). Thermogravimetric analysis (TGA) was performed on a

Q500 (TA Instruments) in a nitrogen atmosphere with a heating rate of 20 °C min−1, from room temperature to 600 °C.

Results and discussion:

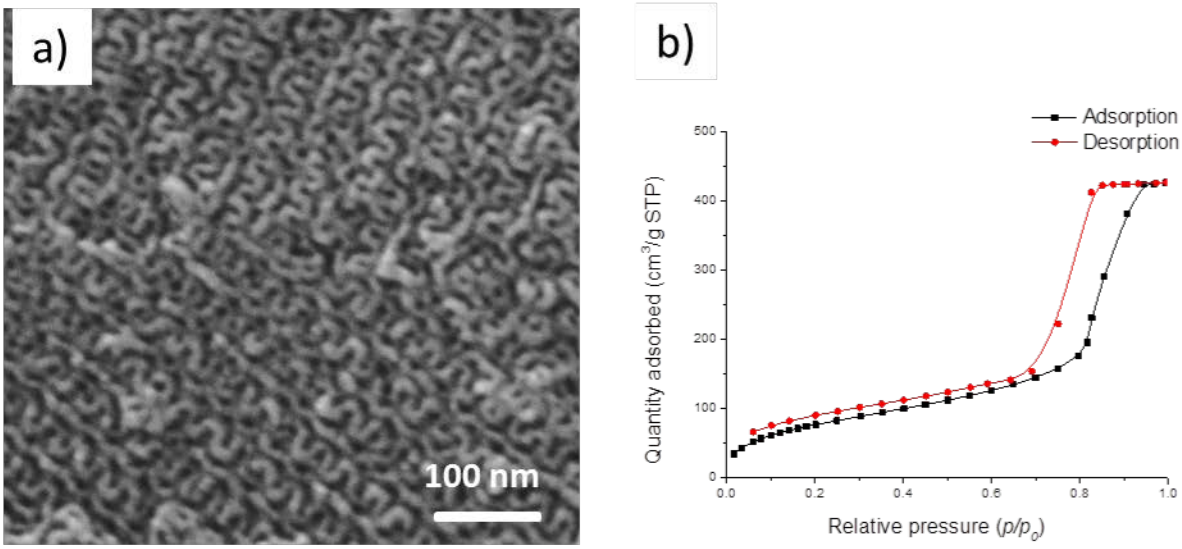

Figure 2.1. (a) SEM image of the as-synthesized cross-linked nanoporous PB template. (b) N_2 adsorption-desorption isotherms of the PB template.

Starting with a block copolymer precursor of lamellar morphology at room temperature, the gyroid structure is permanently captured by cross-linking the precursor at 140^{o}C for 1-2 hours (*29*). PDMS is the minority block with a 40% volume fraction. After the selective and quantitative removal of PDMS by TBAF, gyroid porosity is generated in the space previously occupied by the PDMS domain. The typical “wagon-wheel” gyroid morphology can be clearly observed in Fig. 2.1a, which also shows regular patterns with uniform pore size of 10 nm in

diameter and a crystallographic unit cell size of 45 nm. Fig. 2.1.b shows the results from isothermal adsorption of nitrogen into the nanoporous PB template. The adsorption isotherm is of type IV with a hysteresis loop of type H1, characteristic of mesoporous materials with a narrow pore size distribution, and the BET surface area is estimated to be around 291 m^2/g. More characterization details about the polymer template can be readily found in the literature (*29*). As a result, the transparent and mechanically stable PB thin film with a 1 cm^2 area and 20-um thickness is used as the template for melt infiltration.

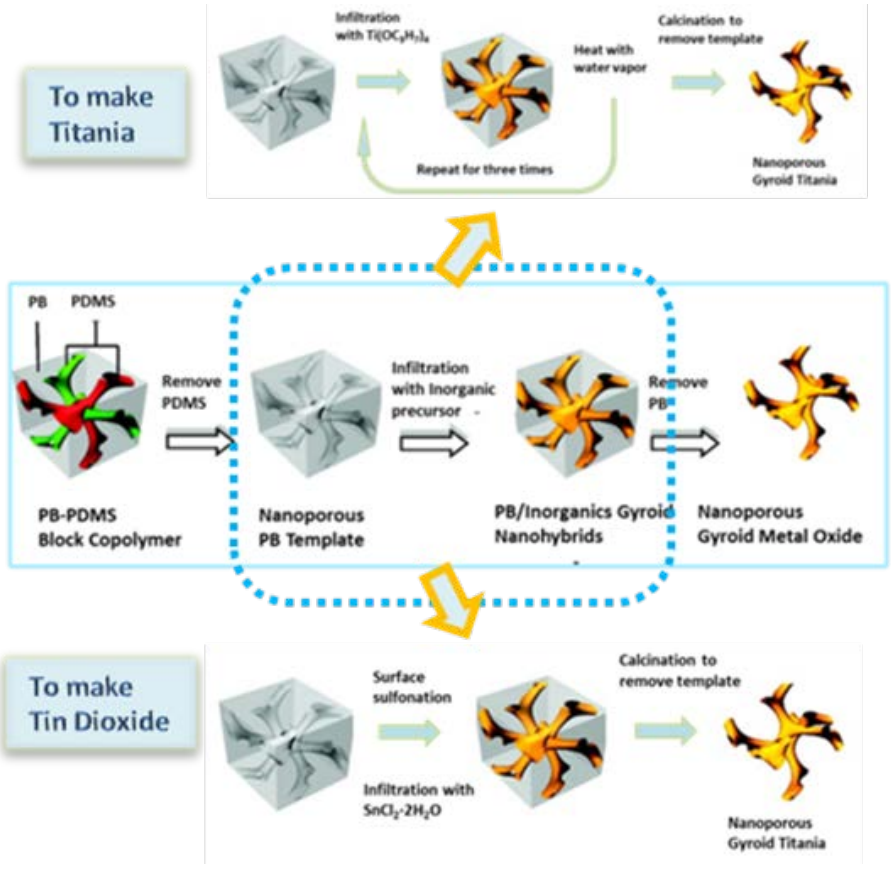

Scheme 2. Schematic illustration for the creation of ordered gyroid TiO_2 and SnO_2 from the cross-linked nanoporous PB.

The principle of the nanocasting by melt infiltration in this work is straight-forward. The solid phase (template) is contacted with the liquid phase (at the temperature above the melting point of the precursor). Then the liquid is drawn into the pores of template by capillary forces. And finally the composite is subjected to further treatment to obtain the desired product. In this process, several important experiment factors need to be considered: the wetting property between the two phases, the ratio between the filler and template, and post treatment. One of the advantages to use bulk film instead of particle powders is the facile separation between the template and liquid precursor. Thus the consideration of the ratio between the precursor and template is unnecessary since always excess of precursor will be applied to guarantee complete pore filling, and usually the template is much more expensive than the precursor. The detailed procedure is schematically illustrated in Scheme 2.

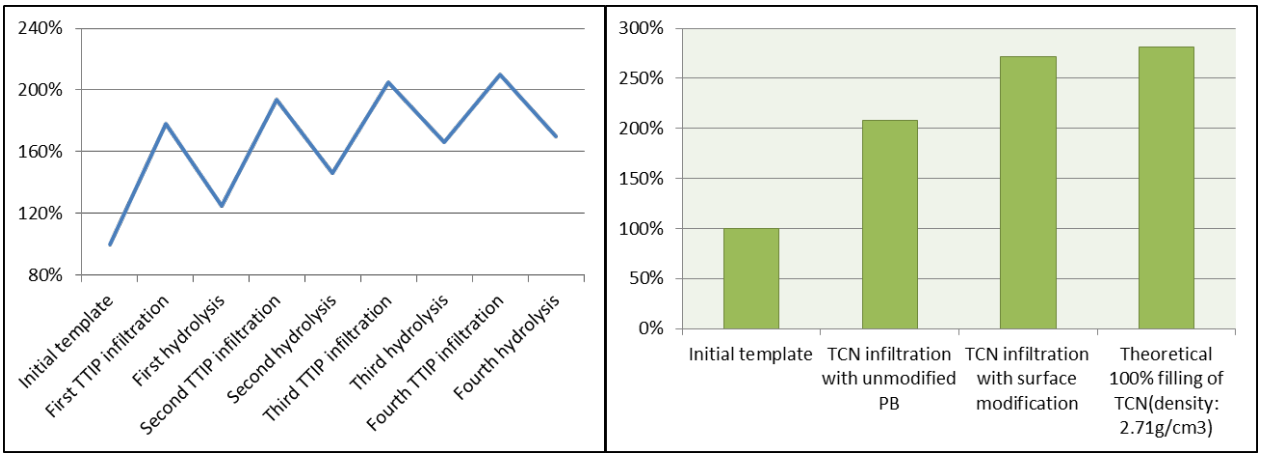

Figure 2.2. Weight analysis of the pore filling efficiency of (a) for TTIP loading, and (b) for TCN loading.

To make gyroid titania, TTIP was used as the precursor which is liquid at room temperature, so no heating is required in the pore filling process. Due to the large organic moiety presents in this

compound, it has excellent wetting property with the hydrophobic inner wall of the PB template，which is evidenced by the weight analysis of the pore filling efficiency in Fig.2.2 (a). In the first infiltration step, the template gains weight of 78% which is very close to the theoretical calculation of 64% weight gain, assuming 40% of the void is occupied. The slightly higher weight gain is probably due to the skin layer which will be discussed in section 2.4. The chemical reaction in the following hydrolysis process is described by the eq.1:

$$Ti\{OCH(CH_3)_2\}_4 + (4\text{-}x)H_2O\ (g) \rightarrow TiO_xH_{(4-2x)} + 4(CH_3)_2CHOH\uparrow \quad (1)$$

The weight loss of the sample is still in a good agreement with theoretical estimation which indicates complete hydrolysis at the experiment condition. Eq.1 shows the large by-product (isopropanol) loss (73%) after the hydrolysis. Therefore it is necessary to repeat the filtration to achieve a higher precursor loading. The remaining is a network of amorphous TiO_xH_y which is partially condensed and thus it remains in the pore during the following infiltration. Finally it will be fully converted into titania in the calcination process. Based on Fig.2.2a, after the third infiltration the weight gain is not noticeable, therefore this loop is repeated three times to have a high degree pore-filling before calcination.

As for the tin dioxide, since the PB template surface is hydrophobic and TCN is a salt which is a very polar compound, poor wetting property between the two distinct materials is expected. To a surprise, initial weight analysis shows some degree of pore filling, as shown is Fig. 2.2b. There are evidences that in nanoscale system, spontaneous infiltration with non-wetting liquids can

occur sometimes (*28*). Nevertheless, the pore-filling is not complete which can be observed in Fig 2.3 that the sample is not continuous and some region show single gyroid morphology. What's more, after calcination the film breaks into small pieces. In order to address this issue, hydrophilization of nanoporous 1,2-PB by thiol-ene photochemistry (*30*) is applied to change the surface tension for a better wetting with the TCN precursor. As shown is Fig. 2.2b, after the surface modification, the pore filling (271%) is almost the same with the theoretical value (282%). Since after the precursor decomposition, the remaining final product (SnO_2) is in a large portion of the precursor (67%), only single infiltration is needed to make gyroid tin dioxide.

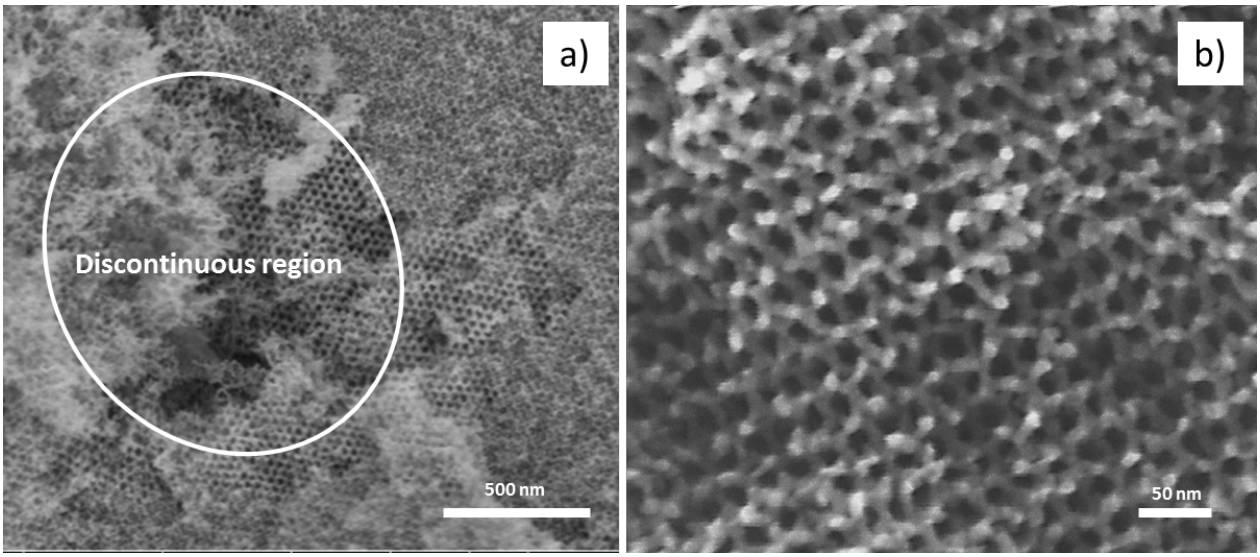

Figure 2.3. After calcination, SEM image of (a) discontinuous SnO_2 framework due to the poor wetting property between the precursor and template (b) single gyroid morphology of SnO_2 framework prepared without template surface modification.

The calcination process also plays an important role in removing the polymer template and crystalize the metal oxides precursor. The high annealing temperature will improve the crystallinity of the metal oxides but it will often leads to the mesopore structure collapse due to

the thermal expansion and cooling shrinkage. Especially during the polymer template removal, the gasification of the carbon source and disappearance of the template support, considerable stress will be generated along the networks. And thus, calcination is conducted by reasonably slow heating and cooling ramping rate.

The specific calcination condition to make gyroid titania is described as follows: the sample is slowly heated to 450^{o}C at 1^{o}C/min; held at 450^{o}C for 2 hours, and then slowly cooled to room temperature at 1^{o}C/min.

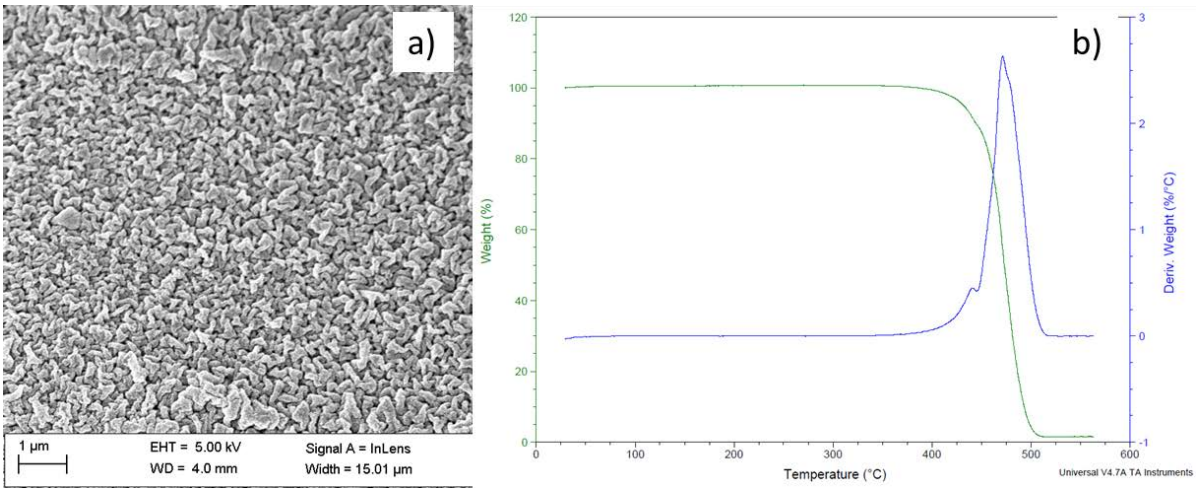

Figure. 2.4. (a) SnO2 morphology prepared with a heating rate of 1^{o}C/min. (b) TGA analysis of the cross-linked nanoporous PB template.

However, initial experiment to make gyroid tin dioxide using the same calcination protocol leads to a dense material as shown in Fig. 2.4a. The reason may be due to the complex process of TCN precursor degradation. In the case of titania, before calcination, it is already amorphous TiO_2 after TTIP hydrolysis. To decompose TCN, multiple chemical reactions may take place

including oxidation of tin(II) to tin(IV) (*37*). We suspect that during template removal process, some intermediate compounds which are not converted to tin dioxide yet are liquid, and therefore the mesopore structure is fused into a dense material. In order to solidify the precursor completely before the template removal, an additional of annealing stage (200^{o}C for 5 hours) is added into the whole calcination process. As shown is Fig. 2.4b, at this temperature the PB template should be intact.

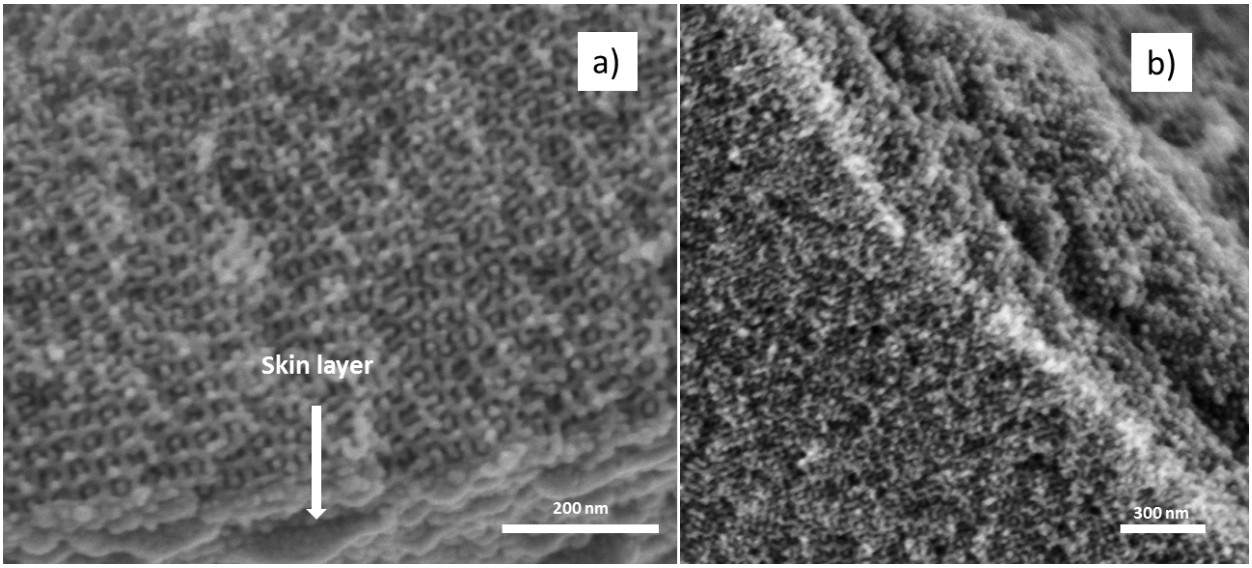

Figure 2.5. SEM image of the as-synthesized Tin Dioxide without rinsing step (a) and with an extra rinsing step (b)

When the film is lifted out from the precursor solution, the precursor which is sensitive to moisture in air inevitably and immediately forms a skin layer on the template surface which is difficult to be removed by wiping with a tissue paper. And as it can be clearly observed in the Fig. 2.5a: the surface morphology is more dense and irregular compared with the bulk. For practice purpose, it is highly desirable that the film features an open surface. In many replication

processes, precursor can form a skin layer at the surface or the crystal grows outside the mesoporous template to block the pore. To overcome that, a rinsing step was added, in which the composite film was immediately immersed and rinsed in a solvent which can dissolve the precursor properly. Isopropanol and methanol was used to dissolve the precursor for TiO_2 and SnO_2 respectively. As it is shown in Fig. 2.5b, the gyroid morphology is continuous and fully open through the whole film. Actually this is another advantage to use bulk film template than particles since it's much easier to rinse the film template manually than particles to avoid any dense layers deposited on the out surface.

Fig. 2.6 a,b show the crack-free centimeter-sized titania thin film with a thickness around several micrometers. The successful replication of the double gyroid channel of the PB template after calcination can be visibly observed in Fig. 2.6c. The framework structures of mesoporous TiO_2 materials are highly crystalline with anatase phase which has the highest photo-catalytic activity, as shown in the wide-angle XRD patterns in Fig. 2.6d. The XRD pattern is somewhat broad peaks, which in a good agreement that the metal oxides particle size is very small. The EDX results are summarized in Table 1, which confirm the sample composition roughly equivalent to the metal oxides without the presence of carbon signal, which strongly indicate that the nano-composite successfully transform into the desired metal oxides with full removal of the polymer template.

Table 1. EDX spectroscopy data for the mesoporous TiO_2 and SnO_2 materials obtained from SEM-EDX spectra.

Materials	Oxygen (atomic %)	Metal (atomic %)	Oxygen/Metal
TiO_2	69.4	30.6	2.3

SnO_2	70.5	29.6	2.4

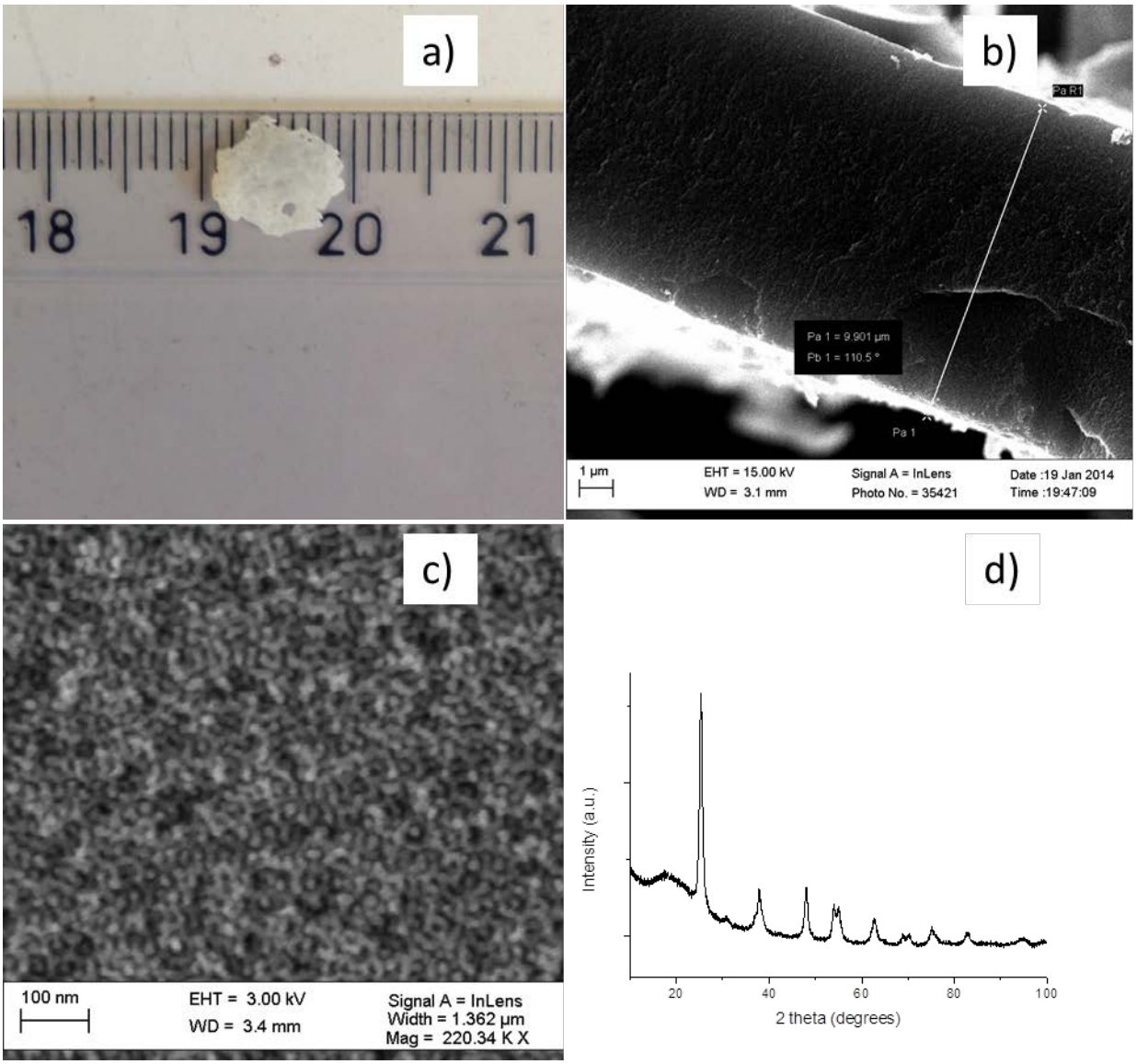

Figure. 2.6. (a) thin film of as-prepared TiO_2 with an area of sub-centimeter square (b) and thickness of several micrometers, (c) SEM image of the double gyroid TiO_2 framework. (d) XRD pattern of the as-synthesized TiO_2 film.

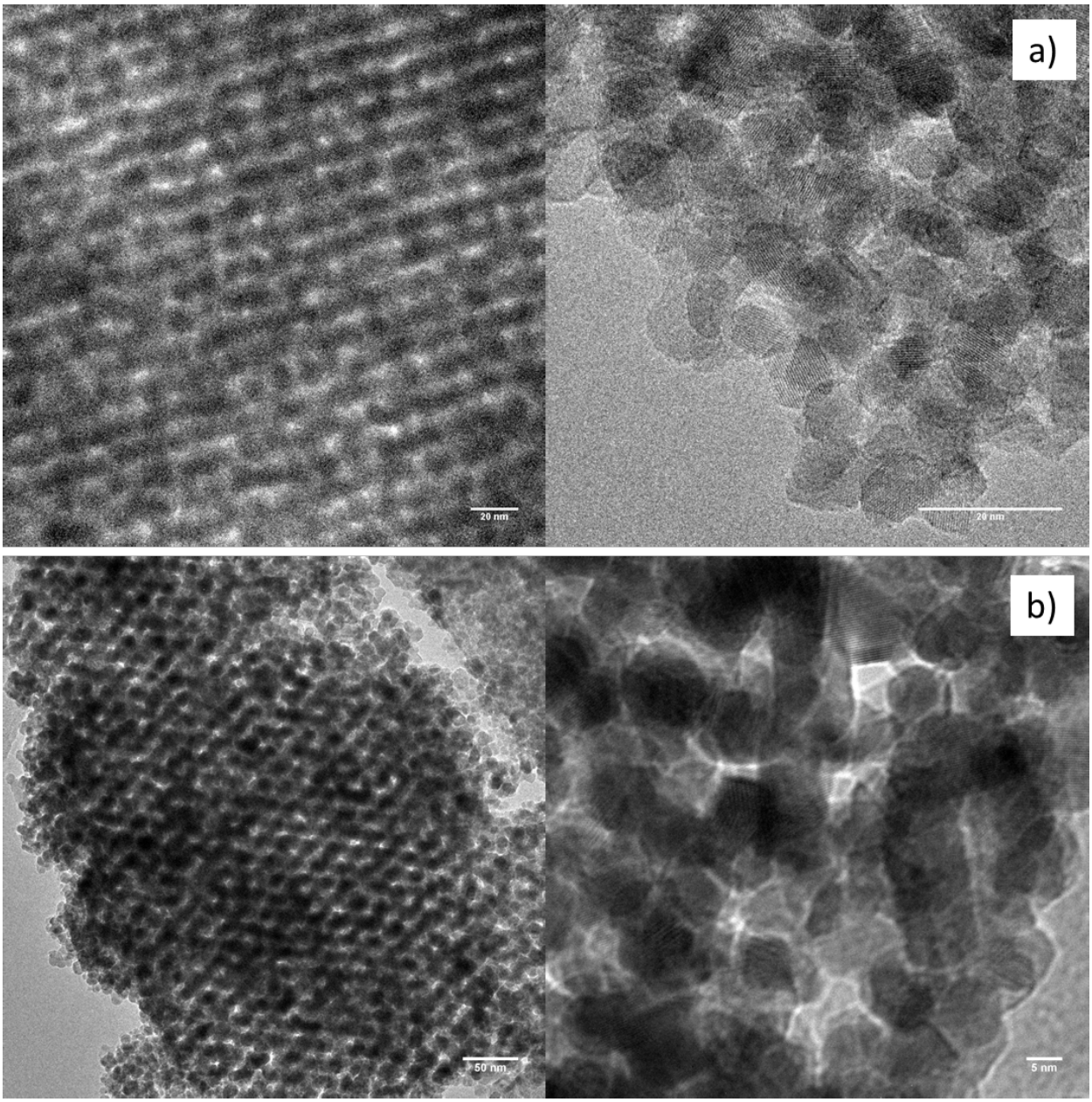

Figure 2.7. TEM image of (a) as-synthesized Titania, (b) as-synthesized Tin Dioxide with the gyroid morphology.

TEM images in Fig. 2.7 clearly show that all the mesoporous TiO_2 and SnO_2 materials display well-defined meso-pore structures and highly crystalline networks, strongly support that the replication from the PB templates is successful. The domain sizes of the TiO_2 and SnO_2

frameworks are about 8 nm. The nanostructures of TiO_2 and SnO_2 are highly ordered and very similar to the PB templates. The higher magnification TEM image also indicates that the networks contain interconnected nano-particles.

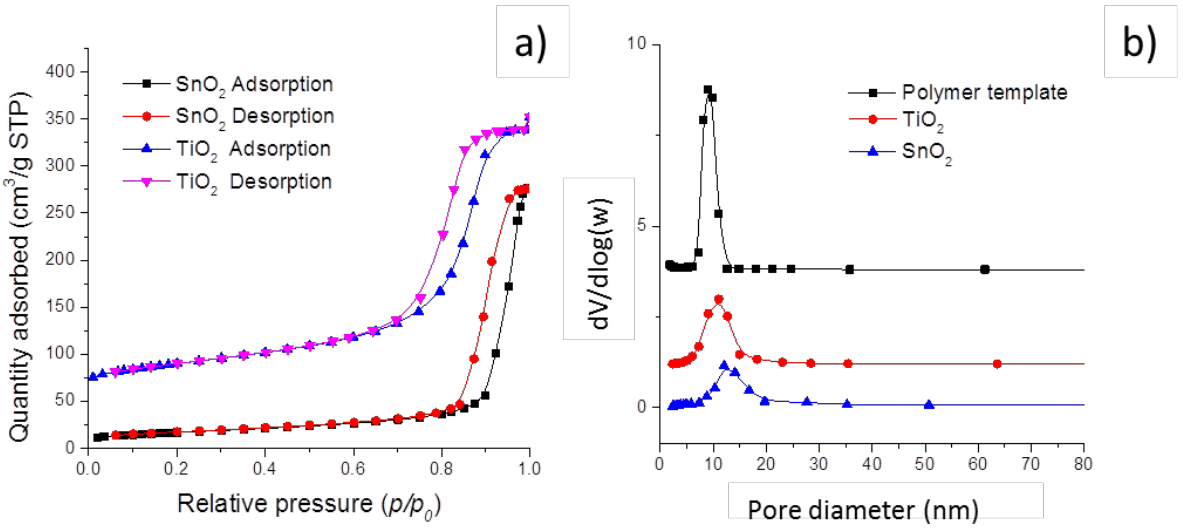

Figure 2.8. (a) N_2 adsorption-desorption isotherms of the as-synthesized metal oxides. (b) Pore size distribution of the nanoporous template and metal oxides, calculated from the adsorption branch by the BJH method.

The porosity of the as-synthesized metal oxides was characterized by N_2 adsorption-desorption isotherm. Fig. 2.8a shows typical type IV isotherms with hysteresis loops, suggesting that the nanoporous metal oxides exhibit well-defined mesoporous structure. The surface area of TiO_2 and SnO_2 is estimated to be 143 m^2/g and 60 m^2/g respectively. Unlike many similar mesoporous metal oxides reported in literature (*25*), only uni-modal pore size distribution is observed for all the templates and metal oxides, as evidenced by the Barrett-Joyner-Halenda (BJH) analysis shown in Fig. 2.8b. The absence of micropores and larger pores, which is often observed in the porous materials made by nanocasting, indicates excellent pore-filling. Compared to the polymer

template, the broader pore size distribution and larger pore size of the metal oxides, are probably due to the pore wall shrinkage after the thermal calcination.

In conclusion, self-assembly of block copolymer into double gyroid morphology is optimized for use as a 10-nm scaffold for fabrication of meso-porous metal oxides thin film. Ordered mesoporous metal oxides thin film, such as titania and tin dioxide, are created using this simple nanocasting method by melt infiltration. Different strategies are carried out for complete pore-filling and conversion of the two inorganic precursors, including surface modification and specific calcination protocols. The double gyroid morphology of the PB templates is well maintained in the mesoporous TiO_2 and SnO_2 materials after the present nano-replication process. The present new method provides an unprecedented facile way to fabricate high-surface-area, high-porosity TiO_2 and SnO_2 with self-supporting structure and controlled crystalline phase for practical applications, which can also be extended to make other mesoporous ceramics like ZnO, et al.

2.3 Fixation of the BCP template onto the substrate

For many applications, the nanoporous semiconductors nees to be fixed on a substrate suitable for the specific purpose. For the example of dye-sensitized-solar-cell, a transparant and conductive substrate is needed as displayed in Fig 2.9. During the PDMS wet etching step, however, the nanoporous porous film is detached from the substrate. In this section, a surface modification method is introduced to chemically bond the template with the substrate.

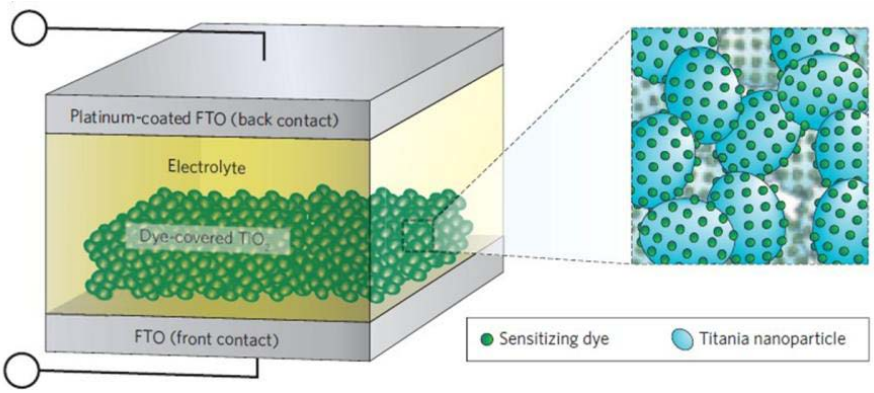

Figure 2.9. Liquid-based DSCs are comprised of a conducting oxide on glass, a nanoparticle photo-anode covered in a monolayer of sensitizing dye, a hole conducting electrolyte and a platinum-coated, FTO-coated glass back-contact.

Materials: All the solvents are purchased from Sigma Aldrich without further purification. Fluorine doped tin oxide (FTO) coated glass slide (L × W × D = 50 mm × 50 mm × 2.2 mm) with a surface resistivity ~7 Ω/sq is purchased from Sigma Aldrich. Indium tin oxide (ITO) coated glass slide with a square surface resistivity 8-12 Ω/sq is purchased from Sigma Aldirch. The Prex substrate is provided by Ole Hansen's group.

Fabrication: The FTO and ITO substrates are activated by oxygen plasma. 60uL trichlorovinylsilane is added in fresh cyclohexane. The treated substrates are immersed in this solution for 2 minutes and rinse with ethanol several times. The PB-PDMS in cyclohexane with 3-4% DCP (relative to BCP) are spin-coated on the substrate to give around 1.5 um thin films. Then the sample is put into the wet etching solution (TBAF in THF) for 1 day, and rinsed in THF repeatly for several hours. The irregular top layer is removed by short oxygen plasma. Then the sample is infiltrated with TiO_2 precursors as described in last section.

Characterization:

SEM was done either on a SEM-Zeiss or a Quanta 200F instrument from FEI with an energy-dispersive detector (EDX). The samples were sputter-coated with 2-nm thick Au prior to SEM imaging except of the sample of SnO2 which is conductive itself. XPS measurement is performed on a XPS-ThermoScientific instrument.

Results and discussion: Silanation is a well-known surface modification technique for the substrates with hydroxyl group (*38*). The fixation can be best described in Scheme 3. Firstly, the glass substrates are treated with oxygen plasma which will clean the surface and generate plenty of hydroxyl group. The trichlorovinylsilane will chemically bond to the substrates. The concentration of the trichlorovinylsilane and the reaction time is carefully controlled; otherwise multi-layer of silica network will form (Fig. 2.10), characterized by XPS results with increasing silicon content. The presence of the carbon double bond in the trichlorovinylsilane will be cross-linked with the poly-butadiene chain during the thermal cross-linking condition. Therefore, the film stays on the substrate during the PDMS wet etching step.

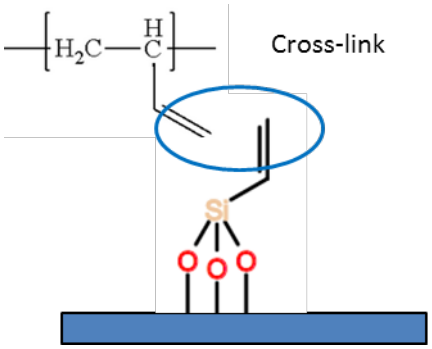

Scheme 3. Schematic illustration of the surface anchoring reaction to fix the template on the substrates.

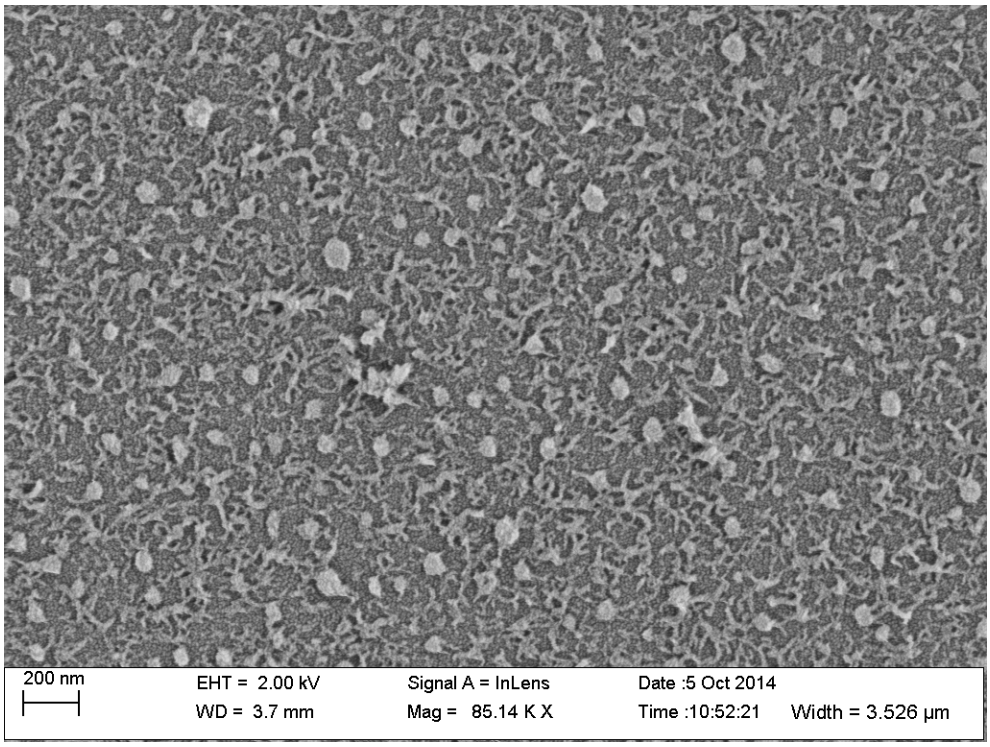

Figure 2.10. SEM image of the surface of the FTO substrate after 30 minutes Silanation reaction.

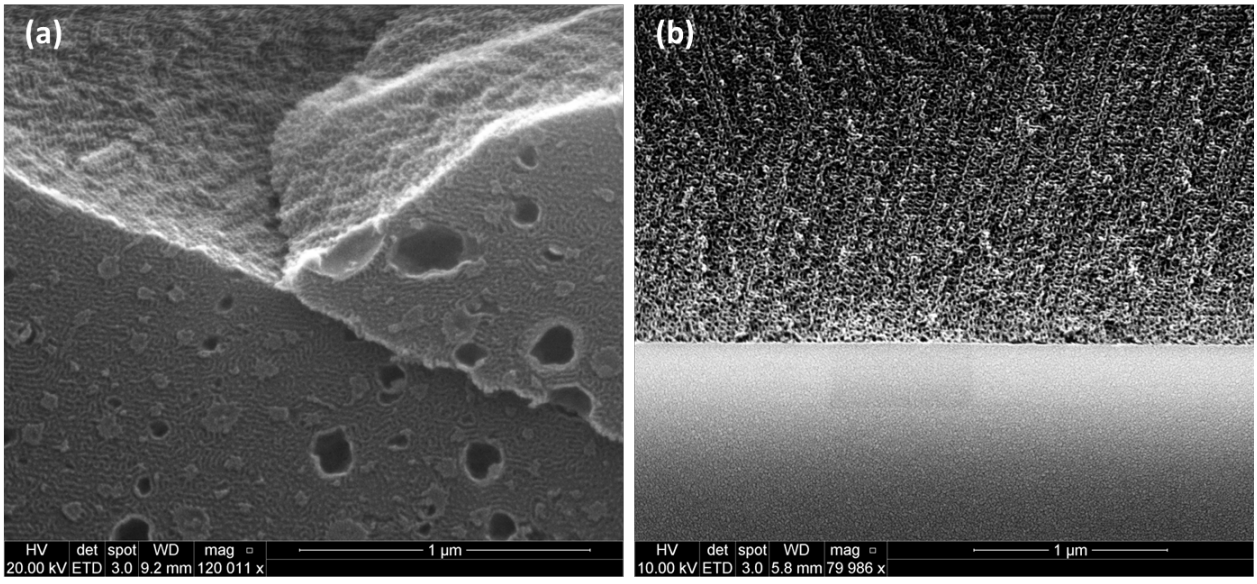

Figure 2.11. SEM image of (a) the interface to the substrate of the template and (b) cross-section of the template on Pyrex substrate.

The BCP self-assembly can behave quite differently in the bulk and at the substrate interface. It is very critical that the porous channel is continuous through the entire film, especially at the interface with the substrate. Fig. 2.11a shows the side towards to the substrate of the template by scratching the film out of the substrate, which shows gyroid characteristic morphology, indicating the change of the substrate (Silanation reaction) doesn't affect the BCP self-assembly. Fig. 2.12b shows the cross-section the gyroid template on Pyrex substrate, and no crack or detachment can be found.

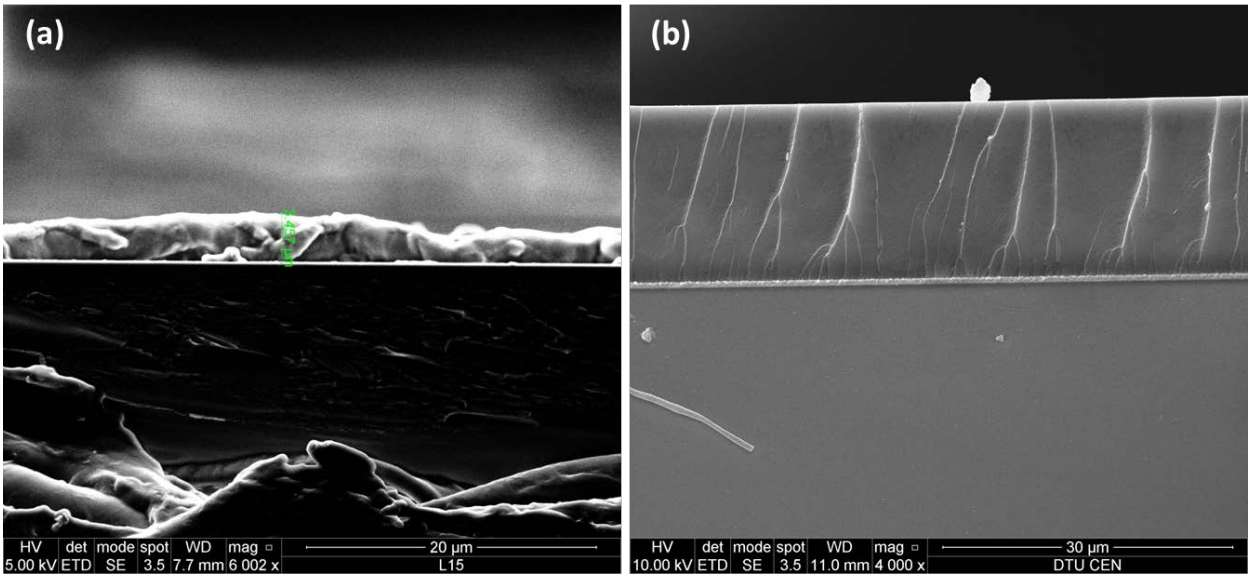

Figure. 2.12. SEM image of the film with a thickness (a) around 3 um and (b) around 30 um, using the DCP concertation of 1% relative to the BCP.

When the film thickness is below 5 um, another problem comes up as the film collapse after PDMS removal (Fig. 2.12a). This is suspected due to the low boiling point (130^{o}C) of the cross-linker. When the film is very thin, it is very likely that the DCP already evaporate before cross-linking the carbon double bond, especially when the top surface is open to air. To address this

problem, the concentration of the DCP is increased to 3% relative to the BCP and luckily this increase didn't affect the BCP self-assembly.

It is also essential that the top surface is fully open and continuous. It is well-known that due to the low surface energy of PDMS, a wetting layer of PDMS preferential cover the top surface. Two approaches have been performed to address this issue, as shown in scheme 4. Firstly, just after spin casting, a glass slide is physically attached onto the film by hand-pushing and therefore a continuous morphology is expected since the top surface is contacted with a neutral surface. However, after the PDMS removal some area of the tin film is detached. Secondly, it is found that the direct TBAF etching is enough to remove all the PDMS through the defect in the top PB layer. And the following oxygen plasma etching will remove the irregular top layers. The final results are shown in Fig. 2.13.

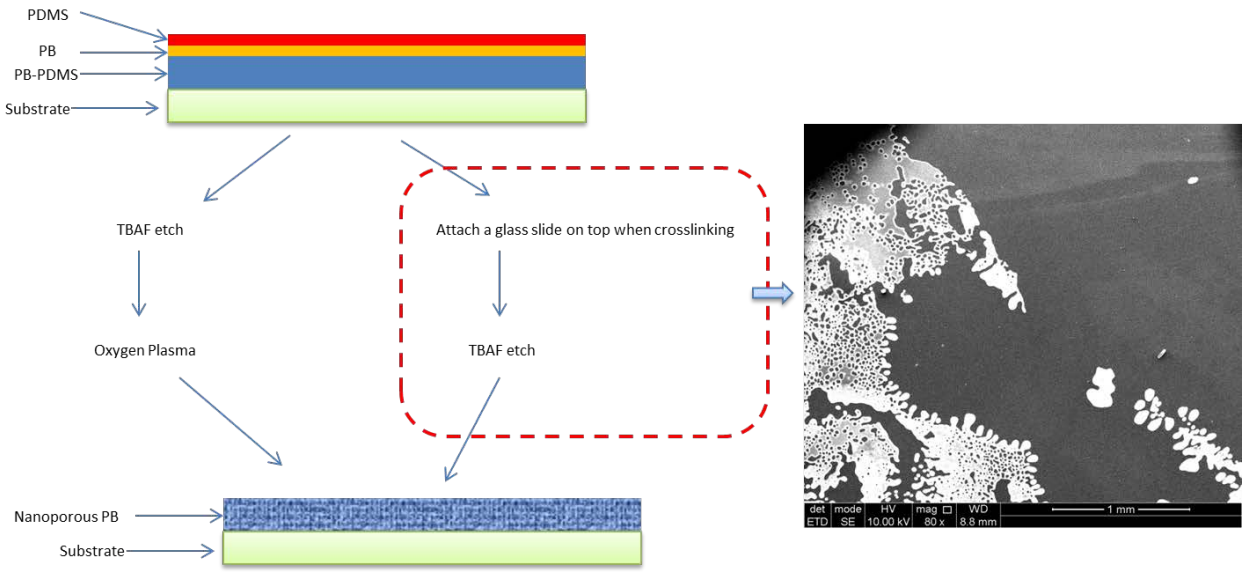

Scheme. 4. Two approaches are performed for thin film (less than 2 um) template.

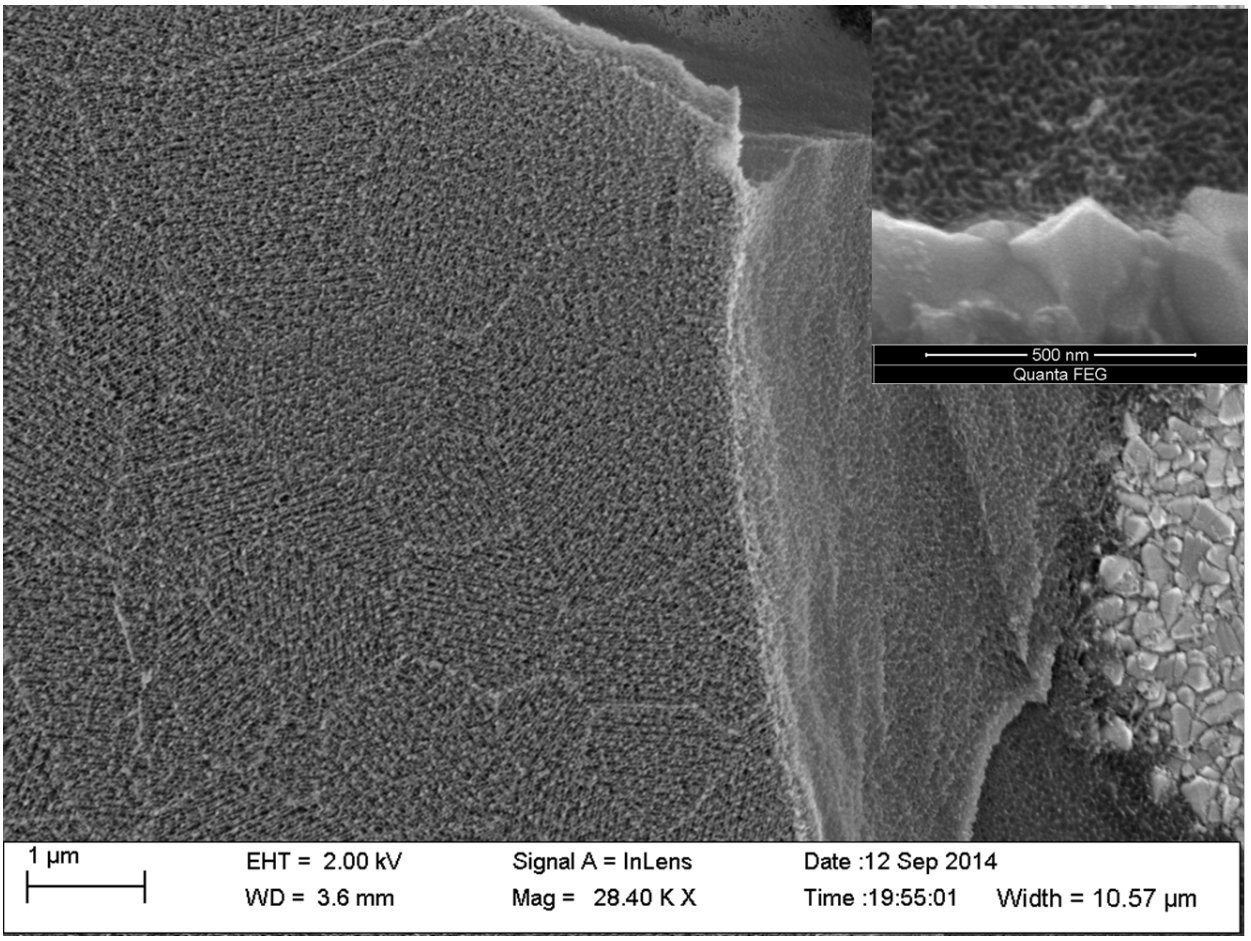

Figure 2.13. SEM image of the cross-linked nanoporous PB template on FTO substrate. Insets: SEM cross-section image

The template is used to replicate TiO2 thin film by melt infiltration method discussed in last section and overall fabrication process is shown in scheme 5. However, after calcination, cracks are observed in Fig. 2.14a, even though the desired nanoporous film is seen in Fig. 2.14b of the "good" area. The cracks are due to the insufficient precursor loading in this method. And I no longer think this method is practical for this purpose.

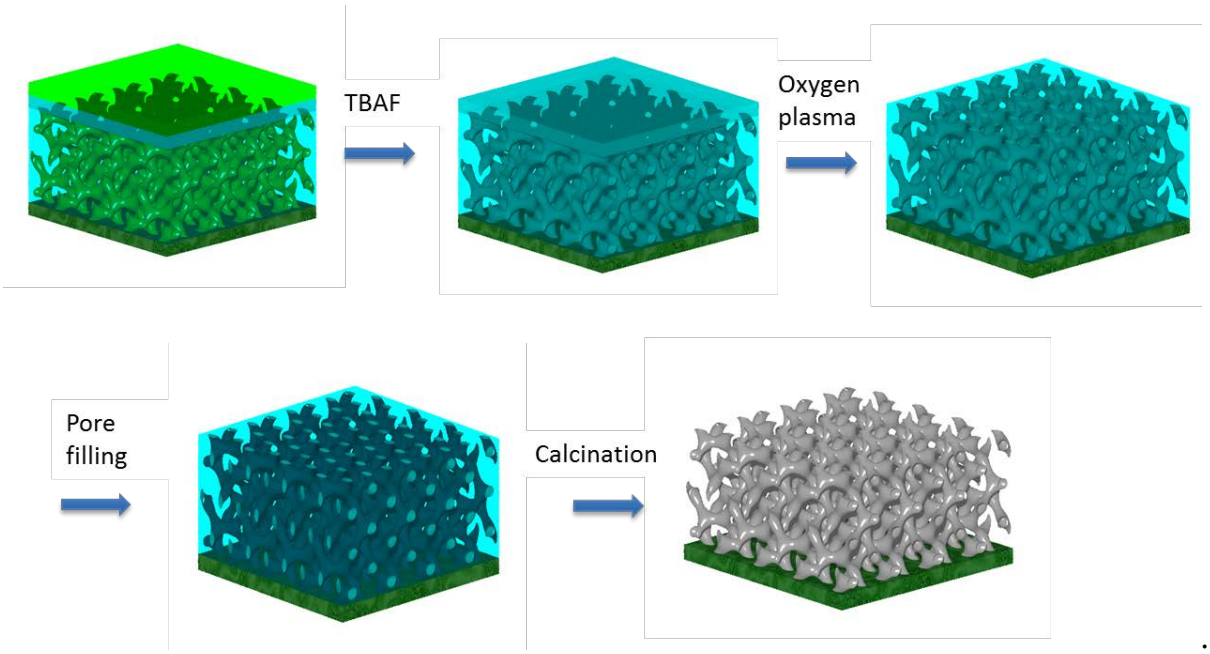

Scheme 5. Overall fabrication process of gyroid semiconductor on substrate by melt infiltration.

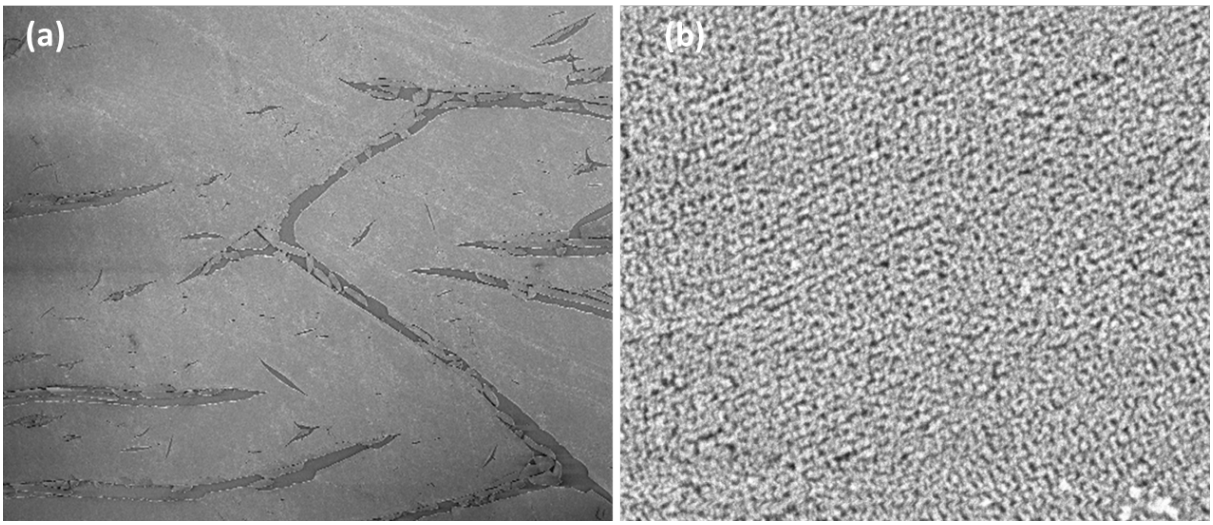

Figure 2.14. SEM image of the TiO2 film on Pyrex substrate after calcination.

2.4 Gyroid TiO_2 and Al_2O_3 prepared by ALD

Introduction: The limited precursor loading efficiency by melt infiltration drives the seeking for other replication techniques. Ideally the nano-pore is filled by the final product completely which does not involve a precursor transformation process. Atomic layer deposition (ALD) is a thin film deposition technique that is based on the sequential use of a gas phase chemical process. The ALD reactions mainly involve two chemicals, typically called precursors. These gas precursors react with the surface of a material one at a time in a sequential, self-limiting manner. Through the repeated exposure to separate precursors, a thin film is slowly deposited. In such a deposition process, a nearly 100% filling efficiency can be expected.

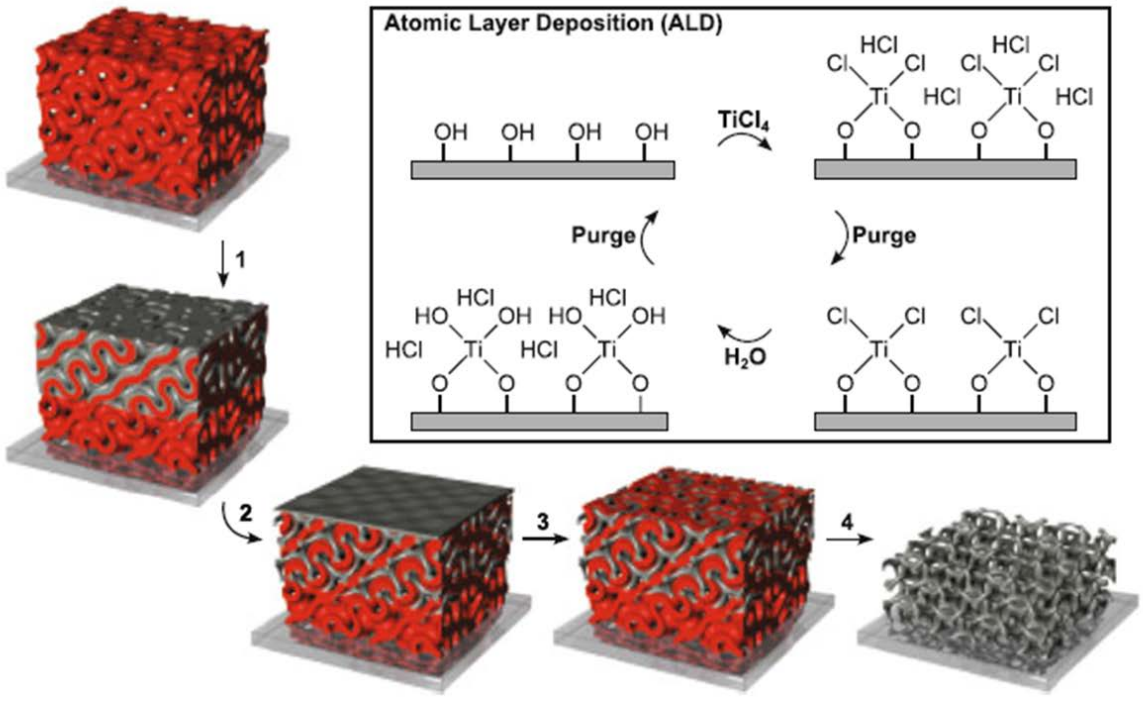

Figure. 2.15. Replication of the gyroid nanoporous template by ALD. Ref: (*39*)

Similar to the proposed route by Maik (*39*) as shown in Fig. 2.15, ALD is applied to the substrate introduced in last section is performed and discussed in this section.

Fabrication:

The ALD is conducted in Picosun ALD model R200, using alternating exposures to trimethylaluminum (97%, Aldrich)/titanium tetrachloride (99.9%, Aldrich) and deionized water. The exposure/ purge time, temperature and cycles are discussed in the results and discussion.

Characterization: Scanning electron microscopy (SEM) images are taken by a Field Emission Zeiss Ultra Plus scanning electron microscope with a Gemini column operating at an accelerating voltage of 2kV. All the samples are imaged directly without coating or staining.

Results and discussion: The template is used to replicate TiO2 thin film by ALD method discussed in last section and overall fabrication process is shown in scheme 6. The purpose of the surface functionalization step, using the same photo grafting method in the first section, is to render the PB surface with –COOH group which can initiate the surface reaction. The result is shown in Fig. 2.16, and well-defined gyroid morphology with a 1-2 nm hollow tube is observed. The high precision thickness control also can be concluded by the hollow tube structure since the deposition starts from the wall surface to the center gradually. A dense layer of TiO_2 on the top will be formed after ALD, and this can be etched away by HF dipping, as shown in Fig. 2.17. Ion beam etching is also performed to etch the dense TiO_2 top layer but the result is not good as HF dipping.

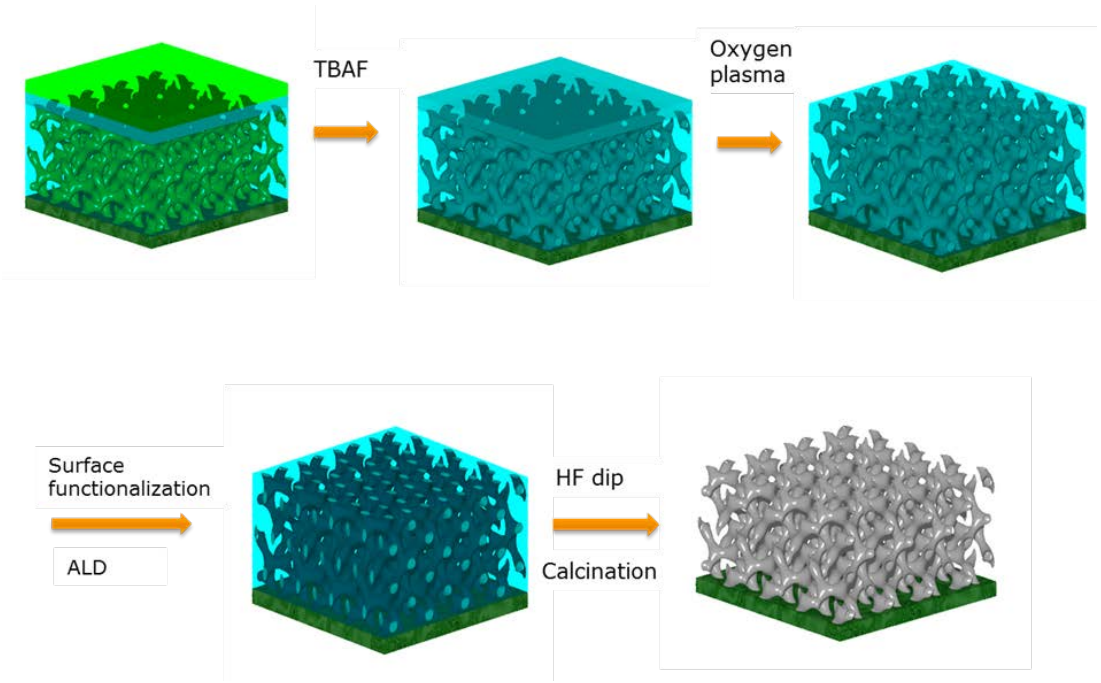

Scheme 6. Overall fabrication process of gyroid semiconductor on substrate by ALD.

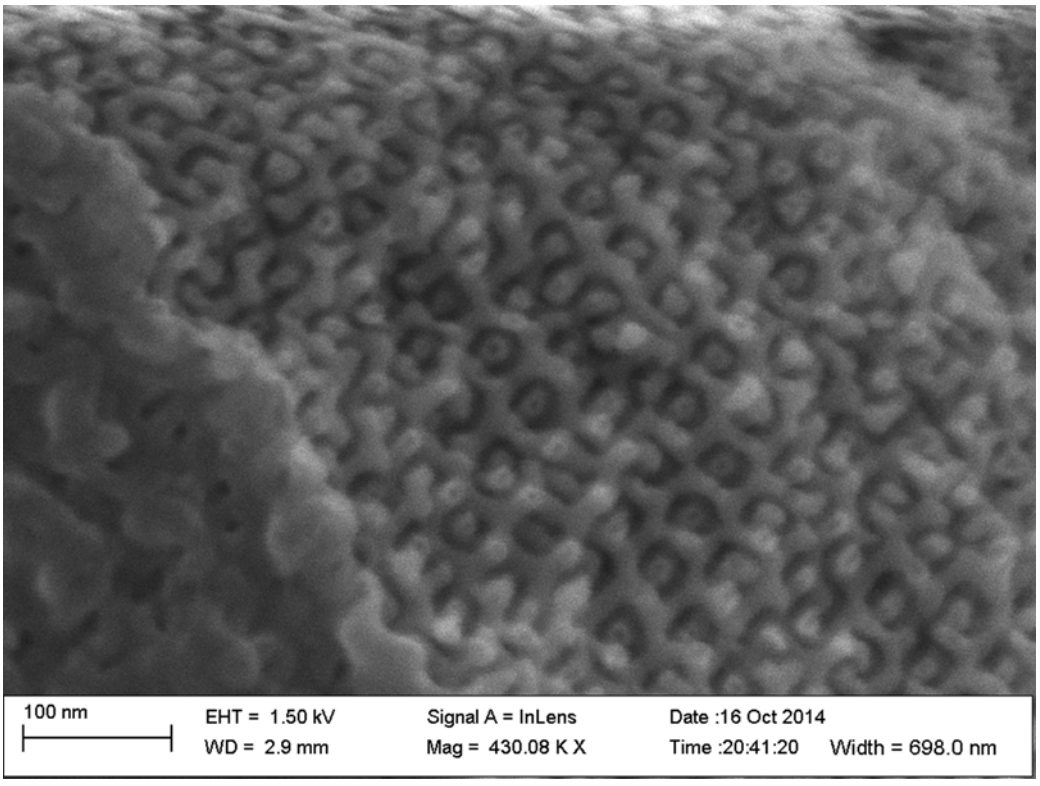

Figure 2.16. After 100 cycles of Tiania deposition, and PB is removed by oxygen plasma.

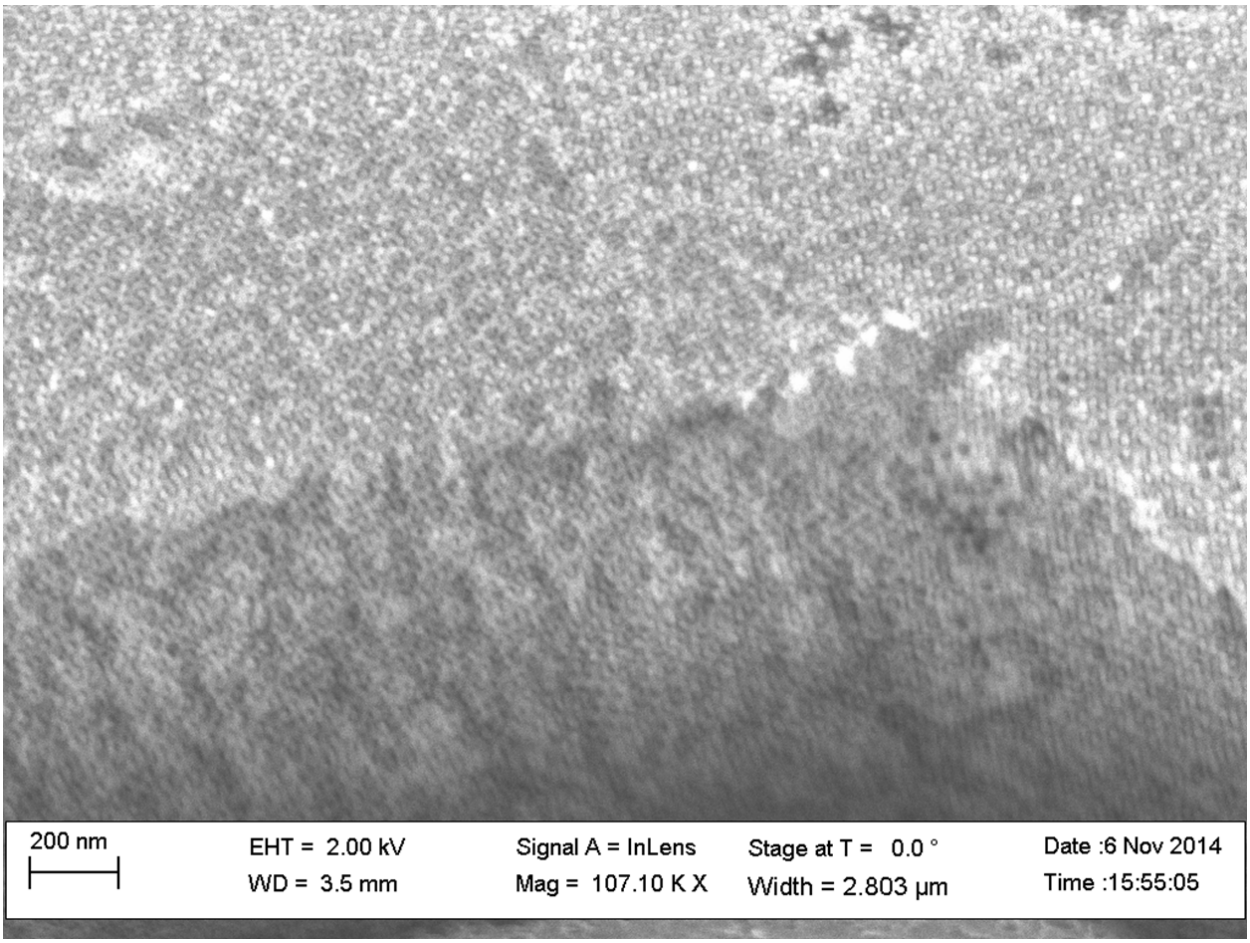

Figure 2.17. SEM images of the as-preapared gyroid TiO_2 by ALD after 5 seconds dip in HF solution (5%).

One of the challenges is the diffusion of the gas precursor molecules to the template entirely during the pulse time. In similar proposed methods (*27*), an ALD system with a "stand by" function is applied to allow sufficient long diffusion time. Unfortunately this function is missing in Danchip instrument. To address this problem, a series single precursor pulses is adopted to mimic this stand-by step as displayed in Chart 1. However, only around 600nm thickness of the gyroid TiO_2 can be obtained using a very long time recipe (exceeding 33 hours) as shown in Fig.

2.18. Various temperatures (150 ^{o}C, 200 ^{o}C and 250 ^{o}C) are also tested which make little difference.

Sequence	Precursor	Pulse time	Carrier gas	Purge time	
Pulse 1	$TiCl_4$	0.1 S	150 sccm	2 S	5
Pulse 2	$TiCl_4$	0.1 S	150 sccm	3 S	
Pulse 3	$TiCl_4$	0.2 S	200 sccm	60 S	150
Pulse 4	H_2O	0.2 S	200 sccm	2 S	5
Pulse 5	H_2O	0.2 S	200 sccm	3 S	
Pulse 6	H_2O	0.2 S	200 sccm	60 S	

Chart 1. Detailed ALD process parameters.

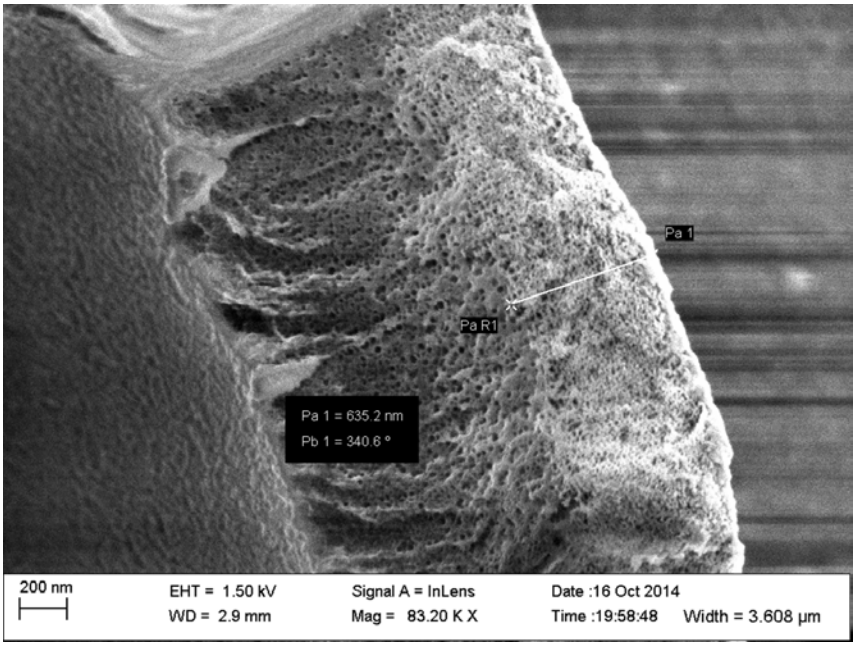

Figure. 2.18. Cross-section SEM image of the gyroid TiO_2 by ALD.

2.5 Gyroid silicon oxycarbide directly from oxygen plasma etching

In this section, an ultra-simple method is shown to fabricate gyroid nanoporous inorganic thin film on a silicon wafer by plasma etching. Under oxygen plasma, the PDMS block is converted to silicon oxycarbide while the PB block is etched away, leaving a gyroid silicon oxycarbide networks (*40*, *41*). This porous thin film may find the applications as the catalysis support and anti-reflective coating layer. The fabrication process is illustrated in scheme 7.

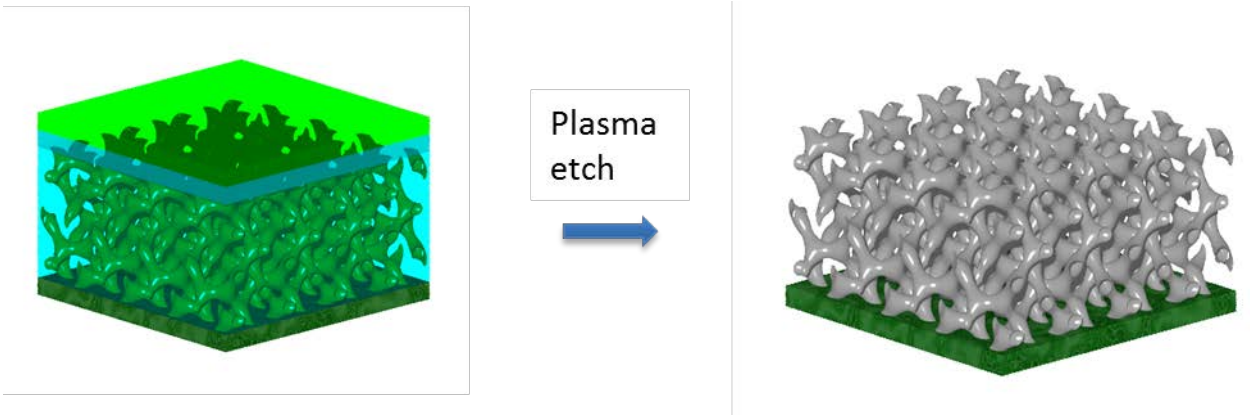

Scheme 7. Schematically illustration of the fabrication process for gyroid silicon oxycarbide directly from oxygen plasma etching

Fabrication: The silicon wafer is obtained from Danchip without any furter cleaning process. BD48 in cyclohexanxe is directly sipn-cast on it to give a thin layer between 200 nm to 2 um.

For the film with a thickness more than 400nm, a single step plasma etching is performed in the ICP tool (SPTS Serial number MP0637) using a CF_4/O_2 gas mixture based etching process: 15

sccm O_2 flowrate, 5 sccm CF_4 flowrate, 10 mTorr pressure, 300 W coil power and 20 W platen power.

For the film with a thickness less than 400nm, a two step plasma etching is performed in an Advanced Silicon Etcher (ASE, STS MESC Multiplex ICP serial no. 30343). A CF_4/O_2 gas mixture based etching process is applied to remove the irregular top layer: 10 sccm O_2 flowrate, 10 sccm SF_6 flowrate, 5 mTorr pressure, 200 W coil power and 20 W platen power for 30 seconds.

Following O_2 plasma condition to remove PB block and oxidize PDMS block: 10 sccm O_2 flow rate, 5 mTorr pressure, 100 W coil power and 5 W platen power.

Characterization: Scanning electron microscopy (SEM) images are taken by a Field Emission Zeiss Ultra Plus scanning electron microscope with a Gemini column operating at an accelerating voltage of 2kV. All the samples are imaged directly without coating or staining.

Results and discussion: To start with, BD 48 with a thickness of about 1.5 um is spin-cast on to a silicon wafer flowed by thermal crosslinking. Using a single step CF_4/O_2 gas mixture based etching process, very regular gyroid morphology is observed in Fig 2.19. CF_4 plasma will etch both PB and PDMS block. And the oxygen plasma only etch the PB block while oxidize the PDMS block into a silicon oxycarbide network. The ratio of the mixture gas is critical to ensure that the etching of the PB is faster than the PDMS etching. As a result, highly porous inorganic thin film is obtained in Fig 2.20 without defects.

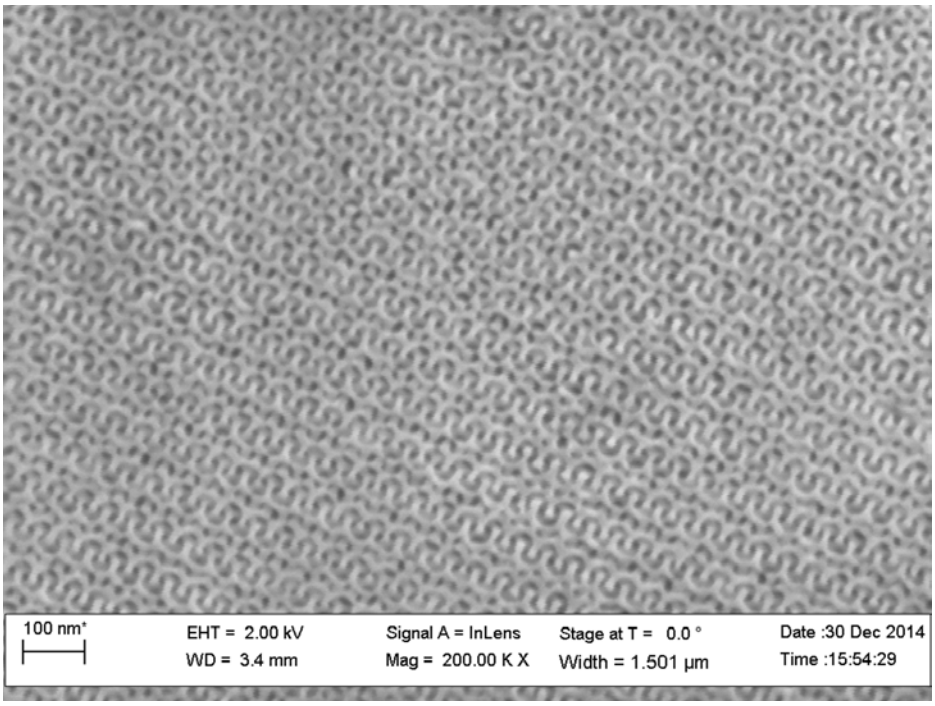

Figure. 2.19. SEM image of the BD48 thin film on silicon substrates after the CF_4/O_2 plasma treatment.

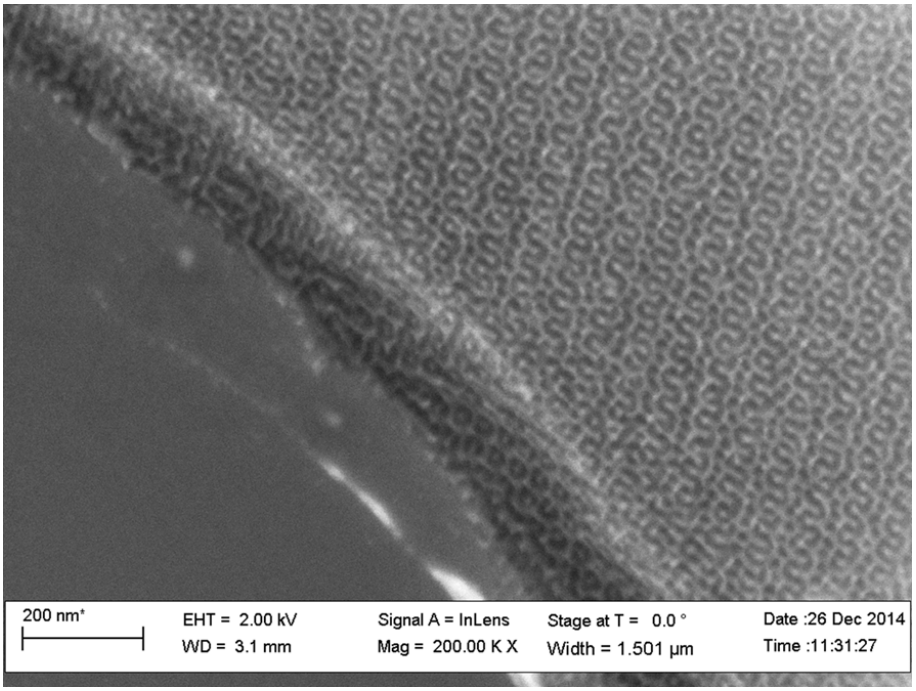

Figure. 2.20. SEM image of the BD48 thin film on silicon substrates after the CF_4/O_2 plasma treatment.

By this method, maximum 200 nm thickness can be achieved starting with an original film thickness above 1 um. It makes much more sense to remove the very 30 nm irregular top layer by CF_4/O_2 plasma treatment and then using only oxygen plasma to remove the PB domain while oxidize the entire remaining PDMS domain with a starting film thickness less than 1 um. However, the BCP self-assembly behavior is very different with the thicker film as shown in Fig 2.21: mixed morphology constantly presents (Fig 2.22). It is found that the heat transfer and DCP evaporation play have to be carefully adjusted to ensure a defect-free/gyroid-only film. Simply by increasing the DCP concentration is not enough since the film is so thin. To address this issue, the sample is put into a small glass jar with DCP powders around so that the DCP vapor can be easily saturated during heating to reduce the DCP evaporation from the thin film. However, the thick glass barrier of the sample between the sample and steel vessel. Therefore, the glass jar is abandoned and DCP is directly put into the vessel.

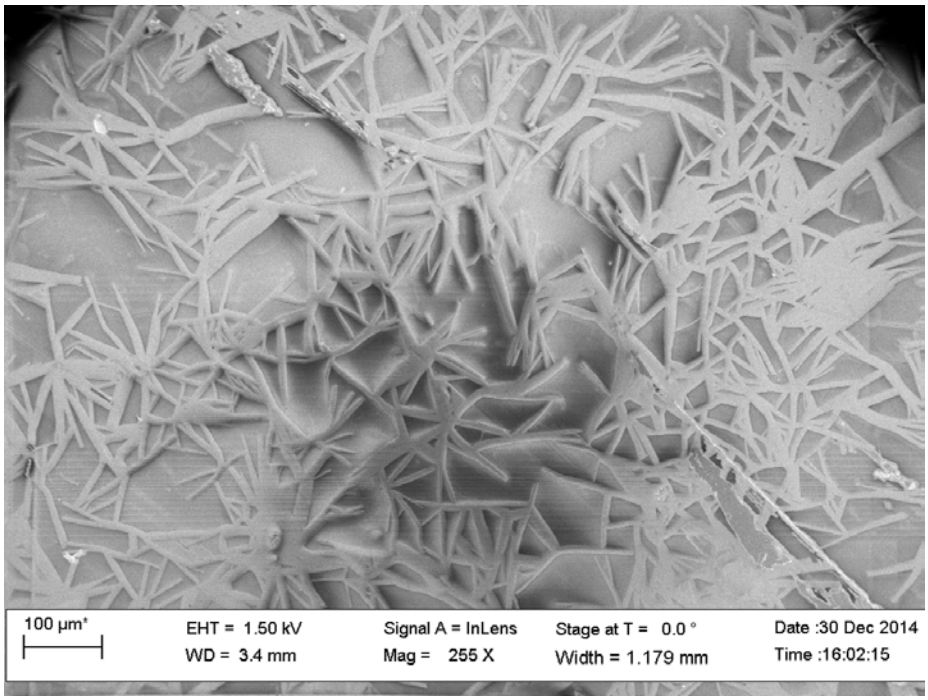

Figure. 2.21. SEM image of the BD48 thin film after thermal annealing and cross-linking.

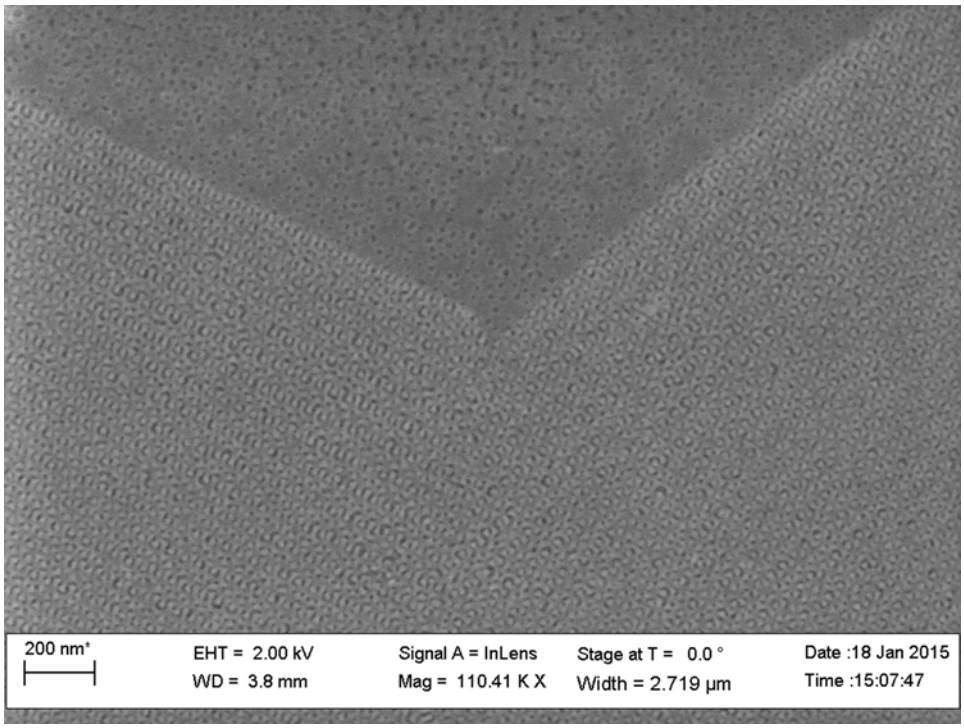

Figure. 2.22. SEM image of the BD48 thin film after thermal annealing and cross-linking.

In the new thermal annealing and cross-linking set-up, a reliable result can be obtained. But still, the oxygen plasma etching step needs to be controlled carefully. Even a mild oxygen plasma condition can damage the porous inorganic networks, as shown in Fig 2.23. Especially the platen power needs to be low since it dictates the degree of ion bombardment energy. An ideal scenario is to mimic an iso-tropic etching process so that the damage to the porous gyroid silicon oxycarbide is minimized. However, during the optimization process, the BD48 supply is run out of use. Instead, a BCP blend of BD45 and BD49 is applied. Although the bulk morphology shows relatively decent gyroid morphology, when the thin film is applied, the self-assembly process becomes unreliable similar the mixed morphology of BD48 using un-modified experiment set-up.

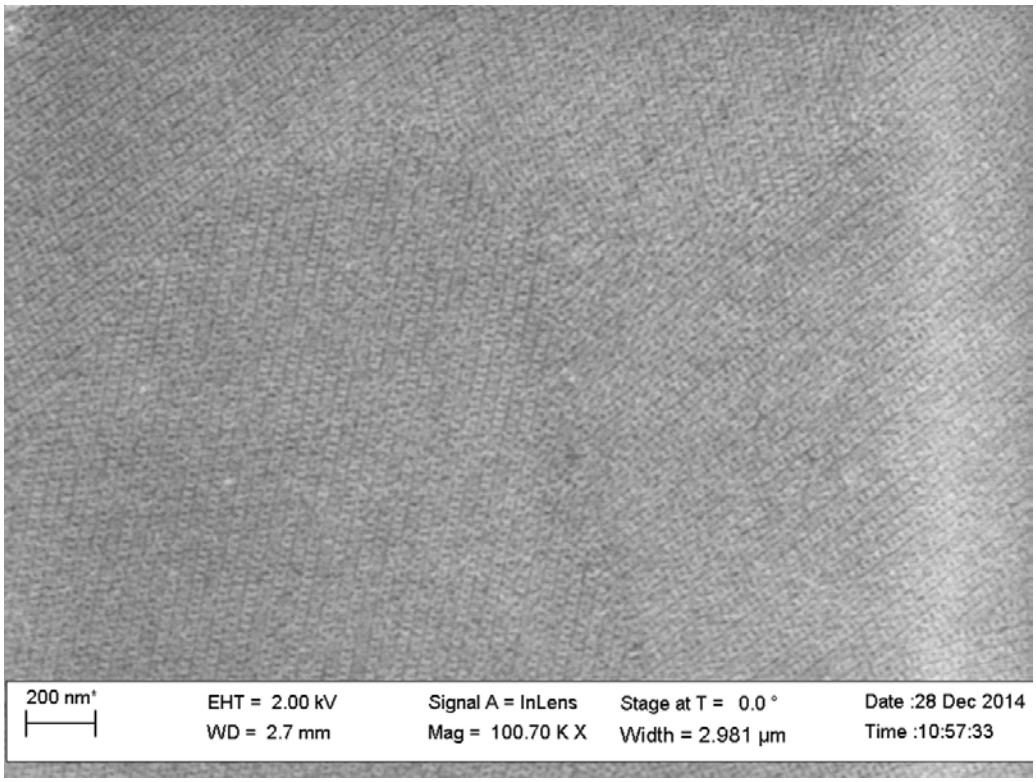

Figure. 2.23. SEM image of the BD48 thin film treated with oxygen plasma using the coil power of 200w and platen power 20w.

The disadvantage of PB-PDMS self-organization is due to its rubbery nature. In the thermal annealing process, the gyroid morphology needs to be captured by cross-linking which complicates the whole process. It is thought that another system like PS-PDMS which is glassy below 100 C will not need this cross-linking process. And thus KA7 (*42*), which is PS-PDMS with gyroid morphology, is tested using the same strategy. Fig 2.24 shows the result: the gyroid morphology is clearly visible after a simple thermal treatment; however, the structure of the obtained gyroid silicon oxycarbide networks is damaged. This is due to its extremely low molecular weight (8.2 kg/mol), which makes it mechanically vulnerable at this small length scale.

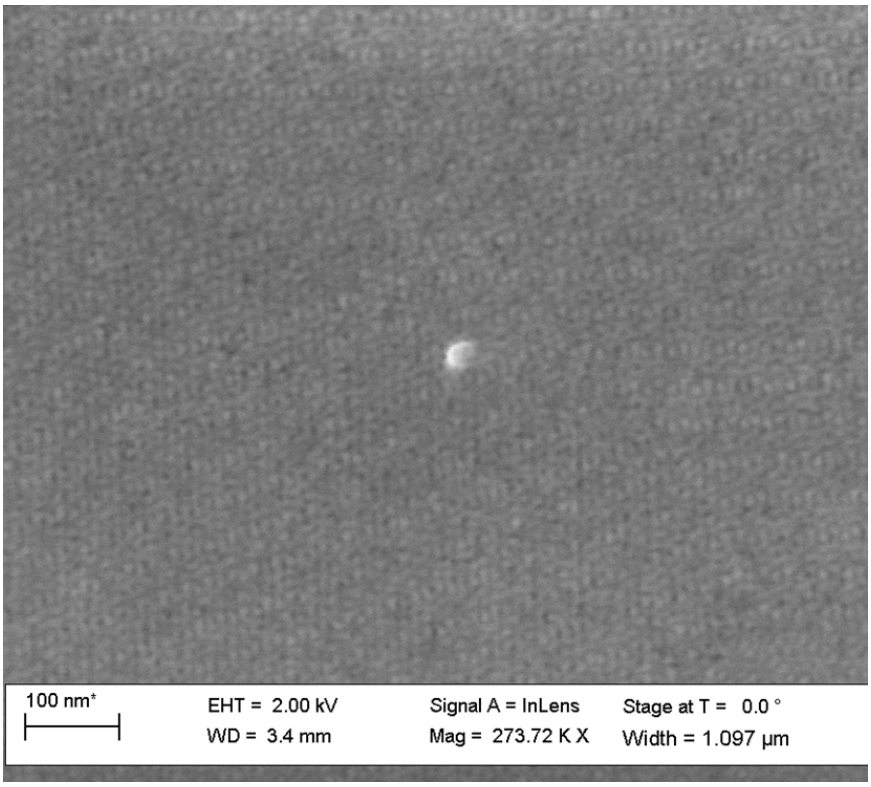

Figure. 2.24. SEM image of the KA7 thin film annealed at 150 C for 1 hour and then treated with plasma.

2.6 Concluding remarks

Firstly, a unique and facile replication method by melt infiltration is developed to manufacture of free-standing nanoporous gyroid semiconductors (TiO_2 and SnO_2). To make it grow on a functional substrate, an efficient surface modification technique is introduced to chemically bond the polymer template. ALD replication is used for a better final product loading efficiency and extraordinary gyroid morphology of TiO_2 is produced. However the film thickness is too low for many applications such as solar cells. It is a pity that the ALD facility can't enable a standby function for more efficient precursor diffusion though the high-aspect-ration channel of the

gyroid template. Otherwise this PB template is ideal for ALD replication since the matrix is cross-linked for a normal ALD working temperature and easy surface functionalization. In the last, an extremely simple procedure to make 3D nanoporous structure is developed. But due to the complicate self-assembly behavior of PB-PDMS at thermal annealing and cross-linking process when the film thickness is very thin, the results are not very reproducible. A gyroid PS-PDMS system may solve the problem.

2.7 References

1. E. J. W. Crossland *et al.*, A Bicontinuous Double Gyroid Hybrid Solar Cell. *Nano Lett* **9**, 2807 (Aug, 2009).
2. M. Gratzel, Photoelectrochemical cells. *Nature* **414**, 338 (Nov 15, 2001).
3. E. Ramasamy, J. Lee, Ordered mesoporous Zn-doped SnO2 synthesized by exotemplating for efficient dye-sensitized solar cells. *Energ Environ Sci* **4**, 2529 (Jul, 2011).
4. G. Kim *et al.*, TiO2 nanodisks designed for Li-ion batteries: a novel strategy for obtaining an ultrathin and high surface area anode material at the ice interface. *Energ Environ Sci* **6**, 2932 (Oct, 2013).
5. F. Huang, Z. Y. Yuan, H. Zhan, Y. H. Zhou, J. T. Sun, A novel tin-based nanocomposite oxide as negative-electrode materials for Li-ion batteries. *Mater Lett* **57**, 3341 (Jul, 2003).
6. M. Adachi, Y. Murata, M. Harada, S. Yoshikawa, Formation of titania nanotubes with high photo-catalytic activity. *Chem Lett*, 942 (Aug 5, 2000).
7. D. Kohl, Function and applications of gas sensors. *J Phys D Appl Phys* **34**, R125 (Oct 7, 2001).
8. M. Q. Li, C. K. Ober, Block copolymer patterns and templates. *Mater Today* **9**, 30 (Sep, 2006).
9. B. D. Gates *et al.*, New approaches to nanofabrication: Molding, printing, and other techniques. *Chem Rev* **105**, 1171 (Apr, 2005).
10. B. Z. Tian *et al.*, Self-adjusted synthesis of ordered stable mesoporous minerals by acid-base pairs. *Nat Mater* **2**, 159 (Mar, 2003).
11. J. H. Pan, S. Y. Chai, C. Lee, S. E. Park, W. I. Lee, Controlled formation of highly crystallized cubic and hexagonal mesoporous SnO2 thin films. *J Phys Chem C* **111**, 5582 (Apr 19, 2007).
12. P. Docampo *et al.*, Triblock-Terpolymer-Directed Self-Assembly of Mesoporous TiO2: High-Performance Photoanodes for Solid-State Dye-Sensitized Solar Cells. *Adv Energy Mater* **2**, 676 (Jun, 2012).

13. Y. H. Deng, J. Wei, Z. K. Sun, D. Y. Zhao, Large-pore ordered mesoporous materials templated from non-Pluronic amphiphilic block copolymers. *Chem Soc Rev* **42**, 4054 (2013).
14. M. Park, C. Harrison, P. M. Chaikin, R. A. Register, D. H. Adamson, Block copolymer lithography: Periodic arrays of similar to 10(11) holes in 1 square centimeter. *Science* **276**, 1401 (May 30, 1997).
15. T. Thurn-Albrecht *et al.*, Nanoscopic templates from oriented block copolymer films. *Adv Mater* **12**, 787 (Jun 2, 2000).
16. A. S. Zalusky, R. Olayo-Valles, J. H. Wolf, M. A. Hillmyer, Ordered nanoporous polymers from polystyrene-polylactide block copolymers. *J Am Chem Soc* **124**, 12761 (Oct 30, 2002).
17. T. Xu *et al.*, Block copolymer surface reconstuction: A reversible route to nanoporous films. *Adv Funct Mater* **13**, 698 (Sep, 2003).
18. F. Guo, K. Jankova, L. Schulte, M. E. Vigild, S. Ndoni, One-step routes from di- and triblock copolymer precursors to hydrophilic nanoporous poly(acrylic acid)-b-polystyrene. *Macromolecules* **41**, 1486 (Feb 26, 2008).
19. J. Y. Cheng *et al.*, Formation of a cobalt magnetic dot array via block copolymer lithography. *Adv Mater* **13**, 1174 (Aug 3, 2001).
20. M. R. J. Scherer, L. Li, P. M. S. Cunha, O. A. Scherman, U. Steiner, Enhanced Electrochromism in Gyroid-Structured Vanadium Pentoxide. *Adv Mater* **24**, 1217 (Mar 2, 2012).
21. J. Kibsgaard, Z. B. Chen, B. N. Reinecke, T. F. Jaramillo, Engineering the surface structure of MoS2 to preferentially expose active edge sites for electrocatalysis. *Nat Mater* **11**, 963 (Nov, 2012).
22. S. Ndoni *et al.*, Controlled Photooxidation of Nanoporous Polymers. *Macromolecules* **42**, 3877 (Jun 23, 2009).
23. I. Vukovic *et al.*, Supramolecular Route to Well-Ordered Metal Nanofoams. *Acs Nano* **5**, 6339 (Aug, 2011).
24. H. Y. Hsueh *et al.*, Nanoporous Gyroid Nickel from Block Copolymer Templates via Electroless Plating. *Adv Mater* **23**, 3041 (Jul 19, 2011).
25. H. Y. Hsueh, R. M. Ho, Bicontinuous Ceramics with High Surface Area from Block Copolymer Templates. *Langmuir* **28**, 8518 (Jun 5, 2012).
26. H. Y. Hsueh *et al.*, A polymer-based SERS-active substrate with gyroid-structured gold multibranches. *J Mater Chem C* **2**, 4667 (2014).
27. E. Kim *et al.*, Gyroid-Structured 3D ZnO Networks Made by Atomic Layer Deposition. *Adv Funct Mater* **24**, 863 (Feb, 2014).
28. P. E. de Jongh, T. M. Eggenhuisen, Melt Infiltration: an Emerging Technique for the Preparation of Novel Functional Nanostructured Materials. *Adv Mater* **25**, 6672 (Dec, 2013).
29. L. Schulte *et al.*, Nanoporous materials from stable and metastable structures of 1,2-PB-b-PDMS block copolymers. *Polymer* **52**, 422 (Jan 21, 2011).
30. K. Sagar, N. Gopalakrishnan, M. B. Christiansen, A. Kristensen, S. Ndoni, Photolithographic fabrication of solid-liquid core waveguides by thiol-ene chemistry. *J Micromech Microeng* **21**, (Sep, 2011).
31. L. Li *et al.*, Ultrafiltration by gyroid nanoporous polymer membranes. *J Membrane Sci* **384**, 126 (Nov 15, 2011).

32. L. Li *et al.*, Gyroid Nanoporous Membranes with Tunable Permeability. *Acs Nano* **5**, 7754 (Oct, 2011).
33. R. C. Furneaux, W. R. Rigby, A. P. Davidson, The Formation of Controlled-Porosity Membranes from Anodically Oxidized Aluminum. *Nature* **337**, 147 (Jan 12, 1989).
34. J. K. Shon *et al.*, Solvent-free infiltration method for mesoporous SnO2 using mesoporous silica templates. *Micropor Mesopor Mat* **120**, 441 (Apr 15, 2009).
35. E. Ramasamy, J. Lee, Ordered Mesoporous SnO2-Based Photoanodes for High-Performance Dye-Sensitized Solar Cells. *J Phys Chem C* **114**, 22032 (Dec 23, 2010).
36. F. X. Guo, J. W. Andreasen, M. E. Vigild, S. Ndoni, Influence of 1,2-PB matrix cross-linking on structure and properties of selectively etched 1,2-PB-b-PDMS block copolymers. *Macromolecules* **40**, 3669 (May 15, 2007).
37. R. Al-Gaashani, S. Radiman, N. Tabet, A. R. Daud, Optical properties of SnO2 nanostructures prepared via one-step thermal decomposition of tin (II) chloride dihydrate. *Mater Sci Eng B-Adv* **177**, 462 (Apr 15, 2012).
38. P. Silberzan, L. Leger, D. Ausserre, J. J. Benattar, Silanation of Silica Surfaces - a New Method of Constructing Pure or Mixed Monolayers. *Langmuir* **7**, 1647 (Aug, 1991).
39. M. R. J. Scherer, (2013).
40. K. Fukukawa, L. Zhu, P. Gopalan, M. Ueda, S. Yang, Synthesis and characterization of silicon-containing block copolymers from nitroxide-mediated living free radical polymerization. *Macromolecules* **38**, 263 (Jan 25, 2005).
41. A. Nunns, J. Gwyther, I. Manners, Inorganic block copolymer lithography. *Polymer* **54**, 1269 (Feb 18, 2013).
42. S. Ndoni, M. E. Vigild, R. H. Berg, Nanoporous materials with spherical and gyroid cavities created by quantitative etching of polydimethylsiloxane in polystyrene-polydimethylsiloxane block copolymers. *J Am Chem Soc* **125**, 13366 (Nov 5, 2003).

Chapter 3

Substrate Tolerant Direct Block Copolymer Nanolithography

3.1 Introduction

Pattern transfer at nano-scale has been the key to the modern nanotechnology. The ever growing demand for increased device functionality, higher data processing speed and larger data storage density drives the searching for new technology to fabricate electronic components with smaller dimensions. Challenges arise from the increasing cost and limited resolution of deep-UV optical lithography. On the other hands, the low throughput e-beam lithography and interference techniques are not suitable for a direct large area patterning.(*1*) BCP nanolithography is a promising platform to meet the key challenges of small feature size with high resolution and high throughput at low cost.(*2, 3*) The domain size can be controlled in the range of 5-50 nm by controlling molecular weight of the BC and the segregation strength between the blocks in the synthesis step. Various patterns with narrow size distribution and perfect alignment have been created so far;(*4-7*) however, pattern transfer process by such method is seldom demonstrated. There is still a need for a facile and versatile approach using block copolymer with large etching contrast and substrate independence to succeed in lithography process.

One of the keys to the BCP nanolithography is the out-of-plane orientation control. Among all the morphologies, perpendicular orientated lamellae or cylinders are most desirable. However, in most cases of di-block copolymer, the different surface energy of each block at both the air-BCP and the substrate-BCP interfaces makes parallel orientation preferable. Several existing

methods are developed to overcome this problem. By applying a random copolymer with controlled composition covalently bonded to the substrate, so called brush layer, a neutral surface energy for both of the polymers can be adjusted (*8*). This approach, however, requires anchoring chemical groups present both in the substrate and brush polymer, which limits its application. Alternative methods including top coats (*9*), electrical fields (*10*) and solvent vapor annealing (*11*) are also reported to orient microdomains normal to the substrate.

Another challenge for BCP nanolithography is to use high Flory–Huggins interaction parameter (χ) block copolymer, which improves the ordering quality, defects levels and scalability to smaller period. So far, poly(styrene-*b*-methyl methacrylate) (PS-PMMA) is the most investigated BCP system due to the easy removal of PMMA block under UV illumination. But the low χ ($\chi_{PS\text{-}PMMA} \sim 0.06$ at 25^{o}C) of this BCP limits the possibility of reaching sub-20 nm features and the remaining PS domain has a low etching resistance under reactive ion etching (RIE), making it a poor mask for pattern transfer process. One major route to increase χ and generate hard mask is to incorporate inorganic domain which is highly incompatible with the organic block. For an example, poly(styrene-*b*-dimethylsiloxane) (PS−PDMS) gains intensive research interest due to its high segregation strength ($\chi_{PS\text{-}PDMS} \sim 0.27$ at 25^{o}C) and large etching contrast (*12, 13*). Under oxygen plasma, the PDMS block is converted to silicon oxy carbide while the PS block is etched away, leaving a hard mask with much more enhanced thermal stability and mechanical strength (*14*, *15*). However, the orientation control of PS-PDMS microdomains is notoriously challenging due to the high surface energy mismatch between the two blocks (*9*). As a result, a top-wetting layer of PDMS preferably form at the air-BCP interface, and a PS or PDMS brush layer is usually needed to balance the surface energy. By far most of the studies are focused on PS-rich

BCP, and yet, PDMS-rich BCP, which is more desired for pattern transfer process to make iso-porous nano-channels, is seldom reported (*16, 17*).

Block copolymer (BC) self-assembly constitutes a powerful platform for nanolithography. However, there is a need for a general approach to BC lithography that critically considers all the steps from substrate preparation to the final pattern transfer. Here a procedure is presented that significantly simplifies the main stream BC lithography process, showing a broad substrate tolerance and allowing for efficient pattern transfer over wafer scale. We demonstrate the procedure by using four PDMS-rich poly(styrene-b-dimethylsiloxane) (PS-b-PDMS) copolymers. By combining large inter-block segregation with high etching contrast; PS-b-PDMS is strong candidate for sub-10 nm lithography. The masks are directly applied on substrates with broadly varying surface energy, including polymers, silicon and graphene, thus bypassing the laborious and delicate substrate chemical pre-modification found in nearly all the reports in the field. The perpendicular orientation of the PS cylinders in the sub-20 nm thin films is kinetically captured by annealing in vapors of selective solvents relative to the PDMS block. A single oxygen plasma treatment enables formation of the oxidized PDMS hard mask, PS block removal and polymers or graphene substrate patterning. Last but not least we demonstrate an efficient pattern transfer to silicon under the *in situ* hardened mask. Our procedure differs fundamentally from the main stream BC lithography in general and from SD based lithography in particular, by combining kinetic control, sub-lattice thickness confinement and selective solvent annealing as the key elements. The preliminary surface modification, including the grafting of a neutral polymer brush layer onto the substrate,(*18*) is the result of thinking thin film BC self-assembly in terms of equilibrium. Uneven BC swelling under selective solvent vapor is known to shift the morphology

by changing the effective volume fraction,(*19*, *20*) which opens up the process window for capturing the targeted morphology kinetically. To our best knowledge, this is the first report on highly ordered PDMS-rich BC masks with perpendicular cylindrical orientation, which shows unparalleled simplicity and applicability in block copolymer nanolithography. The lithography process is schematically illustrated in Scheme. 1.

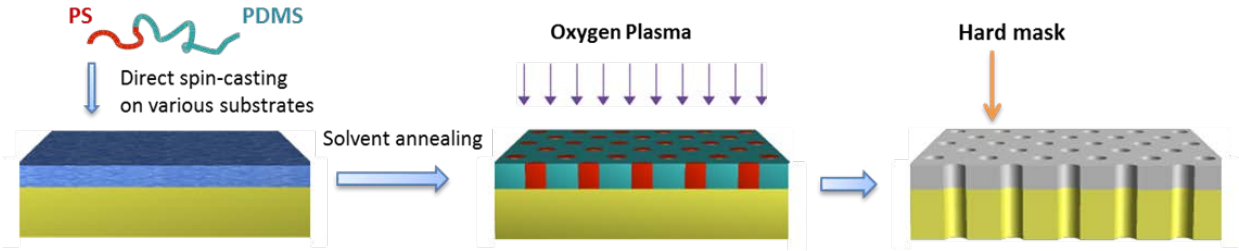

Scheme 1. Schematic workflow of direct BCs nanolithography. SDs are directly cast on various substrates including PS, PLA PMMA, PSF cross-linked PB, graphene, InP and silicon.

3.2 Pattern generation

In this section, an efficient solvent vapor annealing method is introduced. The tentative mechanism is also given.

Materials: All the solvents are purchased from Sigma Aldrich without further purification (except for the BC synthesis). SD67 (21-b-46 kg mol^{-1}, Polymer Source), SD81 (26-b-55 kg mol^{-1}, Polymer Source), PS (50k, synthesized in our lab). SD42, SD34 and SD23 are synthesized by living anionic polymerization following already reported procedure.(*21*) After precipitation in methanol and vacuum drying, SD is dissolved in heptane (5wt %). Clear solutions are obtained in heptane, despite the fact that it is a nonsolvent for PS; the SDs most probably form micelles in

such conditions. However, the solutions turn turbid after a residence time of 10-20 hours, and the undissolved solids are removed by centrifugation. This step is essential for a reliable following self-assembly process, since we find that even a small amount of unreacted PS impurity makes the whole process less robust. Size exclusion chromatography (SEC) traces of the supernatant are indistinguishable from the SEC of the as synthesized SDs (except for SD34, see below), which is consistent with less than 1% of precipitated mass fraction. As synthesized SD34 shows a little but distinguishable SEC peak of uncoupled PS, which is significantly diminished after fractionation in heptane (data not shown). Most probably the PS homopolymer seeds the formation of large SD cylindrical micelles that can be removed by centrifugation.

Fabrication: The supernatant is diluted in heptane at 0.12 -0.28 wt %, giving films with thickness from 12 nm to 20 nm at spinning speed of 2000 rpm. Solvent vapor annealing is made at room temperature with the samples in a closed glass jar in the presence of chosen annealing solvent(s). The annealing time is typically up to 1 hour. Using solvents that are strongly selective to PDMS effectively prevents dewetting since the mobility of the PS block is limited, resulting in a highly controlled and reproducible process. No dewetting is observed for this study; however, using neutral solvents like toluene causes substrate dewetting in less than 2 minutes. The annealing solvents are nonsolvents for PS; however given the structural rearrangement observed these are able to slightly swell the PS block by bringing it in the rubbery state. The swelling ratio of a 10 nm PS film is measured to 1.2 – 1.24 at 40 – 75 min hexane vapor annealing time by a QCM. This degree of swelling is compatible with literature reports on PS glass transition temperature T_g decrease below room temperature.(*22*)

Characterization: ^{1}H-NMR is done in deuterated chloroform, using a 400 MHz NMR from Bruker. The SEC is done using THF as a solvent. The system from Shimadzu, LC-10AD (Pump), SIL-10AS (Autosampler), is combined with Detectors from Viscotek, namely a RALLS Detector (Model LD600) as well as a Differential Refractometer/Viscometer (Model 200) combination. The columns are: one PLgel 5µm Mixed D from Polymer Laboratories in series with one Styragel HMW 6E from Waters. The PS block of the polymers is analyzed using the Refractive Index signal in combination with a conventional calibration against PS standards, while calculations of PDI for the BCs, is done by analyzing the combined Light Scattering and Refractive Index responses. Film thickness is determined by a VASE Ellipsometer (J.A. Woollam) at three different incidence angles (55^{o}, 60^{o} and 65^{o}). Scanning electron microscopy (SEM) images are taken by a Field Emission Zeiss Ultra Plus scanning electron microscope with a Gemini column operating at an accelerating voltage of 2kV. All the samples are imaged directly without coating or staining. Atomic Force Microscopy (AFM) images are taken by an AFM Dimension Icon-PT from Bruker AXS. The annealing process is followed in situ by a quartz crystal microbalance QCM 200 digital controller connected to a QCM 25 crystal oscillating at 5 MHz from Stanford Research Systems. The block copolymer or PS 50k are spin-cast directly on the quartz crystal with a gold electrode at same conditions as for the sample preparation on the different substrates. An accuracy of better than 1 Hz, corresponding to mass differences of smaller than 0.017 ng/cm^{2} or film height changes of ~ 2 Å is routinely achieved.

Results and discussion: Four SDs with different M_n from 23.4 to 67.0 kg/mol are investigated, and their properties are summarized in Table 3.1. The PS volume fraction is in the range of 24-30%, which is within the typical composition range for cylinder bulk morphology (Figure 3.1,).

SD23, SD34 and SD42 are synthesized in our lab by living anionic polymerization with a narrow polydispersity index (PDI ≤ 1.03), and SD67 is purchased with somewhat higher PDI (1.45).

Table 3.1. PS-b-PDMS Copolymer Characteristics

Sample ID	f_{PS}	M_{PS} (kg/mol)	M_{Total} (kg/mol)	PDI	Periodicity (cylinders)[f]	Periodicity (spheres)[f]
SD23	28.6% [a]	7.1 [b]	23.4 [c]	1.02 [e]	24 nm	~ 19 nm
SD34	24.0% [a]	8.7 [b]	34.1 [c]	1.03 [e]	30 nm	~ 23 nm
SD42	28.6% [a]	12.6 [b]	41.6 [c]	1.02 [e]	33 nm	26 nm
SD67	29.7% [d]	21.0 [d]	67.0 [d]	1.45 [d]	45 nm	n.a.
SD81	30.4% [d]	26.0 [d]	81.0 [d]	1.25 [d]	55 nm	n.a

[a]Calculated from ^{1}H NMR spectra using ρ_{PDMS} = 0.97 g/cm^3 and ρ_{PS} = 1.05 g/cm^3.

[b] From SEC analysis calibrated with PS standards.

[c]Calculated from f_{PS} and M_{PS} .

[d]From the supplier (Polymer Source)

[e] From SEC analysis of the combined RI and LS signals

[f]measured from SEM image

R_g = 4.4 nm (SD23), 4.9 nm (SD34), 5.7 nm (SD42), 7.2 nm (SD67) [unperturbed conditions, calculated from statistical data, P. J. Flory Statistical Mechanics of Chain Molecules, 1969, Interscience Publ.]

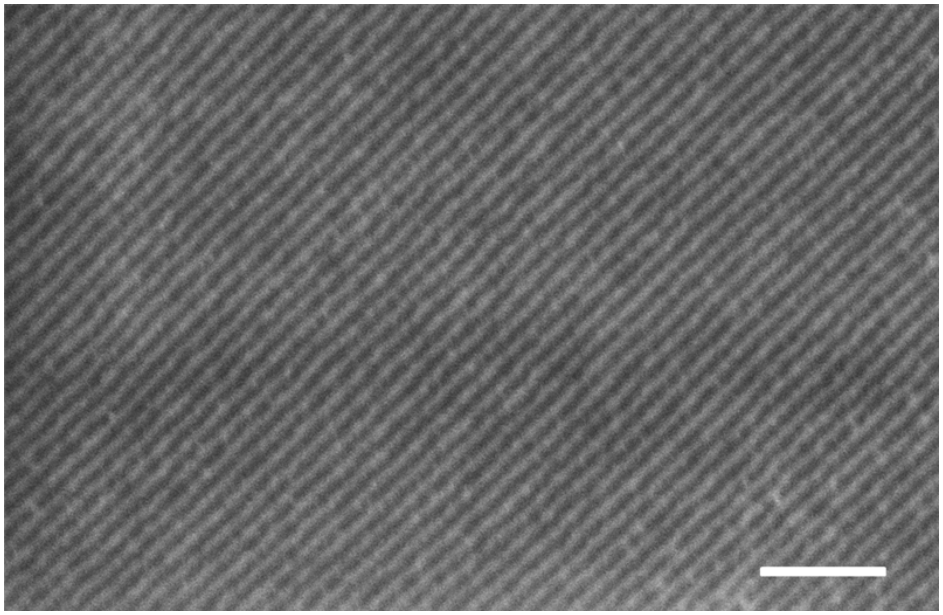

Figure 3.1. SEM image of the bulk morphology of SD23 (600 nm thick film on silicon wafer), annealed at 160^{o}C for 20 hours. The image is taken after 200 nm top layer removal by SF_6/O_2 RIE. The observed period is 29 nm and is equal to the characteristic distance between two cylinders. The corresponding period is 24 nm, which is slightly bigger than the period of thin film cylinder morphology (Table 1). Scale bar: 200nm.

SD solutions in heptane are spin-cast into sub-20 nm thin films on silicon or PS coated silicon. Figure 3.2a,b,c show the top view scanning electron microscopy (SEM) images of SD23, SD34 and SD42 after annealing. A well-ordered hexagonally packed cylinder morphology with narrow PS-cylinder size distribution is clearly seen, which can be visualized directly in SEM. A SEM image of SD67and SD81 after annealing is shown in Figure 3.2d, with the same morphology but lacking in lateral order, which might be due to its large PDI.

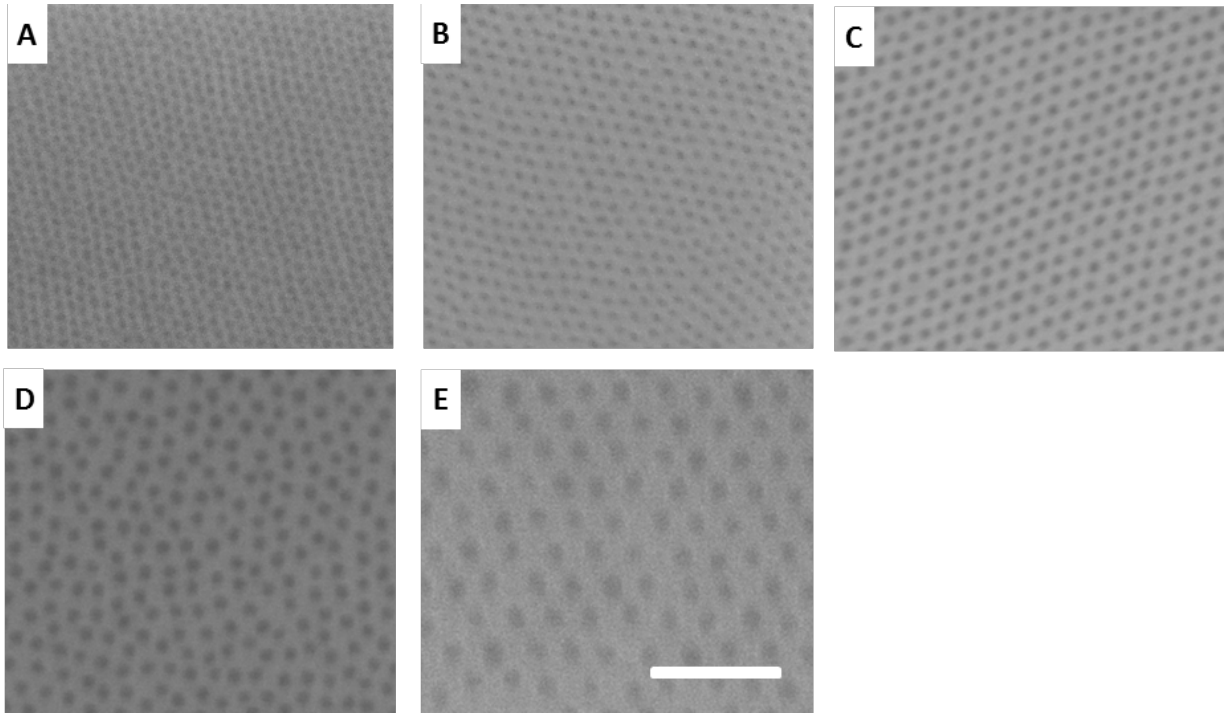

Figure 3.2. Top view SEM images of the masks after annealing: (a) SD23 annealed in TMPA for 40 minutes with a thickness of 13.5 nm, (b) SD34 annealed in TMPE for 30 minutes with a

thickness of 14.7 nm, (c) SD42 annealed in hexane for 40 minutes with a thickness of 15.8 nm, (d) SD67 annealed in 1-octene for 90 minutes with a thickness of 19.1 nm and (e) SD81 annealed in MCH for 60 minutes with a thickness of 22.1 nm. All the samples are spun-cast on a PS 50k substrate coated on silicon wafer with a thickness of around 50 nm. Scale bar: 200 nm.

Compared with the morphology of as cast films or of films after thermal annealing (Figure 3.3a,b), it is evident that the solvent annealing is effective on directing the SD self-assembly over wafer-scale with micrometer grain size (Figure 3.3c). The corresponding period (Table 1) scales with the 0.6^{th} power of BC molecular weights. A wide range of the pore size from 13 nm (SD23) to 30 nm (SD67) is obtained. General shortcomings of solvent vapor annealing, including dewetting and deformation of the structures,(*23*) are not observed in this study due to the limited PS chain mobility in the presence of a nonsolvent.

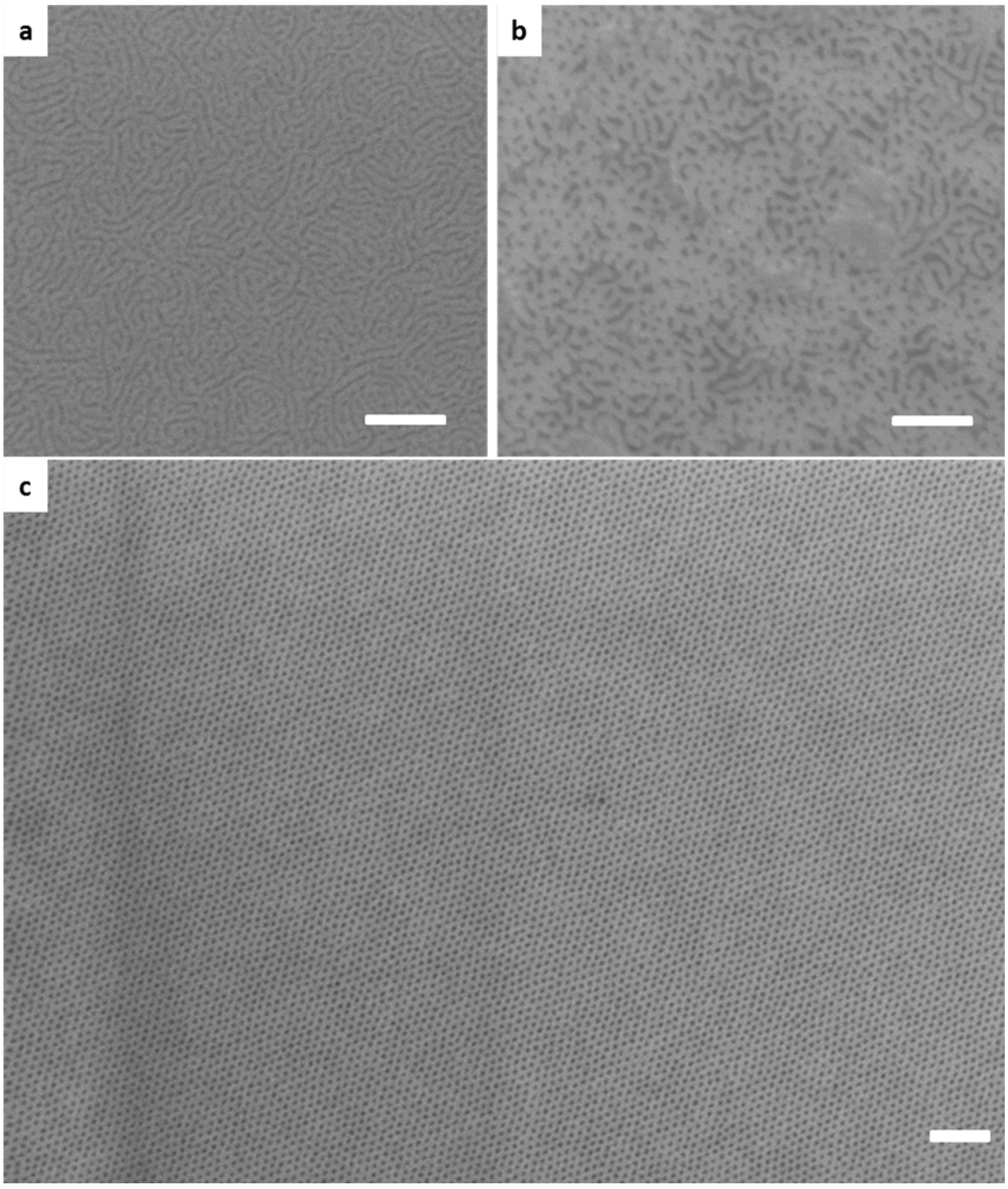

Figure 3.3 SEM image of the SD42 as cast on PS substrate a); the shown morphology is similar for all the SDs after spin-casting, b) SD42 thermal annealed at 160^{o}C for 15 hours and c) SD42 annealed in hexane for 40 minutes with the grain size exceeding 4 um. Scale bar: 200 nm.

The morphology is further confirmed by atomic force microscopy (AFM) (Figure 3.4).

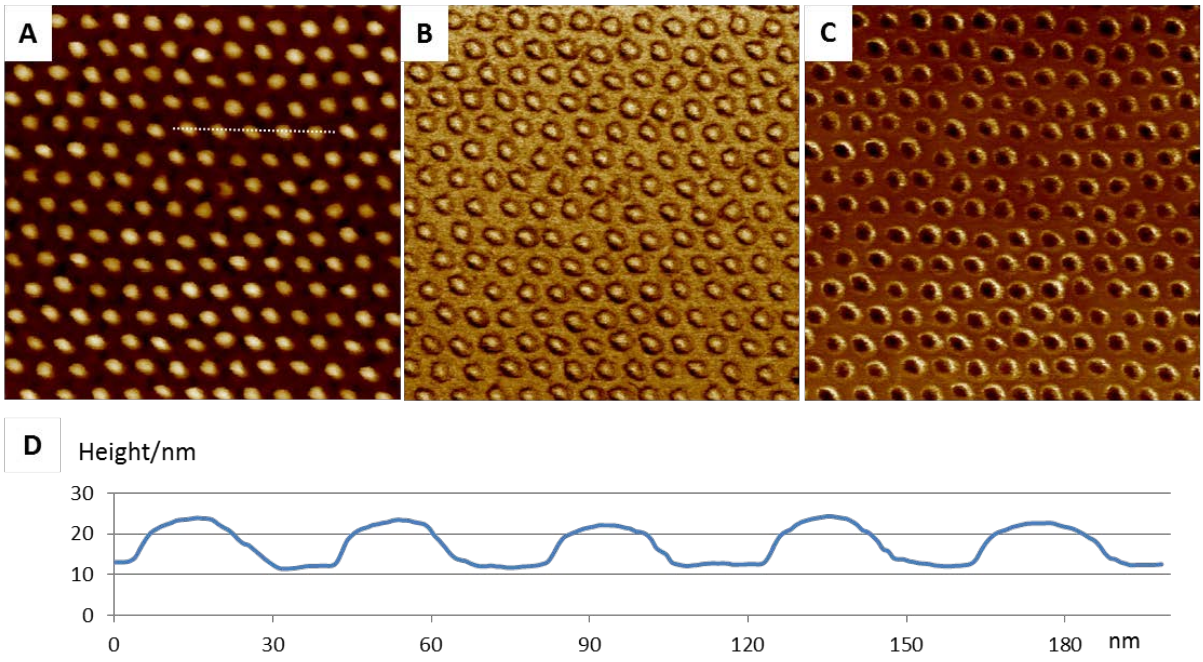

Figure 3.4. AFM image of the SD42 annealed in hexane for 40 minutes: (a) height mode, (b) modulus mode, (c) adhesion mode and (d) section profile of (a); size: 500nm x 500nm.

The interaction between the solvent and polymer can be considered in terms of Hildebrand solubility parameters (Appendix A). Figure 3.5 summarizes the optimum annealing conditions for each SD. There is a clear trend between the film thickness and the solubility parameter of the annealing selective solvent appropriate for each SD molecular weight. The optimum film thicknesses slightly exceed half respective structural periods for the first three SD samples, or roughly $3R_g$, where R_g stands for the radius of gyration of the respective block copolymer chains. In addition to the solvents listed in Figure 3.5 for each SD, other solvents with similar solubility parameters or mixed solvents (Table 3.2) are effective as well. There is at least a 30 minutes processing window where the defect-free morphology can be captured for each SD on a

PS substrate, which qualifies the method as well-defined and reliable. This guideline can be used as a powerful tool to predict suitable annealing conditions for SD with similar composition and different molecular weights. The two key elements of the method illustrated by Figure 3.5 are the sub-lattice film thickness and the selective annealing solvents with solubility parameters increasing with the SD molecular weight.

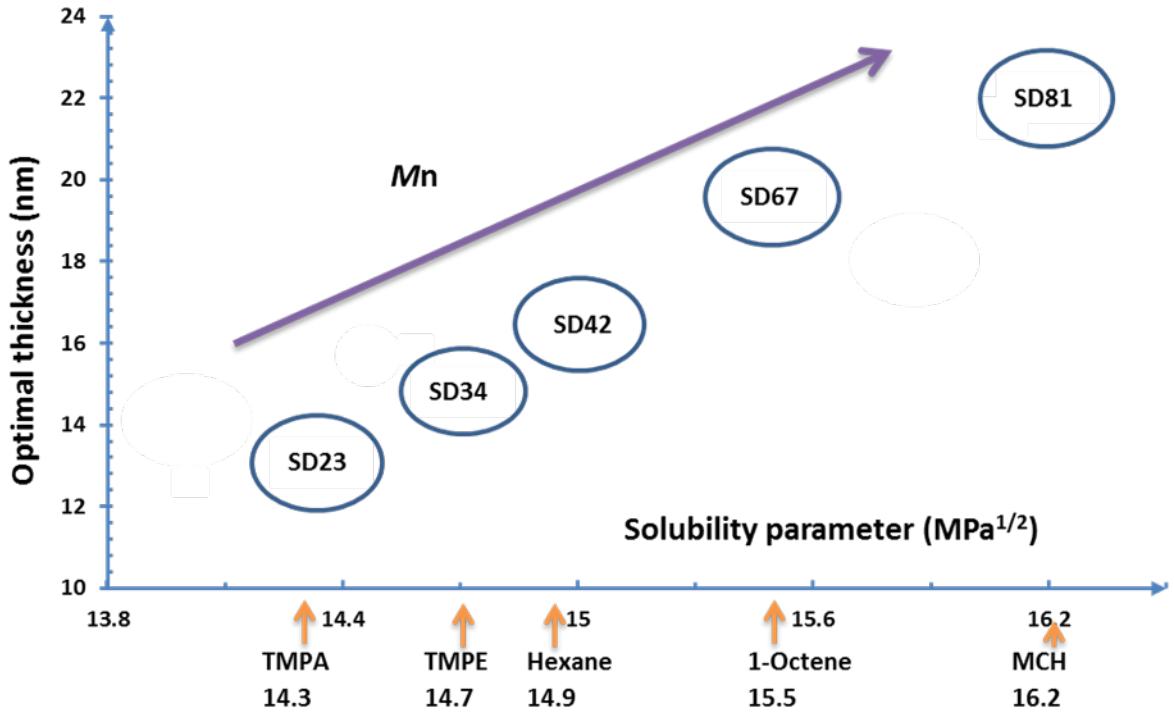

Figure 3.5. Processing window for the film thickness and annealing conditions. The optimum processing space ranges of film thicknesses and solvent solubility parameters shown by the bubbles do not have clean-cut boundaries. However, we experience readily induced defects when operating outside the shown optimum zones.

Table 3.2. Optimal annealing solvent for each BC

BC	Pure solvent	Mixed solvent*
SD23	TMPA, 2,2,3-Trimethylbutane	HM/To (20/1), HM/Xylene (10/1)
SD34	TMPE	HM/To (10/1), HM/Xylene (6/1)
SD42	Hexane, Heptane	HM/To (5/1)
SD67	1-Octene	Hexane/To (10/1)
SD81	MCH	

*ratio by volume.

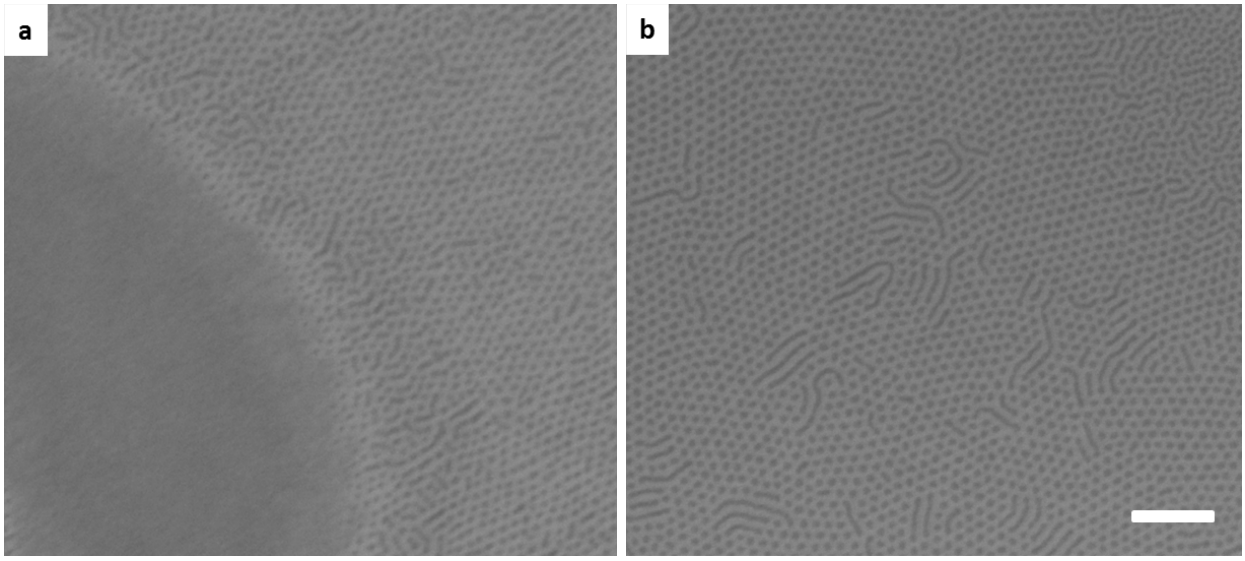

Figure 3.6. Top view SEM images of the SD42 annealed in hexane for 30 minutes with a thickness of (a) 13.2 nm and (b) 16.9 nm , Scale bar: 200 nm.

The film morphology is strongly dependent on the film thickness and the annealing solvent. For an example, as shown in Figure 3.6, when the film thickness is beyond the ideal range (14.5-16.5 nm), defects readily present. Similar results are also observed when the annealing solvent is changed, as shown in Figure 3.7, the transition of the horizontal cylinder to perpendicular cylinder is captured. By annealing under vapors of the slightly more selective solvent to PS block,

1-octene ($\Delta\delta_{PS\text{-}1\text{-}octene}$ = 3.0), instead of hexane ($\Delta\delta_{PS\text{-}hexane}$ = 3.6), the perpendicular cylinder phase seems to be the equilibrium state. The film is homogeneous and no sphere phase is observed for 4 hours (longer annealing time not tested). However, defects are always present in the film, as compared to the well-defined morphology kinetically trapped within the optimum window of the transition-state shown in the Figure 3.5.

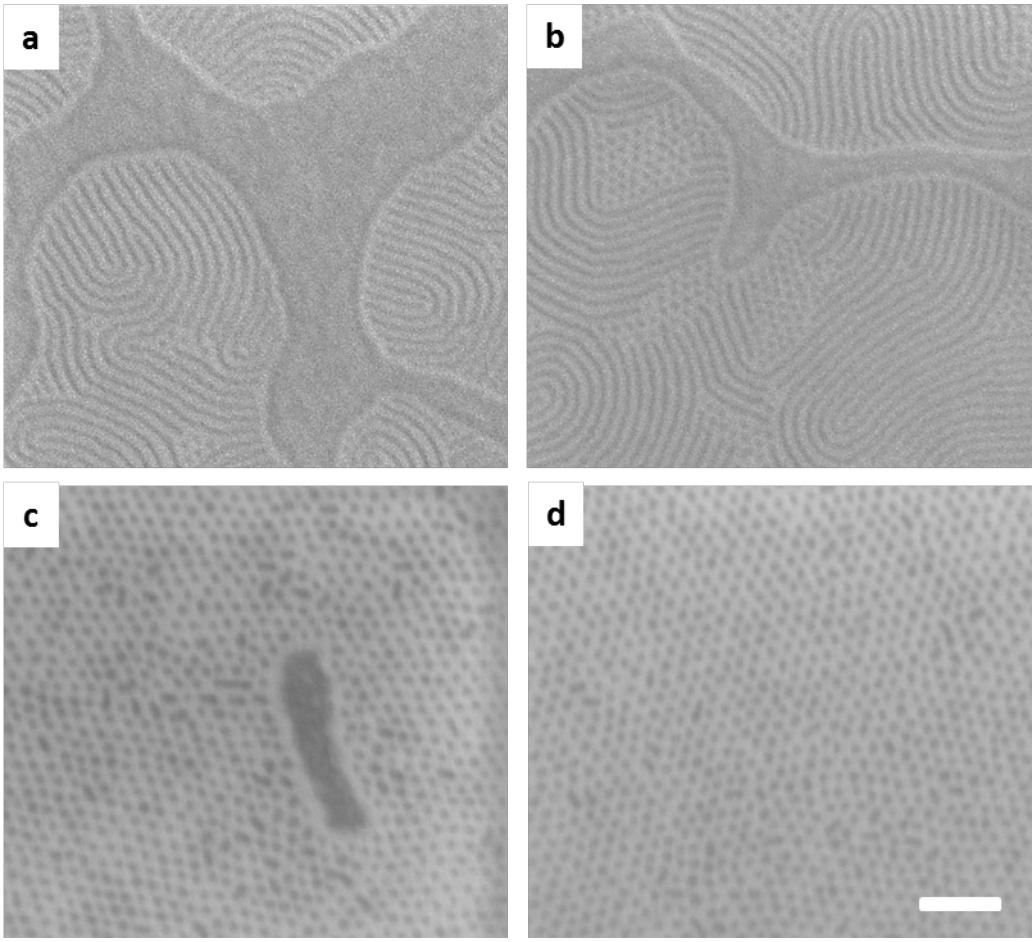

Figure 3.7. Top view SEM images of the SD42 annealed in 1-octene for (a) 15 minutes, (b) 30 minutes, (c) 1 hour and (d) 4 hours, Scale bar: 200 nm.

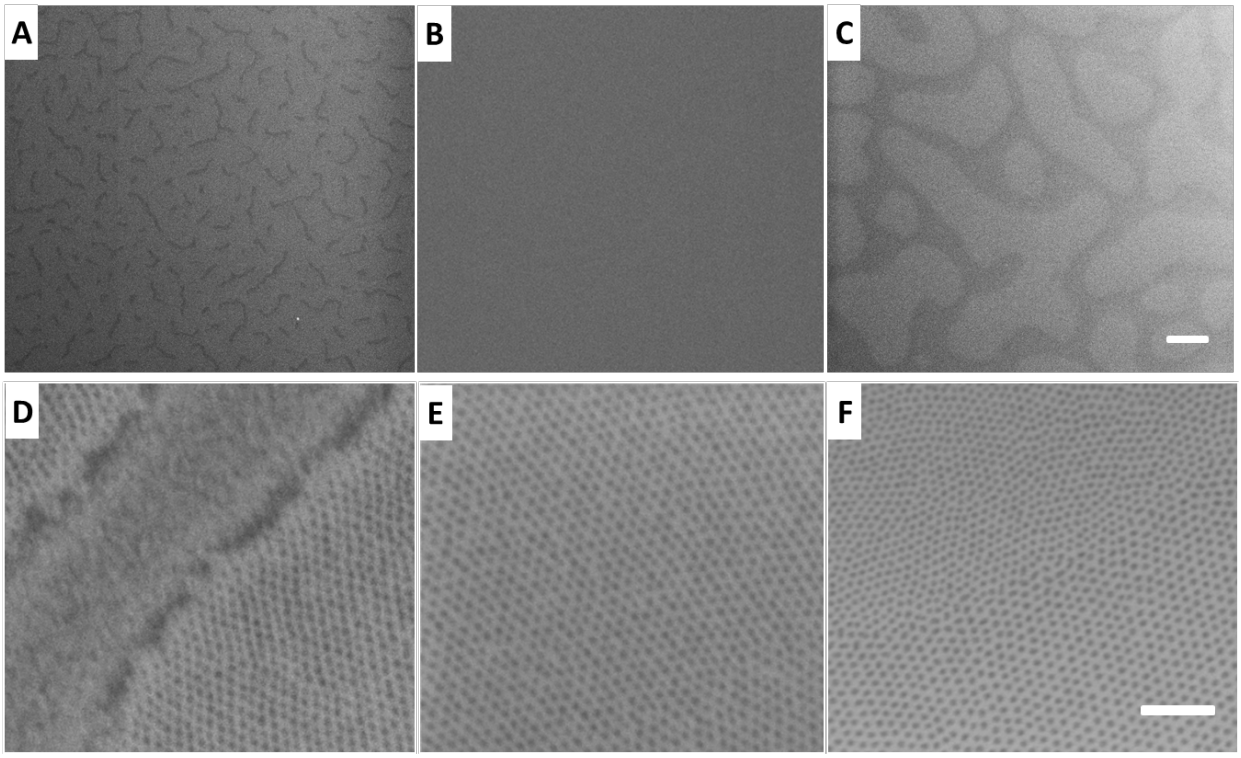

Figure 3.8 Images of the SD42 morphology evolution. Top view SEM images of SD42 annealing in hexane for (a) 15 minutes; (b) between 20 and 60 minutes; (c) 75 minutes. (d-f): magnified SEM images of a-c. Scale bars: 200 nm in the first row and 20 □m in the seco

The third key element, i.e. the kinetic control, can be illustrated by the morphology evolution of SD 42 shown in Figure 3.8 At the early stage (Figure 3.8a,d), the perpendicular cylinder phase gradually propagates to the initial disordered area. At annealing times between 20 and 60 minutes (Figure 3.8b,e), the whole film stays in the perpendicular cylinder morphology free of defects. At longer annealing time the morphology shifts to the spherical phase, which appears in the upper-left corner of Figure 3.8c with a smaller period. The sphere region blocks pattern transfer to the substrate due to the thicker PDMS wetting layer (next section). These observations support the formation of a cylindrical morphology within the annealing process window and the development of a spherical morphology at longer annealing times. The periodic undulation of the

annealed SD film observed in the topographic AFM image in Figure 3.4a,d is caused by the very unequal swelling of the PDMS ($\Delta\delta_{PDMS\text{-}hexane}$ = 0.1) and PS ($\Delta\delta_{PS\text{-}hexane}$ = 3.6) domains in the presence of vapor from the PDMS selective annealing solvent.

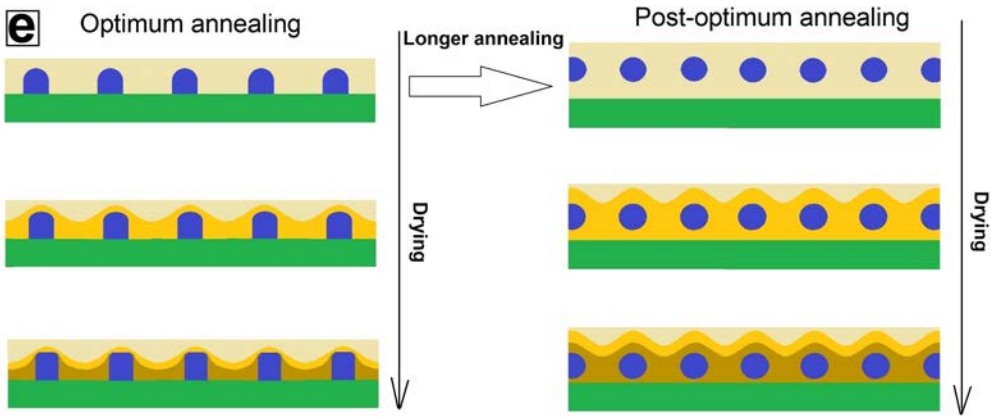

Figure 3.9 Schematics of the proposed mechanism for structure formation at and beyond the optimum annealing window. The darker yellow-brown color represents lower solvent content. Over the entire optimum annealing window the structure in the swollen state consists of hexagonally packed half-spherical or half-sphere capped cylindrical PS domains swollen by a factor of approx. 1.2 surrounded by PDMS coronae swollen by estimated factors of 1.5 – 1.7 (see below).

Fig. 3.9 illustrates a mechanistic model that is compatible with all the mentioned key observations: (a) the structure at the optimum processing window shows pronounced height modulation, with PS domains having little or no PDMS top layer; (b) the same structure does not show PDMS wetting layer beneath the PS domains; (c) the structure developing at post-optimum conditions shows a thicker PDMS wetting layer with a smaller period than the optimum structure. The dry optimum structure originates from half-spherical or half-spherical capped cylindrical

swollen morphology, which would rearrange in the drying stage into cylindrical morphology. The reshaping of the half-spherical / half-spherical capped micelles into cylindrical is driven by the presence of more solvent in the lateral space between PS domains meanwhile the drying front advances downwards. At this stage PS should still be in the rubbery state. This reshaping accounts for the absence or scarcity of PDMS on top of the PS dots as observed by the AFM modulus and adhesion modes in Figure 3.2, as well as by the relative ease of access of the PS domains either directly by oxygen plasma (see next section) or by a short SF_6 plasma treatment (see next section).

The vapor annealing process is monitored in situ by QCM measurements; the obtained swelling data support that (1) the SD samples are in the microphase segregated state during annealing, and (2) the PDMS domains are 2.5-3 times more swollen than the PS domains. The effective volume fraction of the PS block f_S in SD42 varies from 0.29 in the dry state to 0.24, 0.23, 0.22 after resp. 40, 60, 75 min of hexane vapor annealing time (see below). At f_S of approx. 0.22 – 0.24 self-consistent field calculations [(19)] predict cylinder to sphere order-to-order transition in the thin film regime. However, the model in ref. 19 assumes symmetrical interfacial potential and absence of solvent, which are both not satisfied by our system. The solid surface is preferential to PS and air is preferential to PDMS. Therefore the model is not expected to describe our system quantitatively. Indeed, the model predicts laying cylinders or hexagonally perforated lamellae as stable morphologies at $f_S = 0.24$ and film thickness $w = 3R_g$, similar to ours, R_g being the radius of gyration of an unperturbed SD macromolecule. Stable standing cylinder morphologies are predicted at film thicknesses below $2R_g$. These discrepancies could be clarified by more realistic, and complex, models of solvent vapor annealing process in the future.

In Figure 3.9, the upper surface of the fully swollen micelles has been purposefully drawn as undulated in order to visually accentuate the single micelles; in reality the swollen film is expected to be smoother. The darker yellow-brown color represents lower solvent content. Over the entire optimum annealing window the structure in the swollen state consists of hexagonally packed half-spherical or half-sphere capped cylindrical swollen PS domains* surrounded by 2.5-3 times more swollen PDMS coronae*. The SD films are expected to remain in the microphase segregated state during annealing**.

At post-optimum annealing times the half-spherical / cylindrical domains start to transform into spherical domains (micelle-like) with diminished lateral order. The average period of the spherical morphology is 0.6 – 0.8 of the period for the cylindrical morphology. In contrast to the cylindrical, the spherical morphology has a thicker PDMS top layer (see next section). At even longer annealing times the morphology becomes even more irregular due to possible merging of spheres into elongated shapes.

* The swelling ratio of a 10 nm PS 50k film measured by QCM under hexane vapors is 1.20 at 40 min, and 1.24 at 60 min & 75 min annealing times. Swelling ratios of this order are expected to bring the glass transition temperature of PS below room temperature [J. E. Mark editor, Physical Properties of Polymers Handbook, Springer, 2nd ed. 2007, chap. 12], therefore ensuring chain mobility for structure rearrangement. The corresponding swelling ratios for PDMS can be estimated by the measured swelling ratios of SD42 ($SR_{SD42@40'}$ = 1.46, $SR_{SD42@60'}$ = 1.56, $SR_{SD42@75'}$ = 1.61) and the swelling ratio of PS, obtaining: $SR_{PDMS@40'}$ = 1.57, $SR_{PDMS@60'}$ = 1.69, $SR_{PDMS@75'}$ = 1.76. The volume fraction of the PS block in SD42 varies from 0.29 in the dry state to 0.24, 0.23, 0.22 after resp. 40, 60, 75 min hexane vapor annealing time.

** All SD polymers are expected to remain in the microphase segregated state during swelling. Argument: the measured swelling ratio of SD42 up to 75' annealing under hexane vapors is 1.61. Therefore the effective χparameter at this swelling can be estimated by: $\chi_{eff} \approx \chi_{pol} \cdot \chi_{SD} = 0.62 \cdot 0.27 = 0.17$. For SD23 with lowest molecular weight, the total average degree of polymerization is $N = 289$. Therefore $\chi_{eff} N \geq 49$, which places all the swollen polymers safely in the microphase segregated state; the self-consistent order-to-disorder transition at a block volume composition of 0.8 : 0.2 is expected at$\chi N \sim 20$ [F. S. Bates and G. H. Fredrickson, Phys. Today, 1999, 52, 32–38].

3.3 Pattern transfer on polymer substrate

In this section, the pattern generated in last section is used the hard mask directly for polymer substrates etching without any substrate modification which is taken as a routine step in nearly all the similar work found in literatures.

Materials: All the solvents are purchased from Sigma Aldrich without further purification. PS (50k, synthesized in our lab), PMMA (70k, Diakon), PSF (27k, Scientific Polymers), PLA (M_w 18k-28k, Sigma Aldrich), PB (Scientific Polymers, *MW* 100k, crosslinking procedure:(*24*))

Fabrication: All the polymers are spin-coated on a silicon wafer using the condition summerized below:

Polymer	Dissolved in	Concentration (g/L)	RPM	Thickness
PS	Toluene	1	2000	52 nm
PMMA	Ethyl acetate	0.7	2000	57 nm
PLA	Chloroform	0.4	2000	65 nm
PSF	Ethyl acetate	0.8	2000	75 nm

PB	Chloroform	0.3	2000	92 nm

The mask is disoolved in heptane and directly spin-coated on top of the polymer substrates with the correponding thickness shown in last section.

The dry etch process is performed on an Advanced Silicon Etcher (STS MESC Multiplex ICP serial no. 30343). SF_6 plasma condition for pretreatment: 20 sccm SF_6, 20 mTorr, coil power: 50w and platen power: 0w, 5 – 10 seconds.O_2 plasma condition for the pattern transfer: 10 sccm O_2, 5 mTorr, coil power: 200w and platen power: 20w. SF_6 plasma condition for mask removal: 50 sccm SF_6, 20 mTorr, coil power: 200w and platen power: 2w, 20 seconds.

Characterization: Film thickness is determined by a VASE Ellipsometer (J.A. Woollam) at three different incidence angles (55^o, 60^o and 65^o). Scanning electron microscopy (SEM) images are taken by a Field Emission Zeiss Ultra Plus scanning electron microscope with a Gemini column operating at an accelerating voltage of 2kV. The cross-section is taken at a tilt angle of 45^o. All the samples are imaged directly without coating or staining. Atomic Force Microscopy (AFM) images are taken by an AFM Dimension Icon-PT from Bruker AXS.

Results and discussion: A number of common polymer substrates (PS, PMMA, PLA, PSF and cross-linked PB) are invetigated as the subtrates for pattern transfer by the mask developed in lat section. Heptane is a nonsolvent for these polymers, allowing direct spin-casting of the SD without any disturbance.

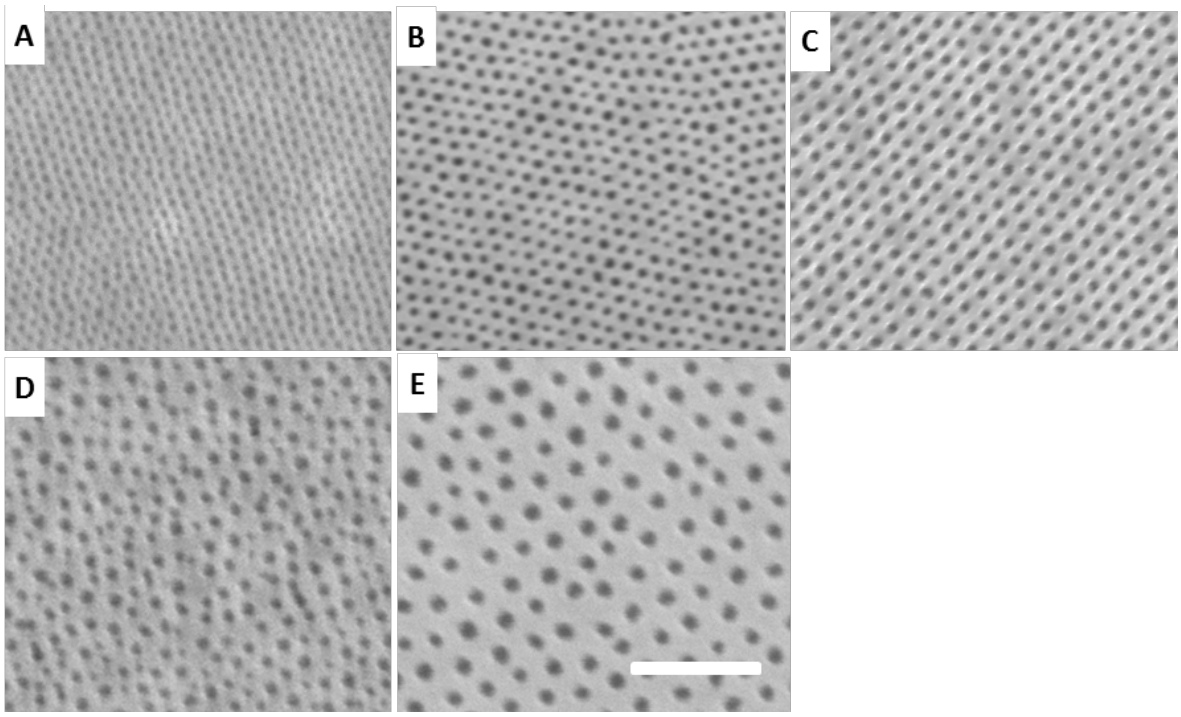

Figure. 3.10 Top view SEM image of the masks after pattern transfer onto PS substrate: (a) SD23 after O_2 plasma etching only, (b) SD34 after SF_6 and O_2 plasma etching, (c) SD42 after O_2 plasma etching only, (d) SD67 after SF_6 and O_2 plasma etching and (e) SD81 after SF_6 and O_2 plasma etching. O_2 RIE removes PS block, solidifies PDMS block and transfers pattern onto substrates. Scale bar: 200 nm.

Firstly, the mechanism is illustrated using PS as the substrate. The pattern transfer is conducted by RIE (Figure 3.10a,b,c,d,e). In most cases, a short SF_6 RIE is firstly used to remove a thin layer of residual PDMS on top. Compared to Figure 3.2, the improved SEM image contrast after etching suggests the successful pattern transfer, which is further evidenced by AFM image in Figure 3.12 and the cross-section image of the samples after etching (Figure 3.13).

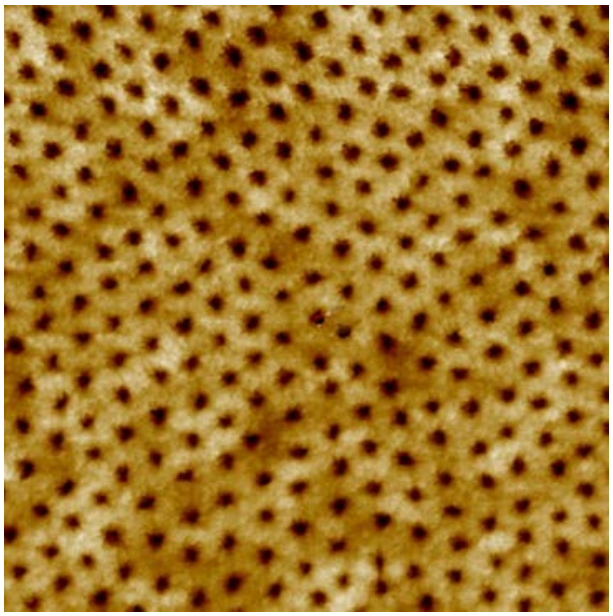

Figure 3.12. AFM image of the SD42 annealed in hexane for 40 minutes on PS substrate and treated with O_2 RIE; size: 500nm x 500nm.

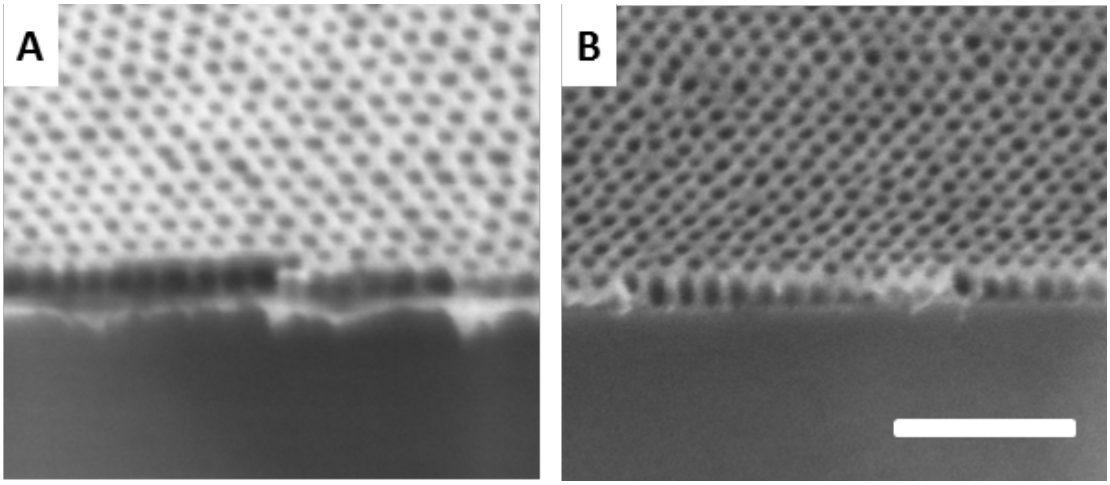

Figure 3.13 Cross-section of the SEM images of SD42 mask (a) after etching and (b) after mask removal. All the samples are spun-cast on the PS (50K) substrate (coated on the silicon wafer with a thickness around 50nm). Scale bar: 200nm.

The mask can be readily removed by a SF_6 RIE (confirmed by the absence of Si element in X-ray photoelectron spectroscopy measurement) without damage to polymer substrate (Figure 3.13b). Figure 3.13 indicates a nicely patern transfer process by this method.

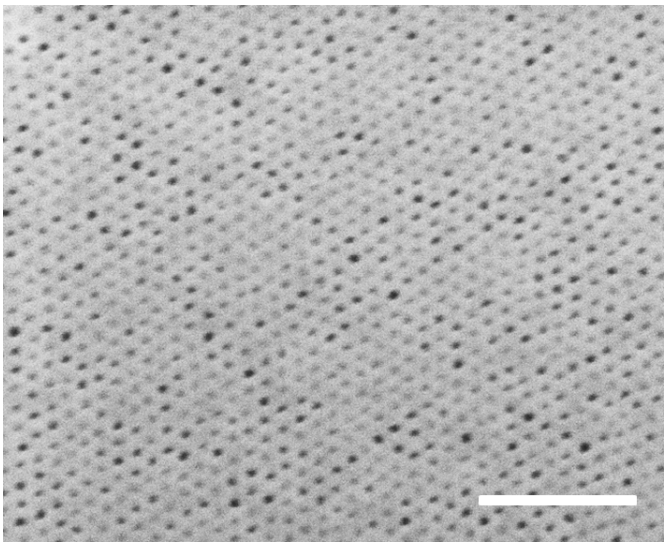

Figure 3.14. SEM image of the SD23 on PS substrate after O_2 RIE. Scale bar: 200nm

Figure 3.14 shows the SD23 only treated with O_2 RIE and most of the pores stay clogged. However, in some cases (Summerized in Table 3.3), only an O_2 RIE is sufficient to complete the pattern transfer (Figure 3.11a,c). In these cases the film is free of a PDMS top wetting layer after solvent vapor annealing, which is difficult to obtain for PDMS-containing BC. The mask produced has high etching resistance under oxygen plasma and high thermal stability (Figure 3.15).

Table 3.3. Condition for SD film free of PDMS top-wetting layer. Only oxygen is needed to transfer the pattern. However to ensure that all the pores are open, we still recommend a short initial fluorine plasma treatment. (HM: Hexamethyldisiloxane and To: Toluene).

BCP	Substrate	Film thickness nm	Annealing solvent*	Anneal time
SD23	PS	13.5	HM/To (20/1)	1 hour
SD42	PS	16.2	Hexane	40 minutes

* Ratio by volume in the liquid phase.

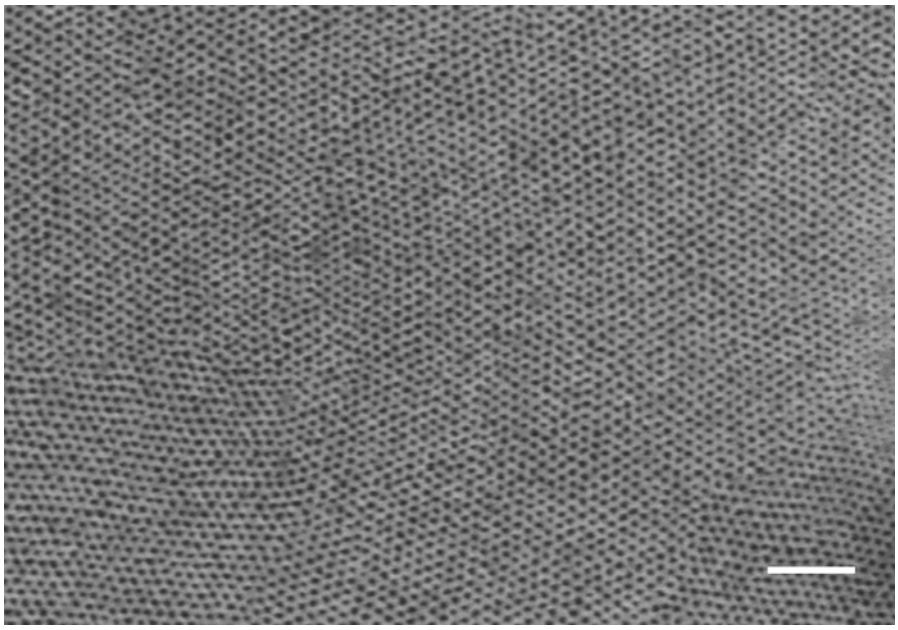

Figure 3.15. SEM image of the SD34 mask after pattern transfer and thermal treatment at 450^{o}C for 2 hours under N_2 flow. Scale bar: 200 nm.

Figure 3.16 shows the attempts of pattern transfer on the films with defects in mask. It is clear that the area with defects is unable to transfer the pattern. This can be explained by its spherical morphology with thicker top-wetting layer and the lower wetting layer of PDMS at the interface with substrate.

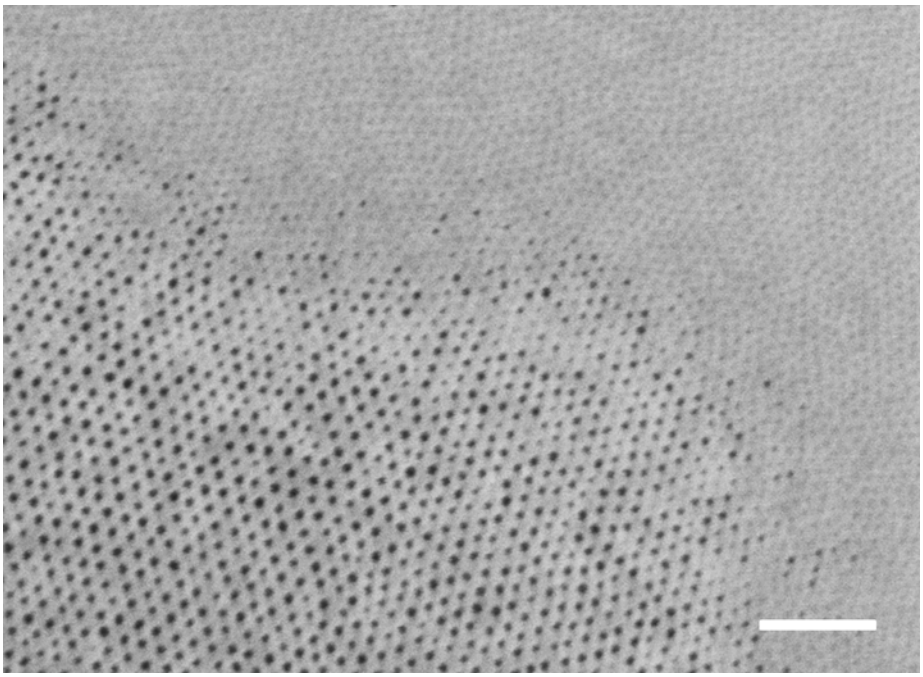

Figure 3.16. SD34 annealed in TMPE for 60 minutes (post-optimum annealing time) then treated with SF_6 and O_2 RIE. Scale bar: 200 nm.

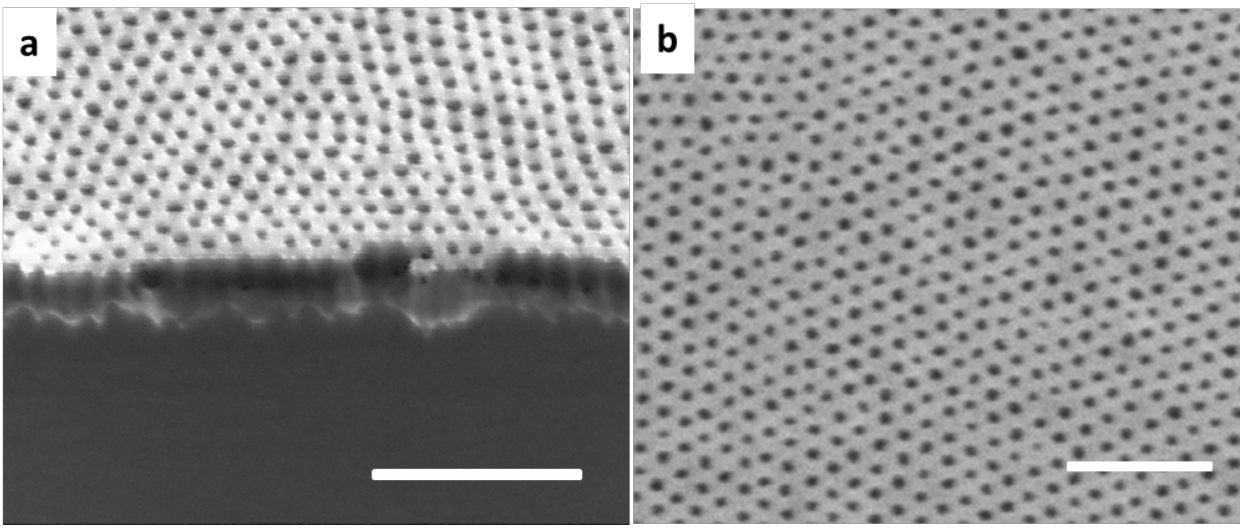

Figure 3.17. SEM images of pattern transfer to polysulfone, graphene and silicon. (a) Cross-section and (b) top view of polysulfone patterned by SD34, Scale bar: 200 nm.

Except PS substrate, the presented approach also shows strong substrate independence, as demonstrated in Figure 3.17 and Figure 3.18. The observed self-assembly behavior is similar to the already discussed behavior on PS substrate for all the tested substrates: PLA, PMMA, PSF, PB, monolayer graohene on Si, InP, and Si with native oxide layer. The compatibility of BCP with subtracted can be measured by water contact angle summarized in Table .3.4. The timing of the morphology evolution is somewhat different in each case but generally faster than the already discussed PS substrate. The pattern transfer is proved successful for all the substrates. Figure 3.17 shows the cross-section of polysulfone patterned by the SD34 mask; a well-ordered nano-pore channel array is clearly observed. Polysulfone is a technologically relevant material for ultrafiltration membranes due to its high thermal, mechanical and chemical resistance.(*25*) For membrane bio-analysis and separation, challenges still exist as to produce reliable membranes with anti-fouling properties, high flux and narrow pore distribution. After oxygen plasma etching, the iso-porous PSF membrane becomes hydrophilic (water contact angle: 19^{o}), which may significantly improve its anti-fouling properties.(*26, 27*) The demonstrated pattern transfer could offer an ideal solution to manufacture high performance thin polymer membranes.

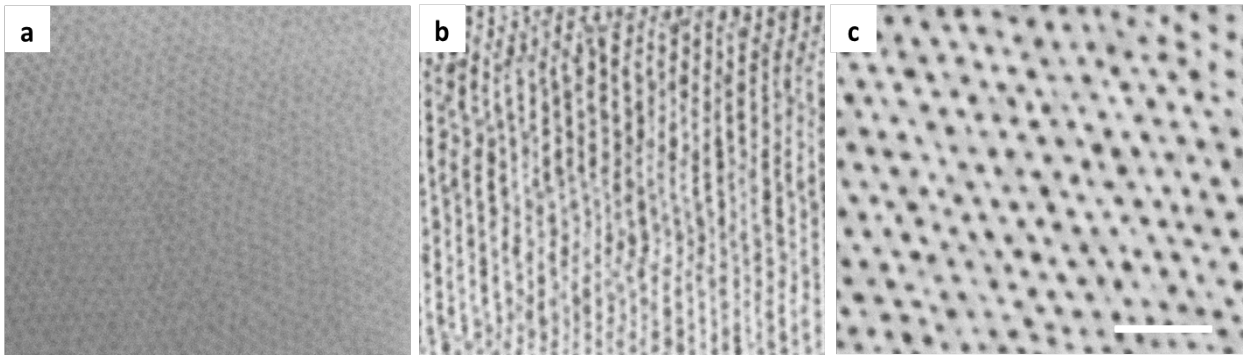

Figure 3.18. SEM image of a) the SD23 on PLA after annealing, b) SD23 on PMMA after etching, and c) SD42 on PB after etching. Scale bar: 200 nm.

Table 3.4. Water contact angle measurement

Sample	Angle measured
Si (with native SiO2 layer)	30
Al_2O_3 by ALD	60
PMMA	65.5
PLA	67
Graphene	69
PSF	73.5
HMDS modified Silicon wafer	80
PS	87
x-linked PB	91
PSF with mask after dry etch	19

Notice from Table 3.4 that with the exception of cross-linked PB the contact angle does not exceed that of PS. Remembering that the water contact angle of PDMS is ~ 108^0, one can argue that the PS block should show preferential wetting to the substrates as compared to the PDMS block.

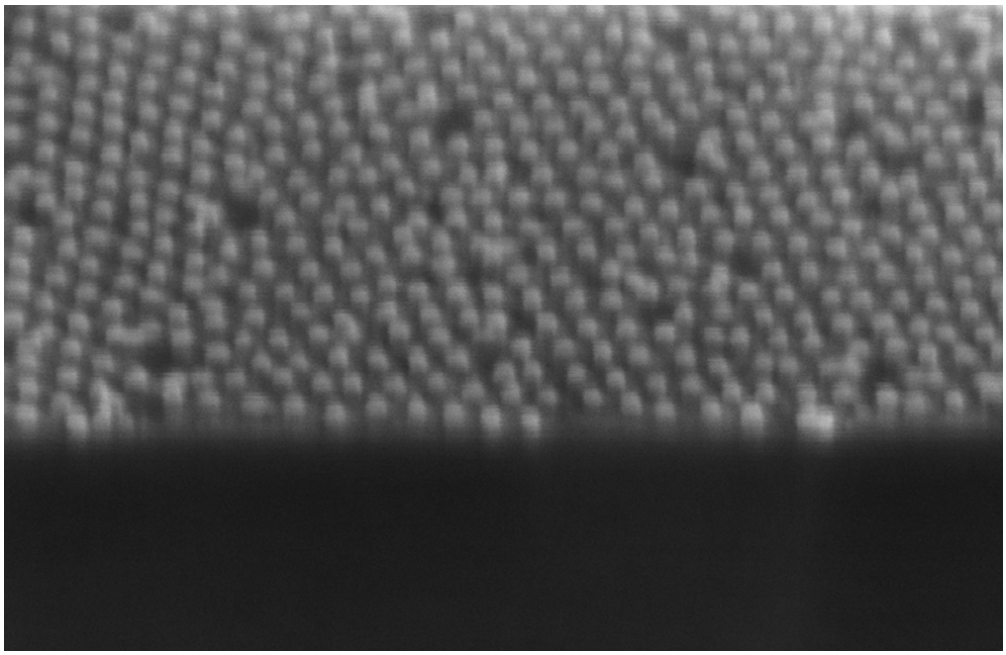

Figure 3.19 Cross-sectional SEM image of the SD12 mask on silicon treated with HF (40%) for 30 minutes

Except the dry etch, we also find HF solution can effectively remove the PDMS block, leaving the PS nano-pillars arrays.

3.4 Graphene nanomesh fabrication

Introduction: Graphene research has grown rapidly in scientific society due to its extraordinary electro properties of the 2D materials. (*28-31*) However, due to its insufficient band gap,(*32*) the applicability of graphene in many electronic applications is currently limited, despite its excellent charge transport properties. One way to open up the band gap is to employ the quantum confinement effects. For an example, by electron beam lithography, the so called “graphene nanoribbon” shows a band gap as semiconductors. (*33, 34*) However, sub-10 nm regime for the width of the nanoribbon is required achieves sufficient band bap for room temperature transistor operation according to the scaling law. To overcome that, a new nanostructured graphene derivative, so called “graphene nanomesh” where a high–density array of nanoscale-holes is punched, is created. (*35-41*)

Until now, several fabrication methods has been developed to manufacture high quality graphene nanomesh, such as electron beam lithography, self-assembled monolayers of colloidal microspheres, photo-catalytic pattern(*42*) and block copolymer lithography. First, the electron beam lithography suffers from the low throughput production, making it less attractive. The intrinsic length scale limit makes nano sphere incapable for ultra-small structure on graphene. The randomness pattern of the nanoparticles local catalysis is also undesired. So the block

copolymer lithography is the ideal technique for making large-area, high quality graphene nanomesh.

However, the BCP lithography for making graphene nanomesh so far is a tedious process involving multiple depositions and etching steps. Figure 3.20 shows a typical process flow of such a process. Most of all, it is difficult to reach sub-30 nm periods with the low-□/PS-PMMA mask used in most reports.

In this section, the method developed in this chapter is also particularly suitable for Graphene nanomesh fabrication. Here, SD is directly deposited on CVD-grown single layer graphene and the pattern transfer process is given.

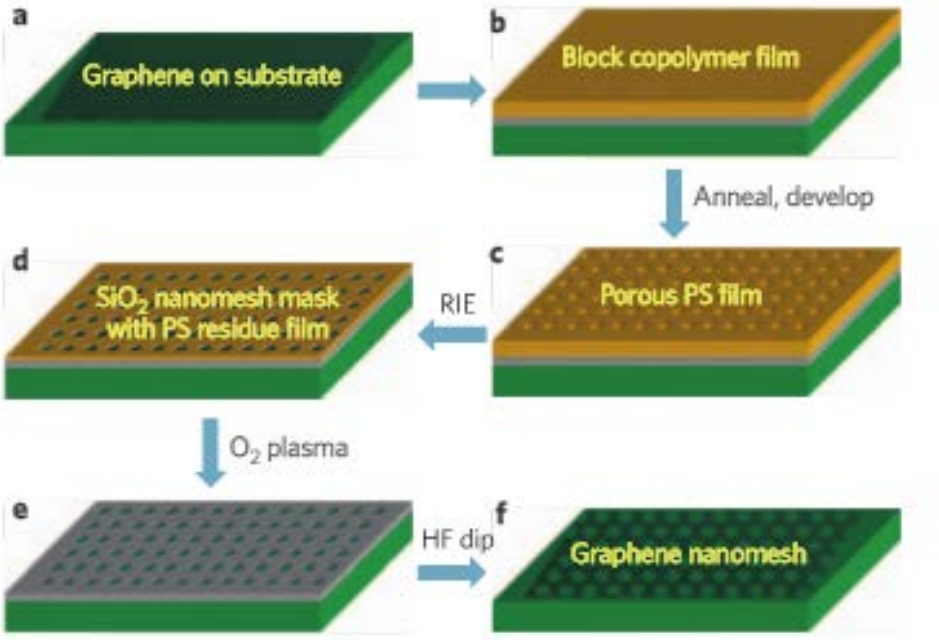

Figure 3.20. Schematic of fabrication of a graphene nanomesh. **a**, Pristine graphene flake on top of a silicon oxide substrate, forming the starting material. **b**, The graphene flake is covered by a

thin layer of evaporated SiO_x and a thin film of spin-coated block-copolymer P(S-*b*-MMA). The SiO_x is used as a protecting layer and grafting substrate for the subsequent block-copolymer nanopatterning process. **c**, The P(S-*b*-MMA) block-copolymer film is annealed and developed, leaving the porous PS matrix as the nanomesh template for further patterning. **d**, Fluoride-based reactive ion etching (RIE) to penetrate the oxide layer, partially degrade the PS film, and form the SiO_x nanomesh hard mask. **e**, Graphene in the exposed area is etched away by O_2 plasma. **f**, Following an HF dip to remove the oxide mask, a GNM is obtained.**g**, Free-standing GNM can be lifted off the substrate by etching away the underlying silicon oxide. (*35*)

Materials: All the solvents are purchased from Sigma Aldrich without further purification. Monolayer Graphene on SiO_2/Si (Graphenea) are used as received.

Fabrication: The mask is disoolved in heptane and directly spin-coated on top of the graphene substrates with the correponding thickness shown in section 3.2.

The dry etch process is performed on an Advanced Silicon Etcher (STS MESC Multiplex ICP serial no. 30343). SF_6 plasma condition for pretreatment: 20 sccm SF_6, 20 mTorr, coil power: 50w and platen power: 0w, 5 – 10 seconds.O_2 plasma condition for the pattern transfer: 10 sccm O_2, 5 mTorr, coil power: 200w and platen power: 20w.

Characterization: Scanning electron microscopy (SEM) images are taken by a Field Emission Zeiss Ultra Plus scanning electron microscope with a Gemini column operating at an accelerating voltage of 2kV. All the samples are imaged directly without coating or staining. A

Thermo DXR-Raman system with a laser wavelength of 455 nm is used for the characterization of graphene samples. The resolution is 5.9 – 8.5 cm^{-1}, spot size is 0.5 μm, collect exposure time is 10 s per scan, and 8 scans are accumulated for each sample.

Results and discussion:

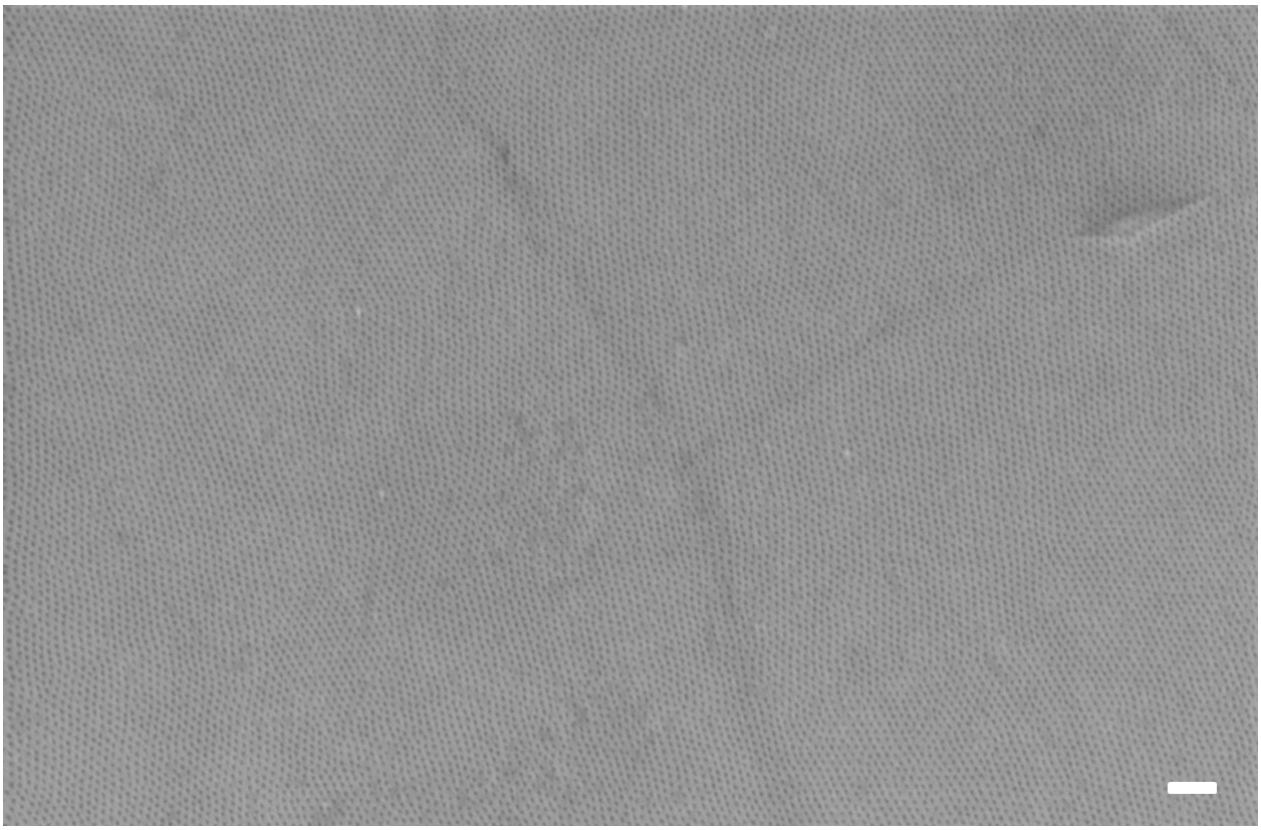

Figure 3.21 SEM image of the SD42 directly cast on graphene substrate, and annealed in hexane for 10 minutes. Scale bar: 200nm.

Figure 3.21 shows large-area mask covering graphene without defects after solvent annealing. The pattern is well adjusted on grain boundaries, multi-layer islands and substrate defects.

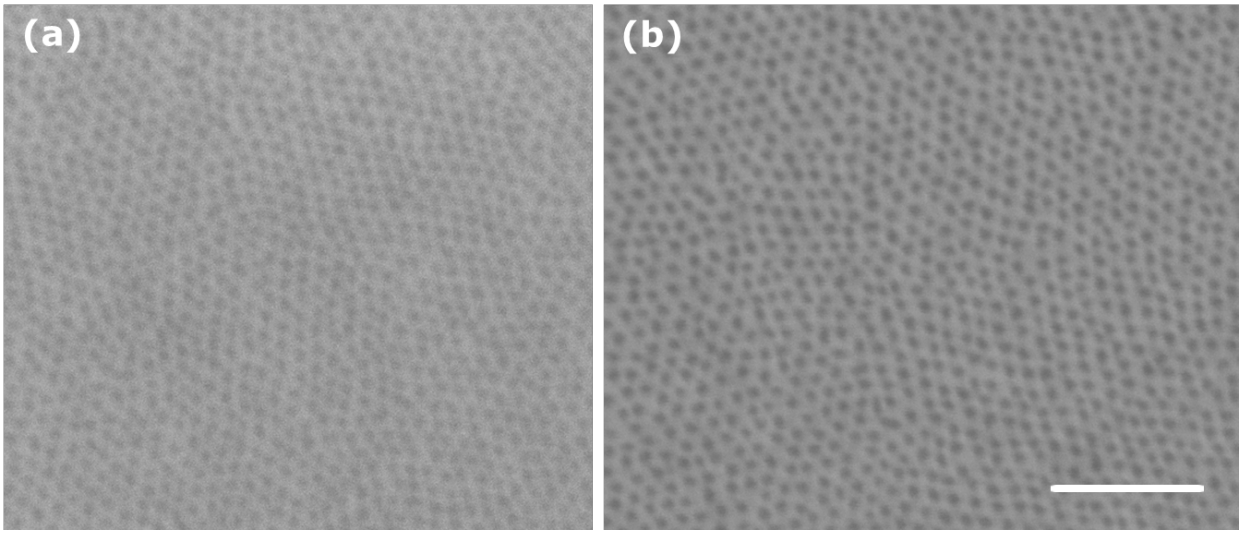

Figure 3.22 Tope-view SEM images of SD23 on graphene after (a) solvent annealing and (b) after O_2 RIE. Scale bar: 200 nm,

Other masks work similarly as well. The increased contrast in Figure 3.22b, as compared to Figure 3.22a, indicates effective pattern transfer.

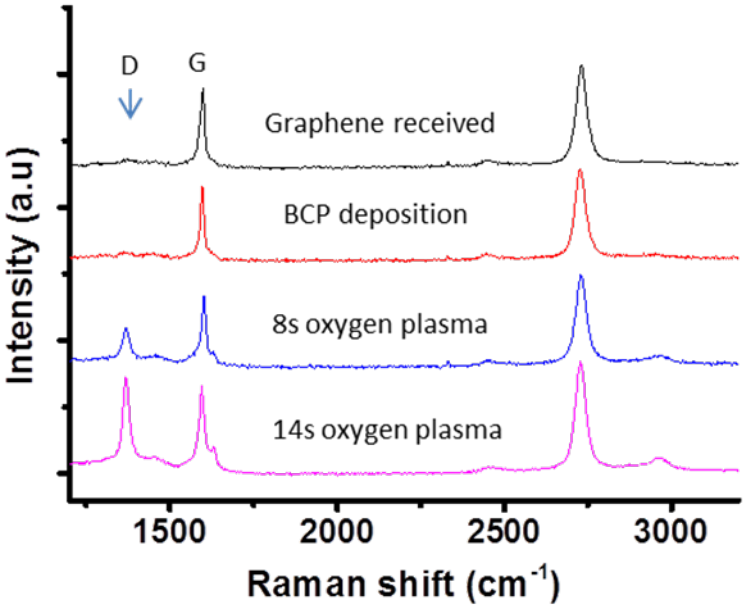

Figure. 3.23 Raman spectrum characterization of graphene patterning in the presence of the mask from SD42.

We use Raman spectroscopy to analyze the hole punching process, as shown in Figure 3.23. After the BC deposition, the spectrum stays the same. Increase in oxygen plasma etching time results in the increase of D peak, which typically characterizes the hole enlarging process. The excellent process control is evidenced by the unchanged width of the G peak.

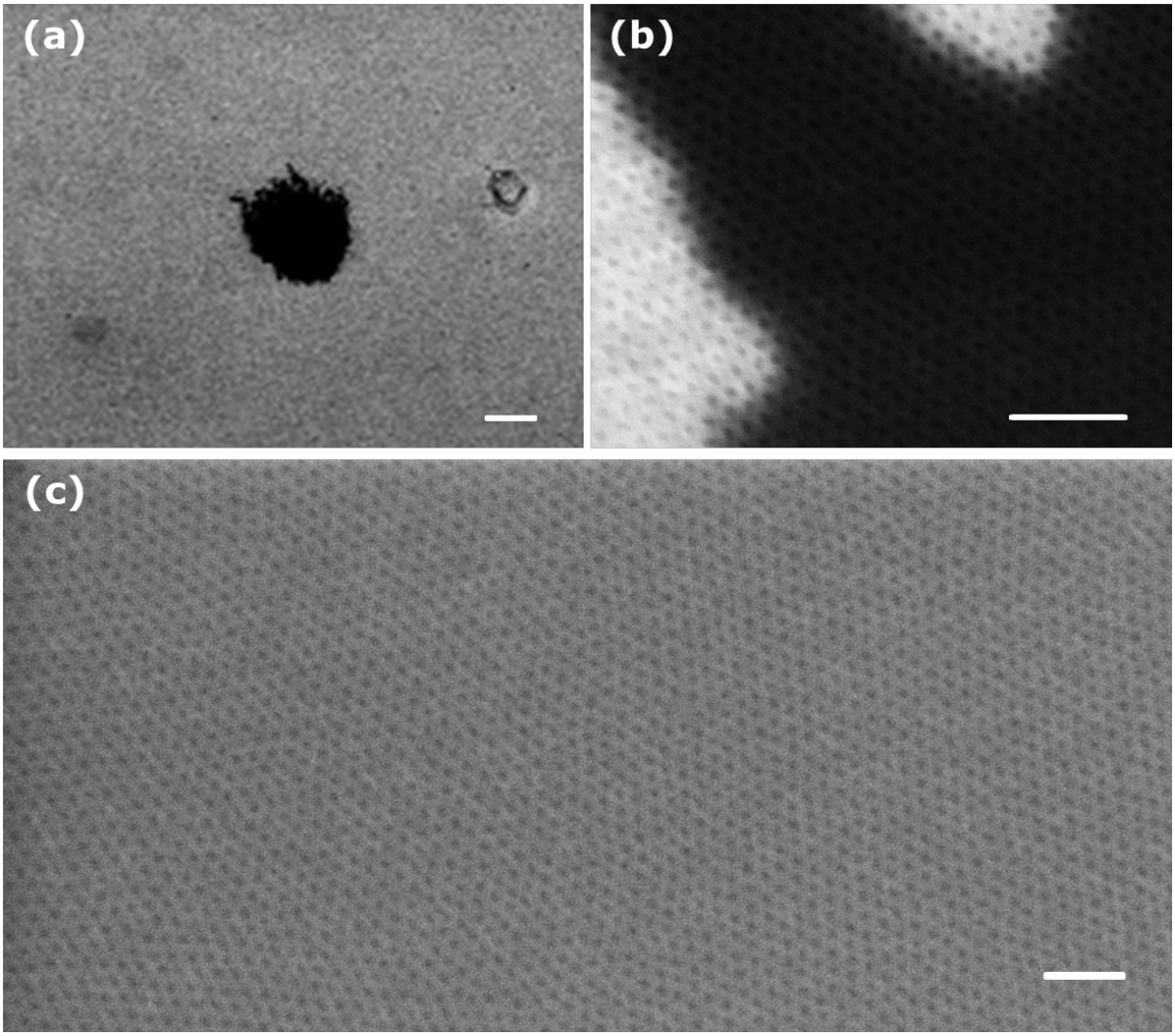

Figure 3.24 Top-view SEM image of (a) mask removed by tape in the black area, scale bar: 20 um, b) enlarged area of (a) and c) SEM image of top-view of the patterned graphene nanomesh by SD42. Scale bar: 200nm.

Figure 3.24 shows the patterned graphene after removing part of the mask by scotch tape. Nevertheless, the mask of only a small portion of the whole area is removed effectively by the tape. The distinct contrast between the areas with and without mask indicates full removal of the mask. This is further supported by the homogeneous Raman spectroscopy measurement. Besides, the black area where there is no mask shows the color as the monolayer graphene under the optic microscopy. In the area without mask (Figure 3.24c), the image shows a high fidelity reproduction of the mask morphology. The obtained graphene nanomesh has potentially many important applications, including fabrication of field-effect transistors,(*43*) gas sensors,(*44*) and atomic-layer separation membranes.(*45*)

Other attempts of removing mask are conducted as well with less satisfactory results. For an example, HF (40%) is used to remove the oxidized PDMS mask. However, since the graphene is put onto the silica substrate, everything above the silicon rapidly disappears in this wet etching. A proper solution is to use the graphene on top of the silicon substrate directly. Another method is to apply additional layer of PS or PMMA, then the mask is removed by fluorine plasma. First an organic solution rinsing is performed to dissolve PS or PMMA. However, the plasma process readily cross-links the polymer that the PS or PMMA can't be washed away anymore. Since graphene also shows higher thermal stability than common polymers. After pattern transfer, the sample is put into an oven at 400^{o}C to degrade the polymers. Even most of the polymers are gone, a carbon peak in XPS is always detected using a reference sample. This indicates that a thermal oxidation process is not enough to remove the polymers after O_2 RIE.

3.5 Silicon patterning

In this section, we are showing that the oxidized PDMS masks can be used not only for patterning carbonaceous materials by oxygen RIE; they also show higher resistance over silicon under chlorine RIE.

Fabrication: The mask with the correponding thickness shown in section 3.2 is disoolved in heptane and directly spin-coated on top of the silicon substrates with a native oxide layer.

The dry etch process for mask pattern geeration is performed on ASE. SF_6 plasma condition for pretreatment: 20 sccm SF_6, 20 mTorr, coil power: 50w and platen power: 0w, 5 – 10 seconds.O_2 plasma condition for the pattern transfer: 10 sccm O_2, 5 mTorr, coil power: 200w and platen power: 20w.

The silicon etching by chlorine RIE is performed on ICP Metal etch (SPTS Serial number MP0637). Breakthrough step: 20 sccm SF_6, 3 mTorr, coil power: 100w and platen power: 10w, 30 seconds. Cl_2 etching: 20 sccm Cl_2, 3 mTorr, coil power: 400w and platen power: 40w, 90 seconds.

The silicon etching by fluorine RIE is performed on ASE. Etching step: 10 sccm SF_6, 5 mTorr, coil power: 100w and platen power: 5w, 20 seconds.

The silicon etching by a pseudo-Bosch process is performed on ICP Metal etch (SPTS Serial number MP0637). Recipe: 38sccm SF_6 and 70sccm C_4F_8, 14 mTorr, coil power: 200w and platen power: 20w, time range from 30 seconds to 2 minutes.

Characterization: Scanning electron microscopy (SEM) images are taken by a Field Emission Zeiss Ultra Plus scanning electron microscope with a Gemini column operating at an accelerating voltage of 2kV. All the samples are imaged directly without coating or staining. XPS measurement is performed on a XPS-ThermoScientific instrument.

Results and discussion: Firstly fluorine based RIE is used to transfer pattern onto the silicon substrates. Pattern transfer at this small length scale is very delicate. As shown in Figure 3.25a,b, when the platen power is 10w, it is very difficult to achieve a decent pattern transfer. The defects readily present already before the complete destruction with increased etching time. This situation changes when the platen power is reduced to 5w, significant better pattern transfer is observed in Figure 3.25c,d. However, compared to the original mask, the diameter of the transferred hole pattern is also enlarged, which is due to the undercutting effect of the isotropic characteristic of silicon etching by fluorine based plasma. Besides, the depth of the transferred pattern is quite shallow. The selectivity of the mask to the substrate under this condition is estimated to be around one, which suggests the oxidized PDMS is a poor mask using SF_6 RIE. A pseudo-Bosch recipe is also tested, in which C_4F_8 gas is introduced as the passivation step to prevent the undercutting in silicon etching. This recipe is deliberately design for nanostructured silicon etching with small length scale, such as using deep-UV lithograph process. However, the

results are even worse. This suggest that silicon etching at very small length scale is quite changeling.

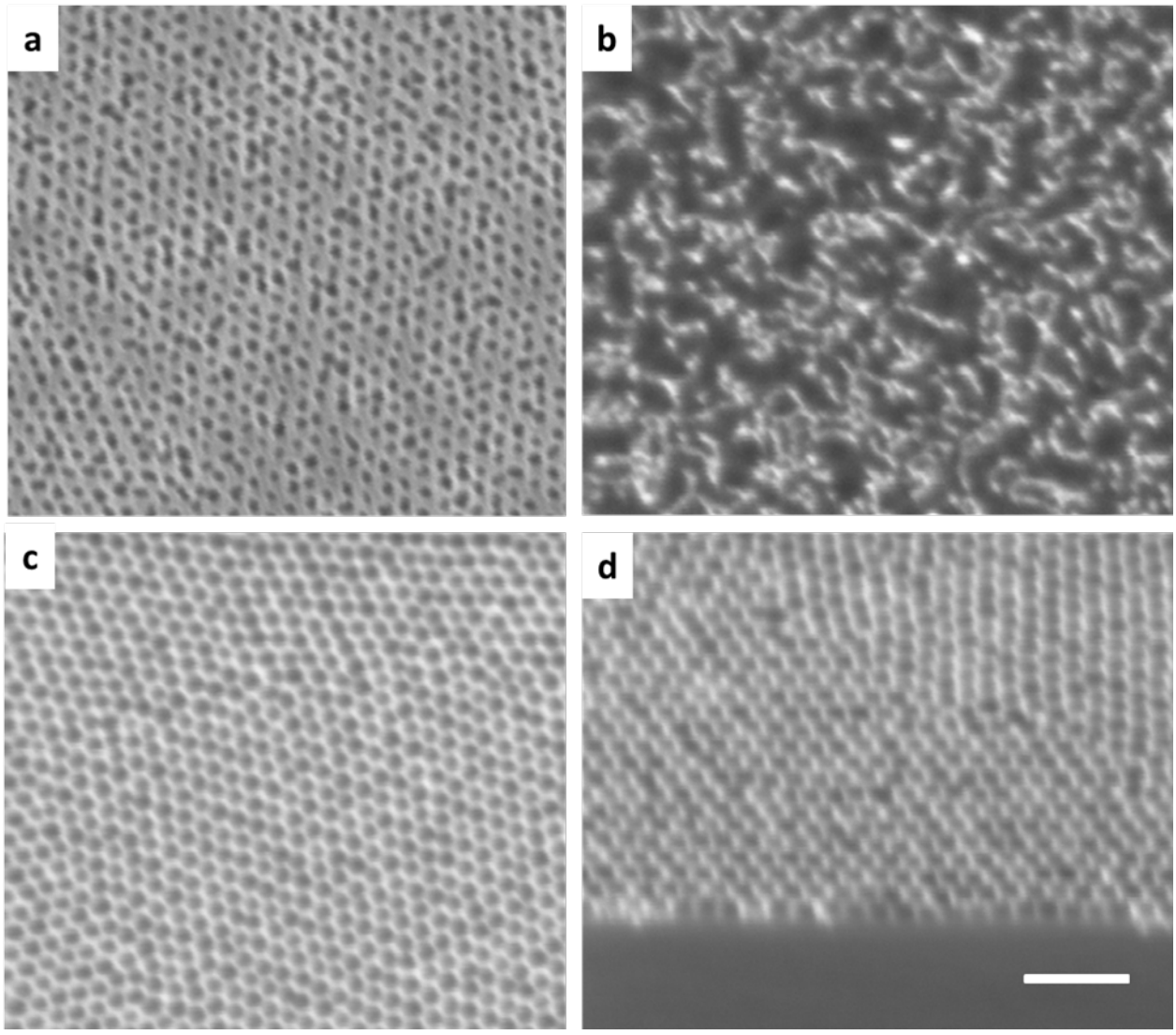

Figure 3.25. Top-view SEM image of silicon patterned by SD42 mask using SF_6 RIE for (a) 10 seconds with platen power of 10w, b) 13 seconds with platen power of 10w and (c) 24 seconds with platen power of 5w and (d) cross-sectional SEM image of (c). Scale bar: 200nm.

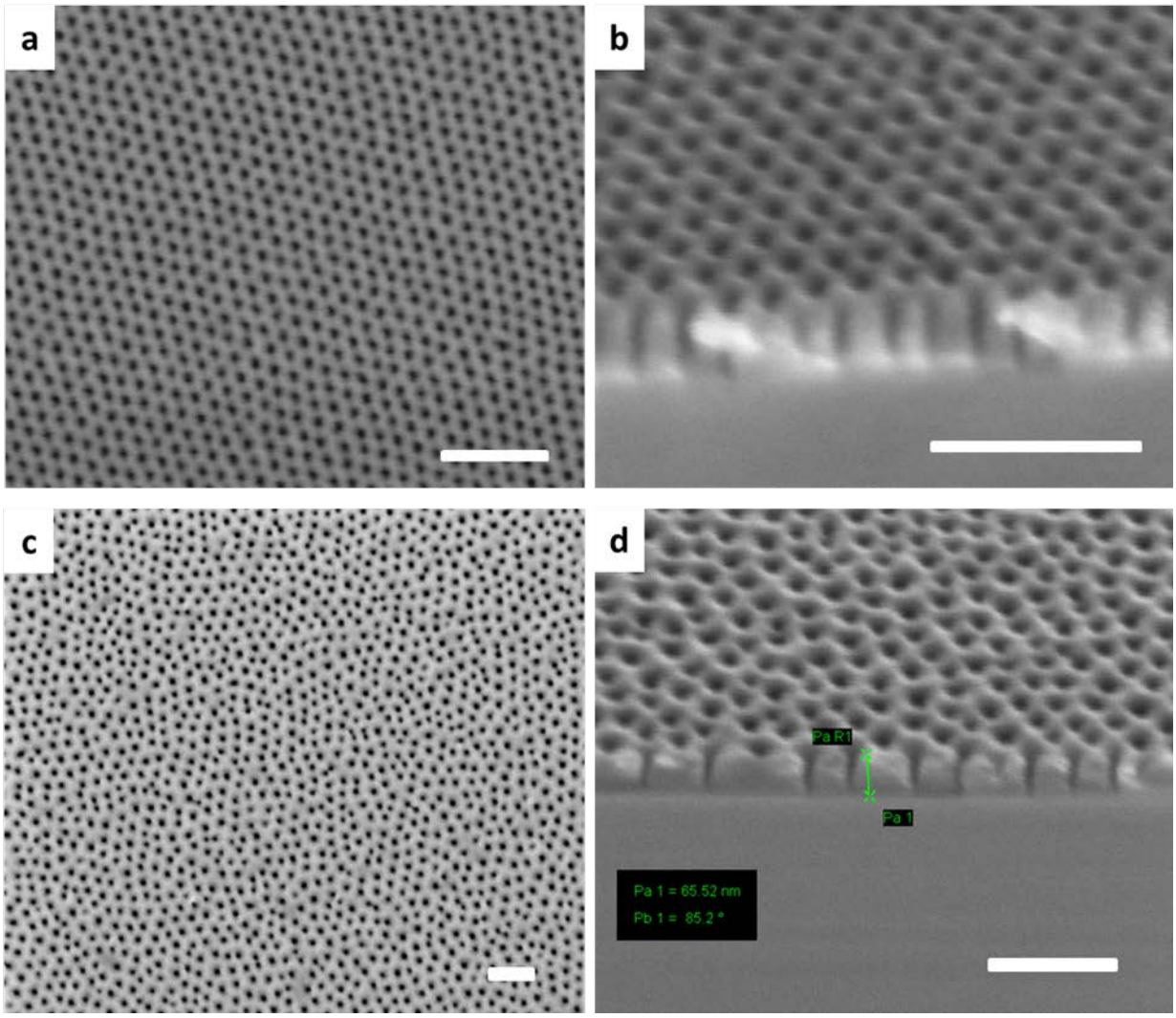

Figure 3.26. SEM image of a) top-view and b) cross-section of the silicon patterned by chlorine RIE using SD42 mask. Holes with aspect ratio exceeding 4 are clearly visible in b). c) top-view and d) cross-section of the silicon patterned by chlorine RIE using SD81 mask. Scale bar: 200nm.

On the other hand, as shown by the SEM images in Figure 3.26, unlike the isotropic fluorine plasma etching, where the pore-broadening is significant, the silicon etching by chlorine plasma is highly anisotropic.(*46*) Therefore, regular arrays of high-aspect-ratio holes in silicon are obtained by direct application of chlorine plasma to the oxidized PDMS mask. The selectivity of the mask to the substrate under this condition is estimated to be around 7, which is significantly

higher than fluorine based plasma. Similarly, hole-arrays of silicon with bigger feature size is fabricated by SD81 mask (Figure 3.26c,d). This process can be applied to pattern silicon with other morphologies, such as lines and dots by PDMS-based BC masks, which is of great relevance for semiconductor industry and solid-state nanopores materials. (*47*)

One thing need to be mentioned is that a breakthrough step is need before the chlorine RIE. Failure to do that will result in complete erase of the pattern. This can be explained that the native oxide layer has stronger resistance towards to chlorine RIE than the oxidized PDMS mask. This breakthrough will remove approximately 1.3 nm silicon dioxide which is corresponding to the thickness of the native oxide layer. Insufficient etching of this layer readily results in insufficient pattern transfer, as shown in Figure 3.27.

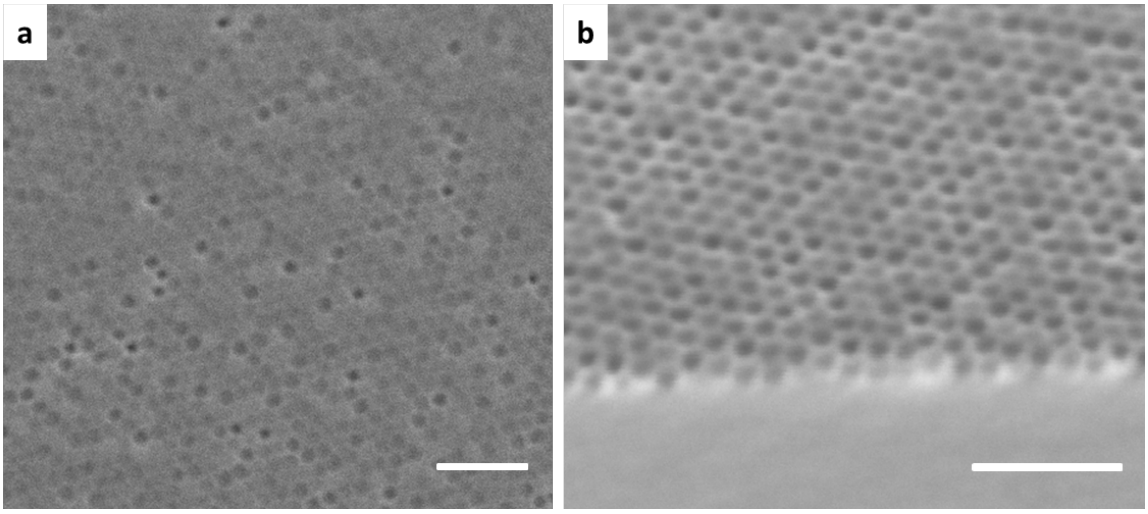

Figure 3.27. SEM image of a) top-view and b) cross-section of the silicon patterned by chlorine RIE using SD42 mask with 25 seconds of breakthrough step. Scale bar: 200nm.

3.6 Concluding remarks

To sum up, we have demonstrated a noval BCP nanolithography process using several cylindrical PDMS-rich PS-PDMS BCPs with perpendicular orientation by selective solvent vapor annealing. The highly ordered morphology is captured via kinetic control of BCP assembly and fast solvent evaporation. The BCP mask can be directly applied on various substrates without brush layer or top coats, which greatly simplifies the lithography process. During the shift of cylinder to sphere phase induced by selective solvent, the perpendicular orientation is kinetically trapped. The choice of solvent, film thickness and annealing time play a pivotal role in determining the final structure. A general guideline for PDMS-rich PS-PDMS with different molecular weights and compositions is given and it may offer a powerful conceptual approach for other BCP systems. As results, removal of PS domain, hardening of PDMS domain and pattern transfer can be achieved simultaneously in a simple dry etch process. Pattern transfer is successfully demonstrated on many substrates including common polymers, silicon and graphene. This facile and versatile method provides unprecedented opportunities to make iso-porous membrane (*47*) and hole arrays on 2D materials, opening up numerous applications like thin film patterning (*48*), membrane separation, nanostructured materials, sensors (*49*), and so on. The essential part of the method lies in the kinetic capturing of the relevant morphology, before the system reaches its equilibrium state. This conceptual approach provides a powerful toolset to obtain desired BC mask morphologies, which are difficult to realize by conventional methods.

3.7 References

1. C. Lu, R. H. Lipson, Interference lithography: a powerful tool for fabricating periodic structures. *Laser Photonics Rev* **4**, 568 (Jul, 2010).
2. C. M. Bates, M. J. Maher, D. W. Janes, C. J. Ellison, C. G. Willson, Block Copolymer Lithography. *Macromolecules* **47**, 2 (Jan 14, 2014).
3. J. Bang, U. Jeong, D. Y. Ryu, T. P. Russell, C. J. Hawker, Block Copolymer Nanolithography: Translation of Molecular Level Control to Nanoscale Patterns. *Adv Mater* **21**, 4769 (Dec 18, 2009).
4. X. D. Gu, I. Gunkel, T. P. Russell, Pattern transfer using block copolymers. *Philos T R Soc A* **371**, (Oct 13, 2013).
5. B. H. Kim, J. Y. Kim, S. O. Kim, Directed self-assembly of block copolymers for universal nanopatterning. *Soft Matter* **9**, 2780 (2013).
6. H. Q. Hu, M. Gopinadhan, C. O. Osuji, Directed self-assembly of block copolymers: a tutorial review of strategies for enabling nanotechnology with soft matter. *Soft Matter* **10**, 3867 (2014).
7. K. Koo, H. Ahn, S. W. Kim, D. Y. Ryu, T. P. Russell, Directed self-assembly of block copolymers in the extreme: guiding microdomains from the small to the large. *Soft Matter* **9**, 9059 (2013).
8. P. Mansky, Y. Liu, E. Huang, T. P. Russell, C. J. Hawker, Controlling polymer-surface interactions with random copolymer brushes. *Science* **275**, 1458 (Mar 7, 1997).
9. C. M. Bates *et al.*, Polarity-Switching Top Coats Enable Orientation of Sub-10-nm Block Copolymer Domains. *Science* **338**, 775 (Nov 9, 2012).
10. T. L. Morkved *et al.*, Local control of microdomain orientation in diblock copolymer thin films with electric fields. *Science* **273**, 931 (Aug 16, 1996).
11. J. G. Son, K. W. Gotrik, C. A. Ross, High-Aspect-Ratio Perpendicular Orientation of PS-b-PDMS Thin Films under Solvent Annealing. *Acs Macro Lett* **1**, 1279 (Nov, 2012).
12. T. Nose, Coexistence Curves of Polystyrene Poly(Dimethylsiloxane) Blends. *Polymer* **36**, 2243 (May, 1995).
13. Y. S. Jung, C. A. Ross, Orientation-controlled self-assembled nanolithography using a polystyrene-polydimethylsiloxane block copolymer. *Nano Lett* **7**, 2046 (Jul, 2007).
14. K. Fukukawa, L. Zhu, P. Gopalan, M. Ueda, S. Yang, Synthesis and characterization of silicon-containing block copolymers from nitroxide-mediated living free radical polymerization. *Macromolecules* **38**, 263 (Jan 25, 2005).
15. A. Nunns, J. Gwyther, I. Manners, Inorganic block copolymer lithography. *Polymer* **54**, 1269 (Feb 18, 2013).
16. C. C. Chao *et al.*, Robust Block Copolymer Mask for Nanopatterning Polymer Films. *Acs Nano* **4**, 2088 (Apr, 2010).
17. M. L. Wadey, I. F. Hsieh, K. A. Cavicchi, S. Z. D. Cheng, Solvent Dependence of the Morphology of Spin-Coated Thin Films of Polydimethylsiloxane-Rich Polystyrene-block-Polydimethylsiloxane Copolymers. *Macromolecules* **45**, 5538 (Jul 10, 2012).
18. M. Park, C. Harrison, P. M. Chaikin, R. A. Register, D. H. Adamson, Block copolymer lithography: Periodic arrays of similar to 10(11) holes in 1 square centimeter. *Science* **276**, 1401 (May 30, 1997).
19. W. B. Bai *et al.*, Thin Film Morphologies of Bulk-Gyroid Polystyrene-block-polydimethylsiloxane under Solvent Vapor Annealing. *Macromolecules* **47**, 6000 (Sep 9, 2014).

20. T. Y. Lo *et al.*, Phase Transitions of Polystyrene-b-poly(dimethylsiloxane) in Solvents of Varying Selectivity. *Macromolecules* **46**, 7513 (Sep 24, 2013).
21. S. Ndoni, P. Jannasch, N. B. Larsen, K. Almdal, Lubricating effect of thin films of styrene-dimethylsiloxane block copolymers. *Langmuir* **15**, 3859 (May 25, 1999).
22. J. E. Mark, *Physical properties of polymers handbook.* AIP series in polymers and complex materials (AIP Press, Woodbury, N.Y., 1996), pp. xv, 723 p.
23. M. Y. Paik *et al.*, Reversible Morphology Control in Block Copolymer Films via Solvent Vapor Processing: An in Situ GISAXS Study. *Macromolecules* **43**, 4253 (May 11, 2010).
24. T. Li, L. Schulte, O. Hansen, S. Ndoni, Nanoporous gyroid TiO2 and SnO2 by melt infiltration of block copolymer templates. *Micropor Mesopor Mat* **210**, 161 (Jul 1, 2015).
25. B. S. Lalia, V. Kochkodan, R. Hashaikeh, N. Hilal, A review on membrane fabrication: Structure, properties and performance relationship. *Desalination* **326**, 77 (Oct 1, 2013).
26. K. S. Kim, K. H. Lee, K. Cho, C. E. Park, Surface modification of polysulfone ultrafiltration membrane by oxygen plasma treatment. *J Membrane Sci* **199**, 135 (Apr 30, 2002).
27. M. L. Steen *et al.*, Low temperature plasma treatment of asymmetric polysulfone membranes for permanent hydrophilic surface modification. *J Membrane Sci* **188**, 97 (Jun 30, 2001).
28. A. K. Geim, Graphene: Status and Prospects. *Science* **324**, 1530 (Jun 19, 2009).
29. A. T. Najafabadi, Emerging applications of graphene and its derivatives in carbon capture and conversion: Current status and future prospects. *Renew Sust Energ Rev* **41**, 1515 (Jan, 2015).
30. S. Sahoo, Quantum Hall effect in graphene: Status and prospects. *Indian J Pure Ap Phy* **49**, 367 (Jun, 2011).
31. F. Schwierz, Graphene Transistors: Status, Prospects, and Problems. *P Ieee* **101**, 1567 (Jul, 2013).
32. A. H. Castro Neto, F. Guinea, N. M. R. Peres, K. S. Novoselov, A. K. Geim, The electronic properties of graphene. *Rev Mod Phys* **81**, 109 (Jan-Mar, 2009).
33. F. Molitor *et al.*, Energy and transport gaps in etched graphene nanoribbons. *Semicond Sci Tech* **25**, (Mar 4, 2010).
34. C. Stampfer *et al.*, Energy Gaps in Etched Graphene Nanoribbons. *Phys Rev Lett* **102**, (Feb 6, 2009).
35. J. W. Bai, X. Zhong, S. Jiang, Y. Huang, X. F. Duan, Graphene nanomesh. *Nat Nanotechnol* **5**, 190 (Mar, 2010).
36. J. Yang *et al.*, Graphene nanomesh: new versatile materials. *Nanoscale* **6**, 13301 (Nov, 2014).
37. L. M. Zhang *et al.*, Photocatalytic Patterning and Modification of Graphene. *J Am Chem Soc* **133**, 2706 (Mar 2, 2011).
38. L. Liu *et al.*, Nanosphere Lithography for the Fabrication of Ultranarrow Graphene Nanoribbons and On- Chip Bandgap Tuning of Graphene. *Adv Mater* **23**, 1246 (Mar, 2011).
39. M. Wang *et al.*, CVD Growth of Large Area Smooth-edged Graphene Nanomesh by Nanosphere Lithography. *Sci Rep-Uk* **3**, (Feb 7, 2013).
40. M. Kim, N. S. Safron, E. Han, M. S. Arnold, P. Gopalan, Fabrication and Characterization of Large-Area, Semiconducting Nanoperforated Graphene Materials. *Nano Lett* **10**, 1125 (Apr, 2010).

41. A. Sinitskii, J. M. Tour, Patterning Graphene through the Self-Assembled Templates: Toward Periodic Two-Dimensional Graphene Nanostructures with Semiconductor Properties. *J Am Chem Soc* **132**, 14730 (Oct 27, 2010).
42. J. Y. Liu *et al.*, Fabrication of Graphene Nanomesh and Improved Chemical Enhancement for Raman Spectroscopy. *J Phys Chem C* **116**, 15741 (Jul 26, 2012).
43. J. G. Son *et al.*, Sub-10 nm Graphene Nanoribbon Array Field-Effect Transistors Fabricated by Block Copolymer Lithography. *Adv Mater* **25**, 4723 (Sep 14, 2013).
44. A. Cagliani *et al.*, Large-area nanopatterned graphene for ultrasensitive gas sensing. *Nano Res* **7**, 743 (May, 2014).
45. K. Celebi *et al.*, Ultimate Permeation Across Atomically Thin Porous Graphene. *Science* **344**, 289 (Apr 18, 2014).
46. K. R. Williams, R. S. Muller, Etch rates for micromachining processing. *J Microelectromech S* **5**, 256 (Dec, 1996).
47. M. E. Warkiani *et al.*, Isoporous micro/nanoengineered membranes. *Acs Nano* **7**, 1882 (Mar 26, 2013).
48. B. N. Miles *et al.*, Single molecule sensing with solid-state nanopores: novel materials, methods, and applications. *Chem Soc Rev* **42**, 15 (Jan 7, 2013).
49. A. de la Escosura-Muniz, A. Merkoci, Nanochannels preparation and application in biosensing. *Acs Nano* **6**, 7556 (Sep 25, 2012).

Chapter 4

Fast & Scalable Pattern Transfer via Block Copolymer Nanolithography

4.1 Introduction

In this chapter, a fully scalable and efficient pattern transfer process based on block copolymer (BCP) self-assembly directly on various substrates is demonstrated. The pattern is directly formed during spin-casting at room temperature, which takes less than 20 seconds, without any preliminary surface treatment of the substrate and without any subsequent annealing.

Pattern transfer at nano-scale has been an essential part of the whole nanotechnology. Challenges arise from the increasing cost and limited resolution of top-down approaches like deep-UV optical lithography. On the other hand, the low throughput e-beam lithography and interference techniques are not suitable for efficient large area patterning.(*1*) Self-assembly of block copolymers can give highly ordered nanostructures with varying morphology on sub-10 nm scale, making it a promising technique to meet the key challenges of small feature size with high resolution and high throughput at low cost.(*2, 3*) Various BCP patterns with narrow size distribution and perfect alignment have been created so far;(*4-7*) however, the pattern transfer process by such method is seldom demonstrated. There is still a need for a facile and versatile approach using block copolymers with large etching contrast and substrate independence to

succeed in a number of applications where the perfect lateral ordering of the nano-pattern is not necessary such as solar cells, catalysis, separating membranes, etc.

When BCP films are spin-cast, they are often kinetically trapped in disorganized form far from equilibrium state. Therefore an annealing process, such as thermal annealing(*8*) and solvent vapor annealing(*9*), is generally needed to generate structural order by increasing the chain mobility and allowing for BCP micro-domain separation. The annealing step indeed increases the complexity and cost of fabrication, and some aspects of these processes might be challenging to implement in industry. In addition to the annealing process, nearly in all the BCP lithography studies, the substrates have to be treated prior to BCP deposition. For an example, by applying a random copolymer with controlled composition covalently bonded to the substrate, a so called brush layer, a neutral surface energy for both of the polymers can be adjusted so the BCP orientation can be aligned normal to the substrate.(*10*) This approach, however, requires anchoring chemical groups present both in the substrate and brush polymer, which limits its application. Other examples including homo-polymer brush layer,(*11*) or substrate chemical functionalization,(*12*) are routinely applied to increase the BCP chain mobility, prevent de-wetting or control the orientation.

Fast pattern generation directly after spin-casting has been reported for poly(styrene-*b*-ethylene oxide) (PS-PEO)(*13, 14*) and poly(styrene-*b*-lactide) (PS-PLA)(*15, 16*) with perpendicular cylindrical morphology. The evaporation rate and solubility parameter of the solvents play a key role in determining the microdomain orientation. However, the PEO block cannot be removed easily by chemical etching.(*17*) In the case of PS-PLA, if the PLA domain is removed by

hydrolysis with a base, the remaining PS is a poor mask for pattern transfer process. Deposition of block copolymer micelles from selective solvents can produce nano-pattern directly on the substrates.(*18*) But the casting condition is tedious and delicate.(*19, 20*) And in order to improve the etching resistance of the mask, an extra step of inorganic precursor infiltration is applied before the nano-pattering process.(*19, 21, 22*)

Here we introduce a large-scale and facile pattern transfer process by in situ block copolymer nanolithography. The in situ PS-PDMS pattern is realized from selective solvent spin-casting, giving monolayer sphere morphology, which allows avoiding the orientation control for nano-patterning. We successfully transfer the pattern to various substrates including common polymers and silicon, without any substrate pretreatment and annealing steps. We also demonstrate an in situ Al_2O_3 hard mask fabrication technique by ALD to generate high aspect ratio (exceeding 10) nanostructured porous silicon with sub-15 nm feature size.

4.2 Morphology control by selective solvent

In this section, selective solvent spin-casting is shown to produce various morphologies with relatively good distribution. This method is proved to be effective on a broad PS-PDMS composition and molecular weights.

Materials: All the solvents are purchased from Sigma Aldrich without further purification (except for the BC synthesis). SD67 (21-b-46 kg mol^{-1}, Polymer Source), SD81 (26-b-55 kg

mol^{-1}, Polymer Source), SD23 and SD39 are synthesized by living anionic polymerization following already reported procedure.(*23*)

Fabrication: All the SDs with concentration of 0.3 wt% to 0.5 wt% spin-cast at 1500 rpm for 20 seconds to give 12 – 22 nm thick films.

Characterization: ^{1}H-NMR is done in deuterated chloroform, using a 400 MHz NMR from Bruker. The SEC is done using THF as a solvent. The system from Shimadzu, LC-10AD (Pump), SIL-10AS (Autosampler), is combined with Detectors from Viscotek, namely a RALLS Detector (Model LD600) as well as a Differential Refractometer/Viscometer (Model 200) combination. The columns are: one PLgel 5μm Mixed D from Polymer Laboratories in series with one Styragel HMW 6E from Waters. The PS block of the polymers is analyzed using the Refractive Index signal in combination with a conventional calibration against PS standards, while calculations of PDI for the BCs, is done by analyzing the combined Light Scattering and Refractive Index responses. The block copolymer solutions used in spin-casting are characterized by dynamic light scattering, DLS, in a Brookhaven instruments corporation instrument, consisting of a BI-200SM goniometer, a BI-APD detector and a 633nm laser from Melles Griot, 25-LHP-928-249 ; the scattered light is collected at 90º and the data are analyzed by Dynamic light scattering software from brookhaven instruments, vers. 5.89/5.9/5.8. Film thickness is determined by a VASE Ellipsometer (J.A. Woollam) at three different incidence angles (55^{o}, 60^{o} and 65^{o}). Scanning electron microscopy (SEM) images are taken by a Field Emission Zeiss Ultra Plus scanning electron microscope with a Gemini column operating at an accelerating voltage of 2kV.

Results and discussion: Five SDs with different number-average molecular weights (M_n) and composition are investigated, as summarized in Table 1. The PS volume fraction is in the range of 24-30% or 60-70%, which is within the typical composition range for cylinder bulk morphology. SD23 and SD39 are synthesized in our lab by living anionic polymerization with a low polydispersity index (PDI ≤ 1.03). SD67 and SD81 are purchased with somewhat higher PDI.

Table 1. PS-b-PDMS Copolymer Characteristics

Sample ID	f_{PS}	M_{PS} (kg/mol)	M_{Total} (kg/mol)	PDI
SD23	64.8% [a]	15.9 [b]	23.1 [c]	1.02 [d]
SD39	66.1% [a]	27.2 [b]	38.9 [c]	1.03 [d]
SD67	29.7% [a]	21.0 [e]	67.0 [e]	1.45 [e]
SD81	30.4% [a]	26.0 [e]	81.0 [e]	1.25 [e]

[a] Calculated from ^{1}H NMR spectra using ρ_{PDMS} = 0.97 g/cm^3 and ρ_{PS} = 1.05 g/cm^3.

[b] From SEC analysis calibrated with PS standards.

[c] Calculated from f_{PS} and M_{PS} .

[d] From SEC analysis of the combined RI and LS signals

[e] From the supplier (Polymer Source)

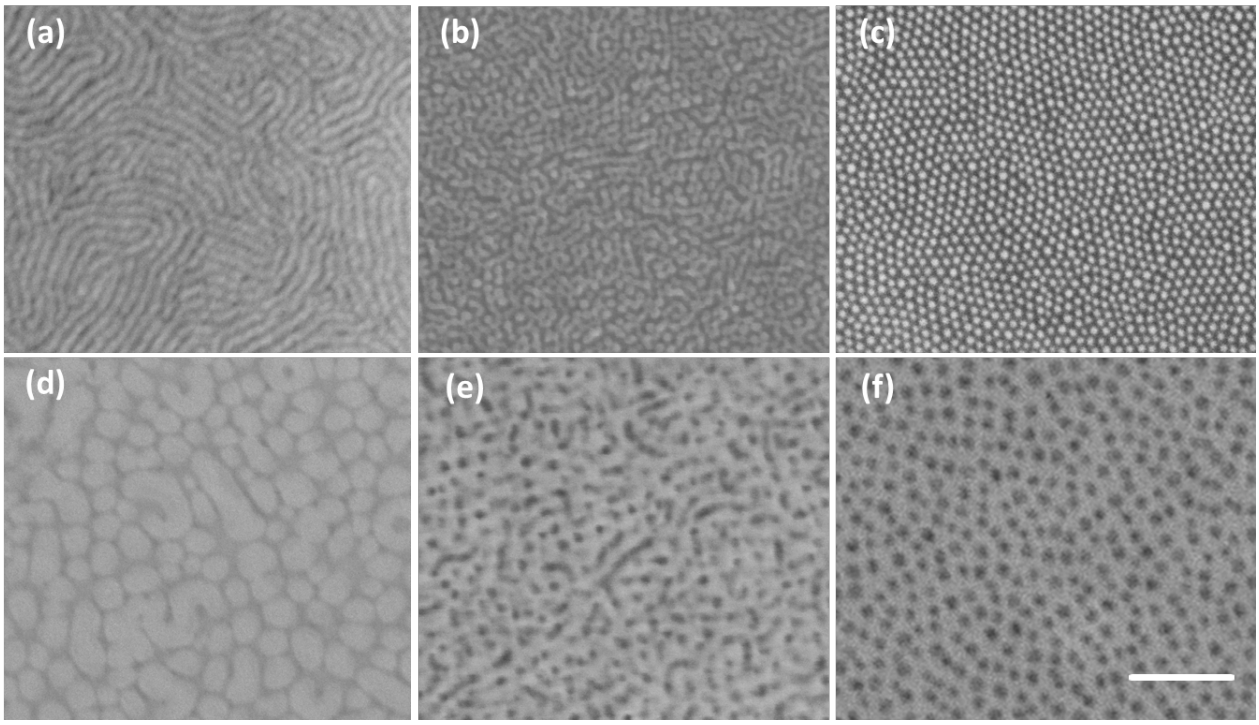

Figure 4.1 Top view SEM images of the SDs after spin-casting: (a-c) PS-rich SD39 spin-cast from (a) toluene, (b) tetrahydrofuran and (c) cyclopentanone with thickness in the range of 15-20 nm; (d-f) PDMS-rich SD67 spin-casting from (d) toluene, (e) methylcyclohexane and (f) hexane with the thickness around 20 nm. All the samples are spin-cast on a silicon wafer and treated with fluorine and oxygen plasma to increase contrast. Scale bar: 200 nm.

Preferential inclusion of the solvent to one block of the BCP is well known to shift the morphology.(*24-26*) The interaction between the solvent and polymer can be considered in terms of Hildebrand solubility parameters (HSP), which are summarized in Table 2 for all the solvents used in this study. Fig. 4.1 shows the pattern of the SD39 and SD67 on silicon substrate after spin-casting from several solvents. For the PS-rich SD39 shown in Fig. 4.1a to Fig. 4.1c, the morphology changes from cylinder to sphere when the casting solvent changes from little selective (toluene) to highly PS-selective (cyclopentanone). An intermediate state consisting of both lines and dots is also captured by tetrahydrofuran which has the HSP value in between. The

morphology in Fig. 4.1c is a monolayer of hexagonally packed spheres with lateral domain size around 200 nm. A similar trend is observed for PDMS-rich SD67 shown in Fig. 4.1e to Fig. 4.1f, although the morphology transition to a monolayer of spheres is less evident compared to SD39. We suspect the difference is due to the limited mobility of the glassy PS-chain when cast in a non-solvent for PS, accentuated by the bigger molecular weight of SD67. In the case of SD39, the rubbery nature of the PDMS makes it easier to self-assemble into more regular pattern. The sphere morphology is clear for SD67 but the lateral order is completely missing, which may be due to its larger PDI. What's more, defects in the film cast from less selective solvents are readily presenting. In contrast, the film is very uniform and homogeneous when cast from the highly selective solvents. The thickness of the final film is slightly smaller than the corresponding sphere packing period, which supports the scenario that the sphere self-assembly occurs at the stage when there is still solvent present and then the morphology is trapped as the remaining solvent evaporates. When a thicker film is cast, multi-layers of spheres are observed, as shown in Fig. 4.2.

Table 2. Solubility parameters (*)

Solvent	Solubility parameter ($MPa^{1/2}$)
Hexane	14.9
Methylcyclohexane	16.2
Toluene	18.2
Tetrahydrofuran	18.6
Cyclopentanone	21.3
PDMS	15.0 (*27*)
PS	18.5 (*11*)

(*) Solvent values were calculated from the evaporation enthalpies and molar volumes given in ref. (*28*)

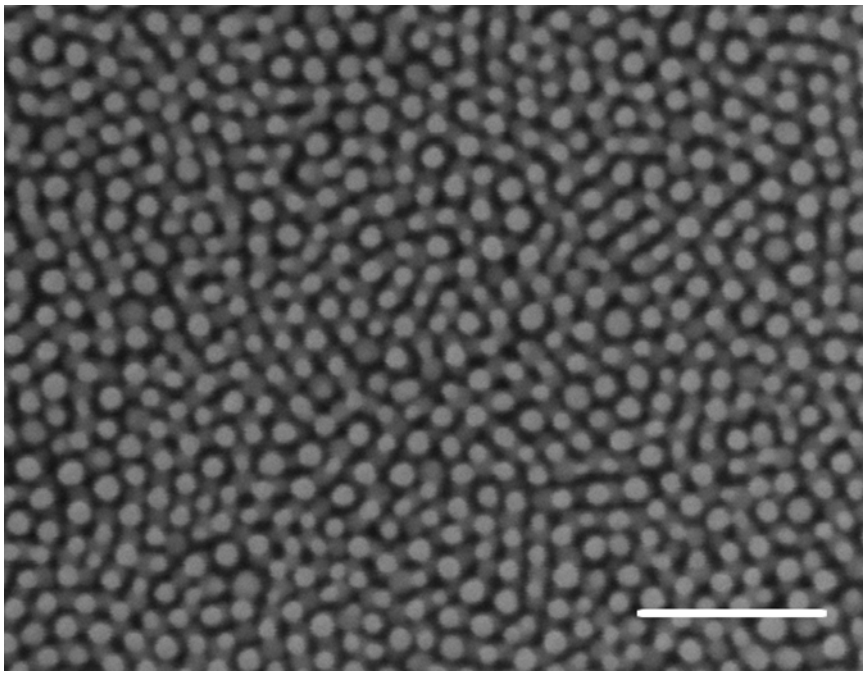

Figure 4.2. Top-view SEM image of the 90 nm thick SD39 film spin-cast on a silicon wafer and treated with fluorine and oxygen plasmas to enhance contrast. A multilayer of spheres is clearly visible. Scale bar: 200 nm.

The same strategy is effective for the other two SDs with different molecular weights but similar compositions, as displayed in Fig. 4.3a and Fig. 4.3c. A relatively narrow size distribution of the nano-features is evident, even before the annealing step (see the discussion relative to Table 3 below). In order to improve the ordering, solvent vapor annealing is conducted for these two SDs. Fig. 4.3b and Fig. 4.3d shows well-ordered morphology with lateral domain size exceeding 1 micrometer, which makes this technique also attractive for applications where the lateral order is required. This strategy could be used as a general guideline to make monolayer packed sphere patterns from bulk-cylindrical SDs with different length scale by changing the molecular weight and composition.

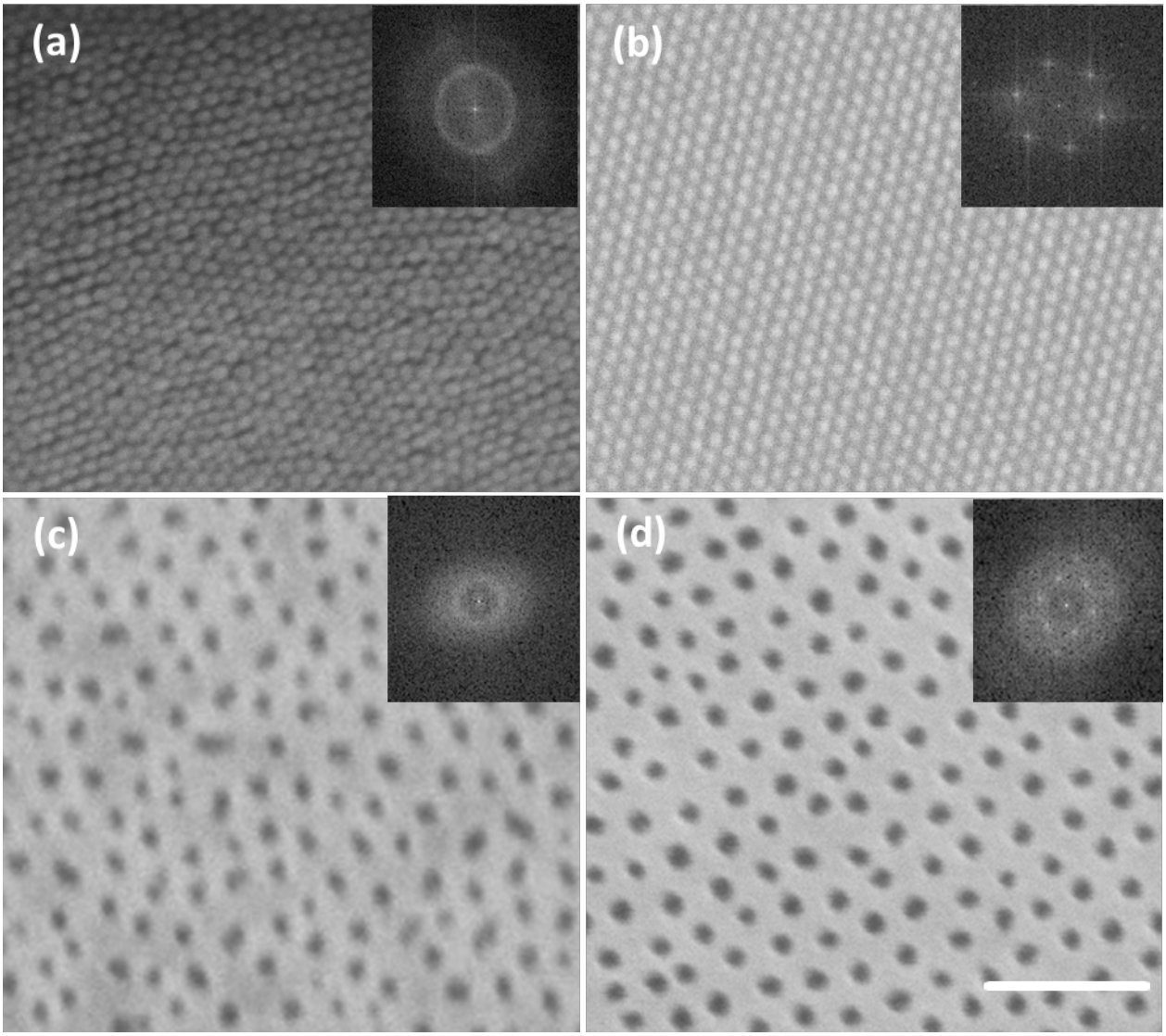

Figure. 4.3 Top view SEM images of (a) SD23 spin-cast from cyclopentanone, (b) SD23 annealed in cyclopentanone for 1 hour, (c) SD81 spin-casting from methylcyclohexane and (d) SD81 annealed in methylcyclohexane for 1 hour. All the samples are spin-cast on a silicon wafer and treated with fluorine and oxygen plasma to increase contrast. Scale bar: 200 nm. Inset: fast Fourier transforms of the SEM images.

In the extreme cases, using strongly minority selective solvent can induce phase reversion as shown in the Fig. 4.4.

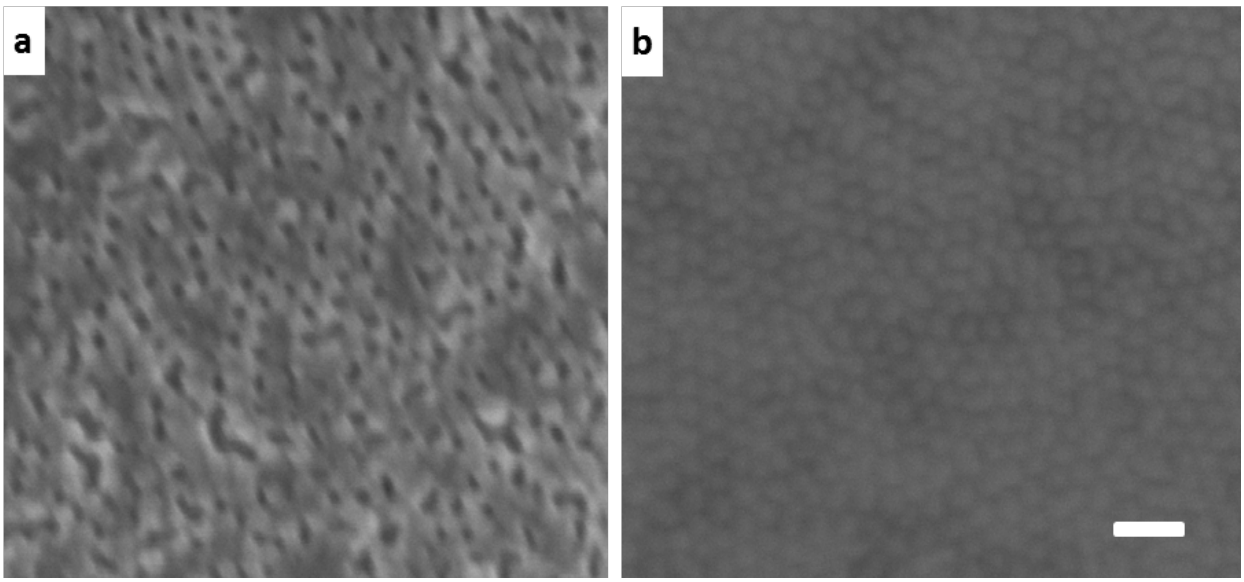

Figure. 4.4 Top view SEM images of (a) SD39 spin-cast from hexane, (b) SD81 spin-casting from cyclopentanone. All the samples are spin-cast on a silicon wafer and treated with fluorine and oxygen plasma to increase contrast. Scale bar: 200 nm. Inset: fast Fourier transforms of the SEM images.

Dynamic light scattering of the BCPs in the spin casting solutions were recorded in order to understand the formation of the rather well-ordered structures immediately after the spin-casting step. The obtained data are shown in the second and third columns of Table 3. The effective hydrodynamic diameters measured in toluene are significantly smaller than the effective diameters in the respective selective solvents (Fig. 4.4). Toluene is a good solvent for both blocks and the BCP molecules are expected to be fully dissolved; therefore the shown values correspond to hydrodynamic dimensions of single BCP macromolecules. In contrast the larger values in the selective solvents indicate formation of micelles, most probably spherical micelles for SD23, SD39, SD81 and elongated micelles for SD67. The last two columns in Table 3 show data derived from the SEM images in Fig 1c,f and 2a,c. It has not been possible to find a clear correlation between the micelle size as measured by DLS and the structural period derived by

SEM. With the exception of SD67 the DLS micelle sizes are 2.5 – 3.6 times smaller than the corresponding thin film periods.

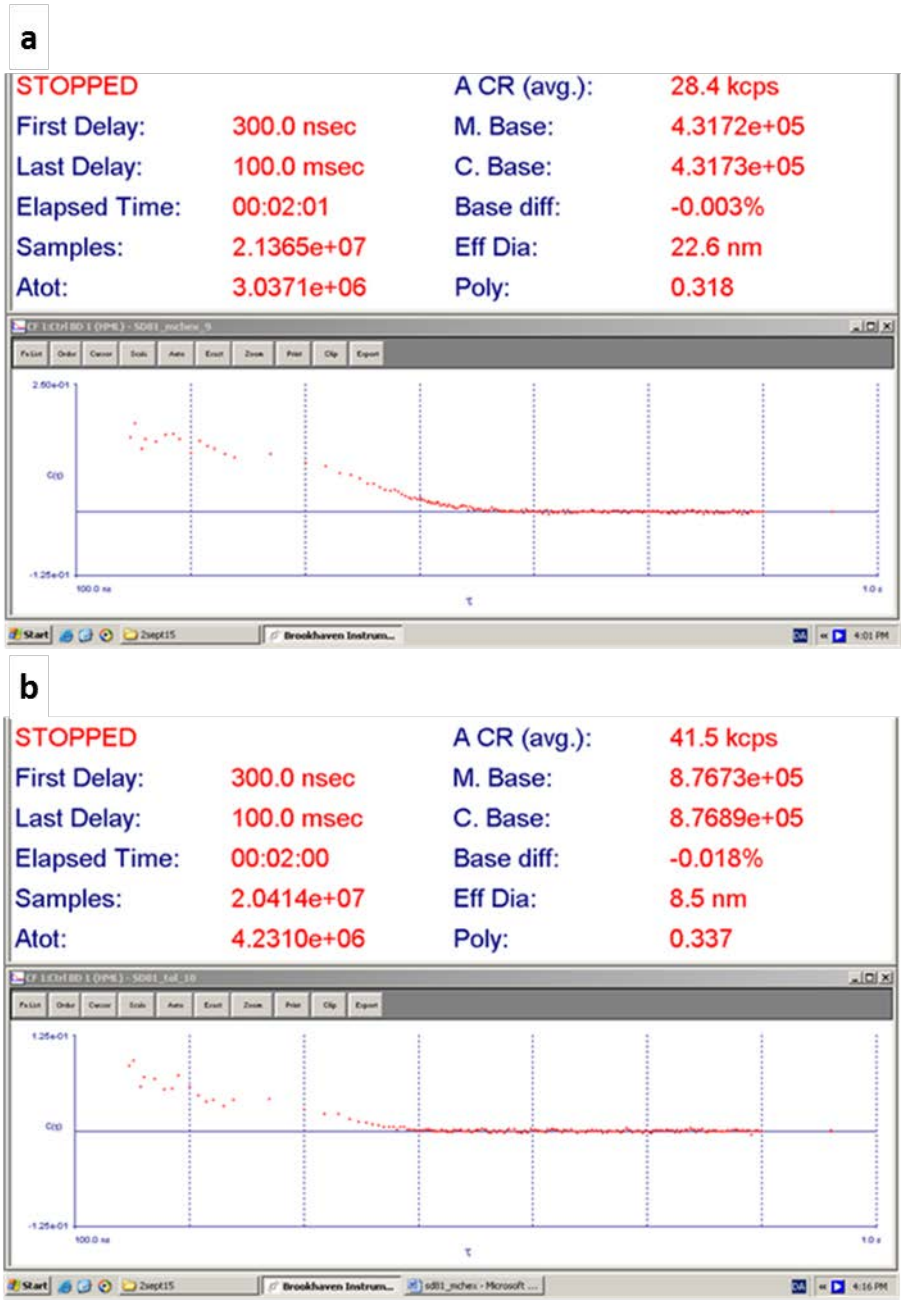

Figure. 4.4 DLS results of (a) SD81 spin-cast from methylcyclohexane, (b) SD81 spin-casting from toluene

This discrepancy hints at a reorganization of the micelles in the process of spin-casting from selective solvents. The significant shear forces during spin-casting would deform and disrupt the micelles that then reorganize before the PS block becomes glassy as a result of solvent evaporation. The reason why SD67 forms worm-like micelles could be related to the relatively high molecular weight polydispersity of this block copolymer and to the extreme selectivity of hexane as a solvent (see Table 2). During spin-casting these micelles are also disrupted and there remains no sign of worm-like structures in the thin film after spin-casting (Fig 1f).

A last comment relative to the SEM feature sizes listed in tab. 3. The shown standard deviation values are moderate indicating a rather narrow feature size distribution realized by our fast process. Of course, even lower standard deviation values are realized after annealing, as is evident by inspection of figs. 2b,d. In both these cases the standard deviation from the mean is reduced by a factor of 2.3 relative to the values of the not annealed samples.

Table 3. Effective hydrodynamic diameter of the BCPs in non-selective and selective solvents measured by DLS together with the structural feature diameter and period measured by FFT and particle size analyses of the SEM images.

Sample ID	BCP in Toluene (nm)	BCP in selective solvents (nm)	Feature size (nm)	Period (nm)
SD23	2.3	8.1	14.0 ± 5.0	20.1
SD39	3.3	9.5	20.2 ± 3.2	34.7
SD67	7.6	83	25.8 ± 7.4	43.5
SD81	8.3	23	23.8 ± 7.0	56.6

3.3 Pattern transfer on polymer substrate

In this section, the pattern generated in last section is used the hard mask directly for polymer substrates etching without any substrate modification and annealing process, which is taken as a routine step in nearly all the similar work found in literatures.

Materials: SU8-2002 (MicroChem), Poly(methyl methacrylate) (PMMA, 70k, Diakon), Polysulfone (PSF 27k, Scientific Polymers), Polylactide (PLA M_w 18k-28k, Sigma Aldrich) and 1, 4-polybutadiene (PB Scientific Polymers, *MW* 100k, crosslinking procedure:(*29*))

Fabrication: SU8 (7 wt% in Cyclopentanone) is spin-cast at 5000 rpm for 30 seconds to give a 110 nm thick film, and then is put onto a hot plate for crosslinking at 250 ^{o}C for 15 minutes.

The dry etch process is performed on an Advanced Silicon Etcher (STS MESC Multiplex ICP serial no. 30343). SF_6 plasma condition to remove PDMS top wetting layer: 20 sccm SF_6, 20 mTorr, coil power: 50w and platen power: 0w, 8 – 20 seconds. O_2 plasma condition to remove PS/polymer substrate and oxidize PDMS: 10 sccm O_2, 5 mTorr, coil power: 200w and platen power: 10w. The etching rate of the SU8 is estimated to be 3 nm/s as measured by ellipsometry. SF_6 plasma condition for breakthrough of the PDMS-substrate wetting layer: 20 sccm SF_6, 5 mTorr, coil power: 100w and platen power: 5w, 3 seconds. The silicon etching by fluorine RIE is performed on ASE. Etching step: 10 sccm SF_6, 5 mTorr, coil power: 100w and platen power: 5w, 10-25 seconds.

Characterization: Film thickness is determined by a VASE Ellipsometer (J.A. Woollam) at three different incidence angles (55^o, 60^o and 65^o). Scanning electron microscopy (SEM) images are taken by a Field Emission Zeiss Ultra Plus scanning electron microscope with a Gemini column operating at an accelerating voltage of 2kV. The cross-section is taken at a tilt angle of 45^o. All the samples are imaged directly without coating or staining.

Results and discussion: The overall nano-patterning process on polymer substrate by SD81 is conducted by RIE, which is summarized in scheme 1.

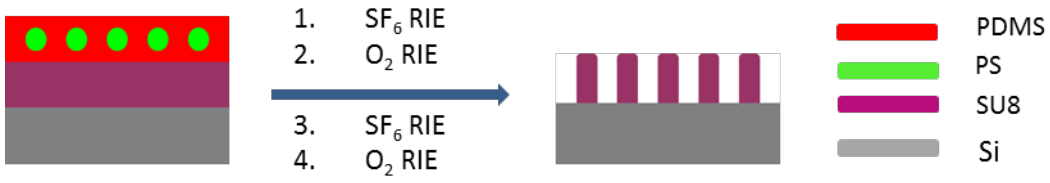

Scheme. 1. Pattern transfer process on SU8 substrate by SD81 mask.

For a successful sphere pattern transfer, a short SF_6 RIE is firstly applied to remove a thin layer of PDMS top wetting layer. Due to the low surface energy of PDMS compared to PS, this wetting layer of PDMS is almost always present at the air interface in SD film.(*30*) Following O_2 RIE removes the PS domain and oxidizes PDMS into a hard mask, which can act as a hard mask for the successive nano-patterning process. In the case of PDMS-rich SD, an additional SF_6 RIE step is needed to break through the lower PDMS wetting at the substrate interface. Otherwise this thin PDMS layer will block the pattern transfer under O_2 RIE (Fig. 4.5).

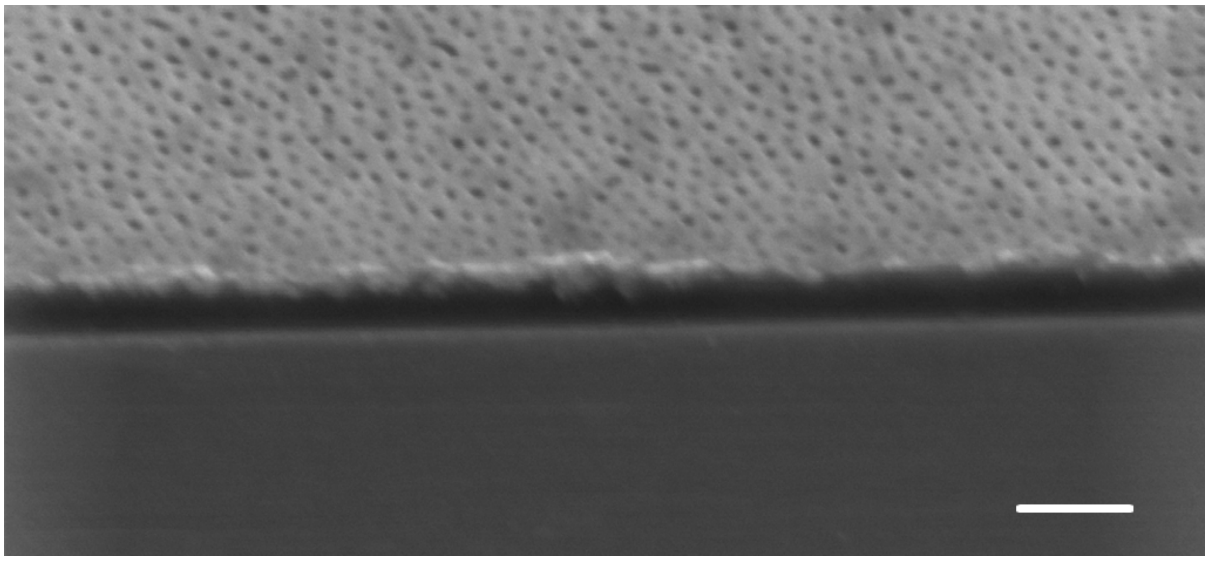

Figure 4.5. Tilted SEM image after an attempt to transfer the pattern from SD81 onto SU-8 by O_2 RIE without removing the PDMS wetting layer at the substrate interface. This wetting layer effectively blocks access of the O_2 RIE to the substrate. Scale bar: 200 nm.

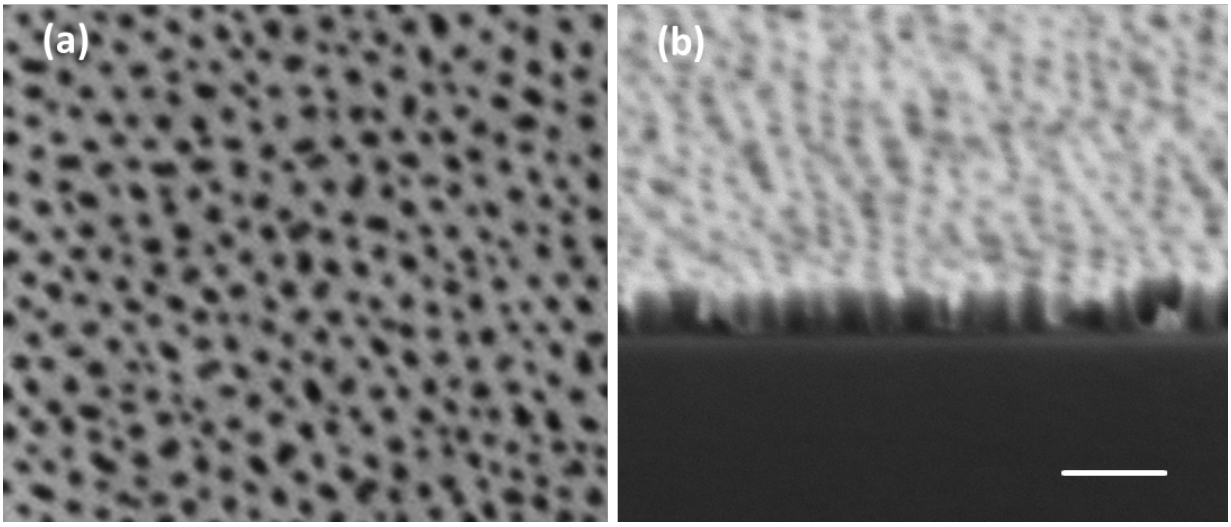

Figure 4.6. Top view (a) and tilted (b) SEM images of SD81 pattern transfer onto SU-8 by O_2 RIE. The SDs are directly spin-cast on the substrate without any annealing process and the transferred pattern is well replicated from the mask. Scale bar: 200 nm.

Fig. 4.6 shows the cross-linked 110 nm thick SU8 substrate, which is a widely used photo-resist in silicon industry, (*31*) patterned by SD81. The obtained SU-8 nano-wells can be further used as an etching mask or as templates to fabricate other functional materials, for example, 1D nano-rod arrays by electro-deposition or ALD.(*32, 33*) Because the casting solvent of methylcyclohexane is a non-solvent for polylactide (PLA), PMMA and polysulfone (PSF), the SD81 mask works similarly on these polymer substrates, as well as on highly cross-linked polybutadiene (PB). (Fig. 4.7). This technique is very attractive as an ultra-fast way for polymer patterning.

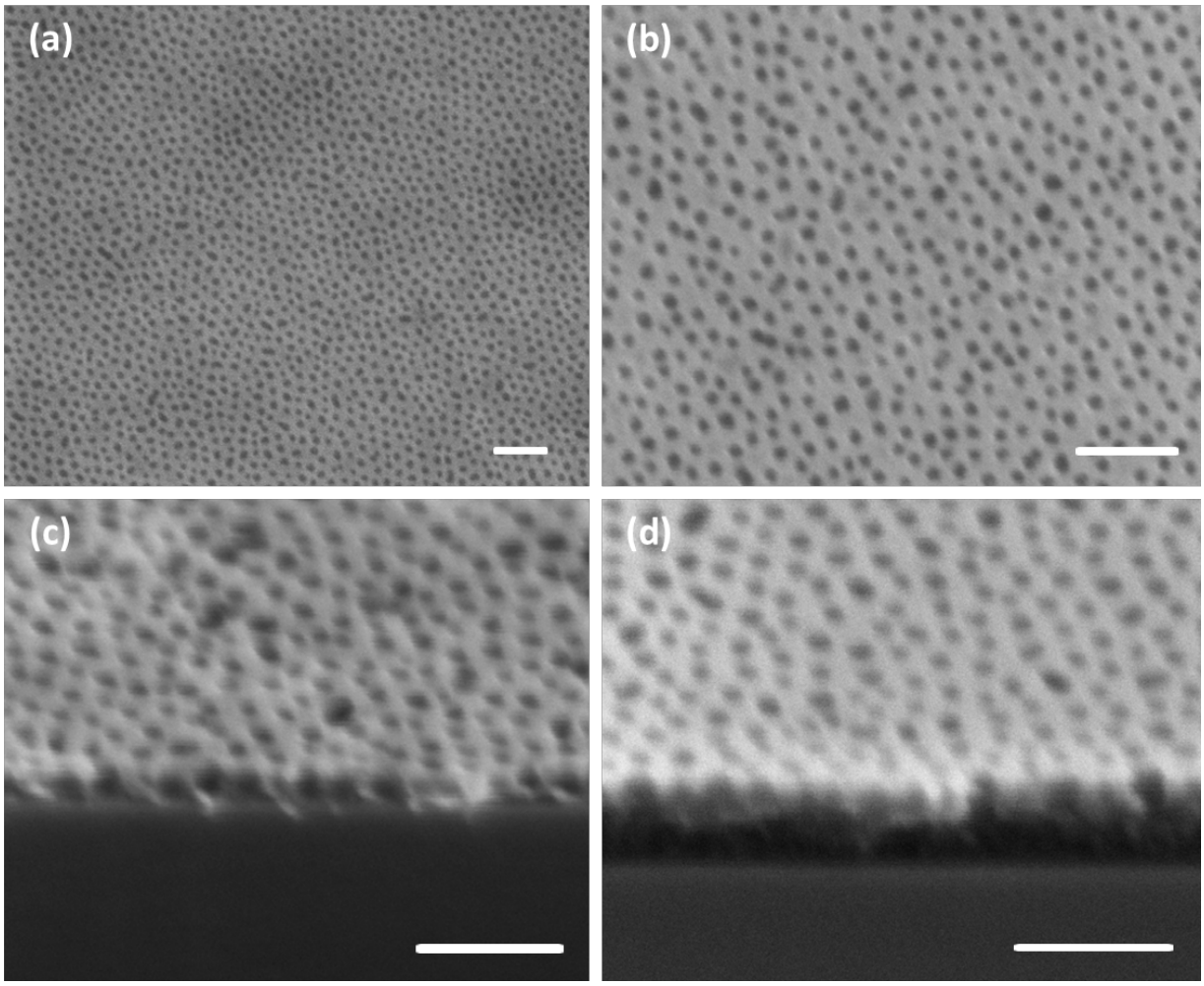

Figure 4.7 Top-view SEM images of (a) PLA patterned by SD81 and (b) PSF patterned by SD81. Tilted SEM images of (c) PB patterned by SD81 and (d) PMMA patterned by SD81 with partial pattern transfer. Scale bar: 200 nm.

4.4 In situ hard mask for deep silicon etching

Introduction: High-aspect ratio nanostructured silicon has many important applications. In this section, Al_2O_3 hard mask is created in situ by ALD in order to improve the dry etch selectivity.

Fabrication: The silicon etching by a pseudo-Bosch process is performed on ICP Metal etch (SPTS Serial number MP0637). Recipe: 38sccm SF_6 and 70sccm C_4F_8, 14 mTorr, coil power: 200w and platen power: 20w, time range from 10 to 20 seconds.

The Al_2O_3 breakthrough and silicon etching is performed on ICP Metal etch (SPTS Serial number MP0637). Cl_2 etching: 20 sccm Cl_2, 3 mTorr, coil power: 300w and platen power: 40w. The etching rate of Al_2O_3 is estimated to be 0.11 nm/s as measured by ellipsometry.

The ALD is conducted in Picosun ALD model R200, using alternating exposures to trimethylaluminum (97%, Aldrich) and deionized water at 200 ^oC for 300 cycles with N_2 gas purge step in between. The exposure and purge time for both precursors used in this study is 2 and 25 seconds respectively.

Characterization: Scanning electron microscopy (SEM) images are taken by a Field Emission Zeiss Ultra Plus scanning electron microscope with a Gemini column operating at an accelerating voltage of 2kV. All the samples are imaged directly without coating or staining. XPS measurement is performed on a XPS-ThermoScientific instrument

Results and discussion: The initial attempt of pattern transfer using SD39 on polymer substrate by O_2 RIE failed (Fig. 4.8). The film thickness is readily reduced as the etching goes on but only the sphere mask can be observed. This may be due to its smaller feature size, which makes the under-cutting inevitable during the dry etching process.

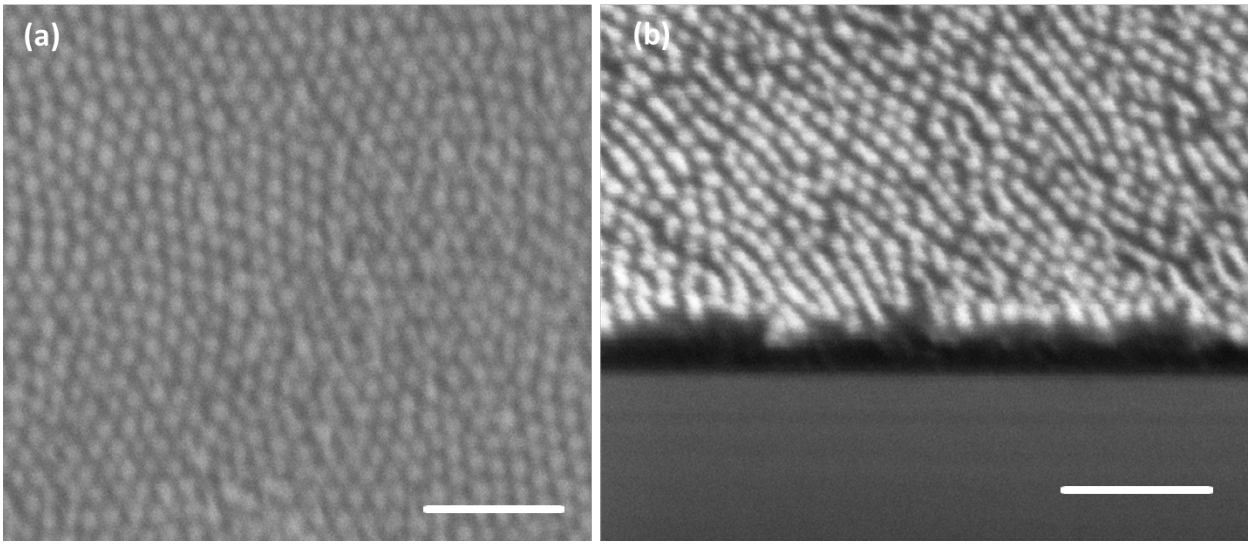

Figure 4.8 Top-view (a) and tilted (b) SEM images of SU-8 after a patterning attempt by O_2 plasma in the presence of a hard mask derived from SD39. A layer of about 40 nm SU-8 has been removed by the plasma; however no pattern transfer can be discerned on the remaining SU-8 (see discussion in the manuscript). Scale bar: 200 nm.

On the other hand, pattern transfer to silicon by SD39 is conducted by several fluorine-based RIE recipes, which also proved to be unsuccessful. The selectivity of the mask to the silicon substrate under this condition is estimated to be less than 1, which suggests that the oxidized PDMS is a poor mask under SF_6 RIE. A pseudo-Bosch recipe is also tested, in which C_4F_8 gas is introduced as the passivation step to prevent the undercutting in silicon etching. This recipe is deliberately designed for nanostructured silicon etching with small length scale, such as using deep-UV

lithograph process. However, the results are not improved. This suggests that silicon etching at very small length scale is quite challenging.

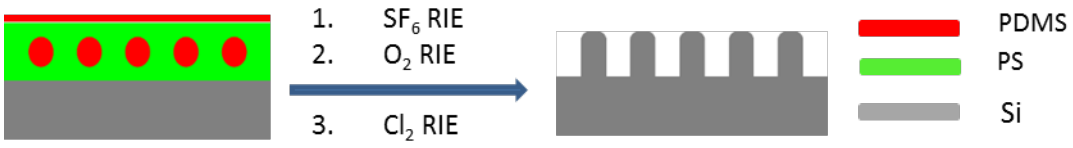

Scheme. 1. Pattern transfer process on silicon substrate by SD39 mask.

Surprisely, we find that the oxidized PDMS masks can be used not only for patterning carbonaceous materials by oxygen RIE, as demonstrated in Scheme 2.

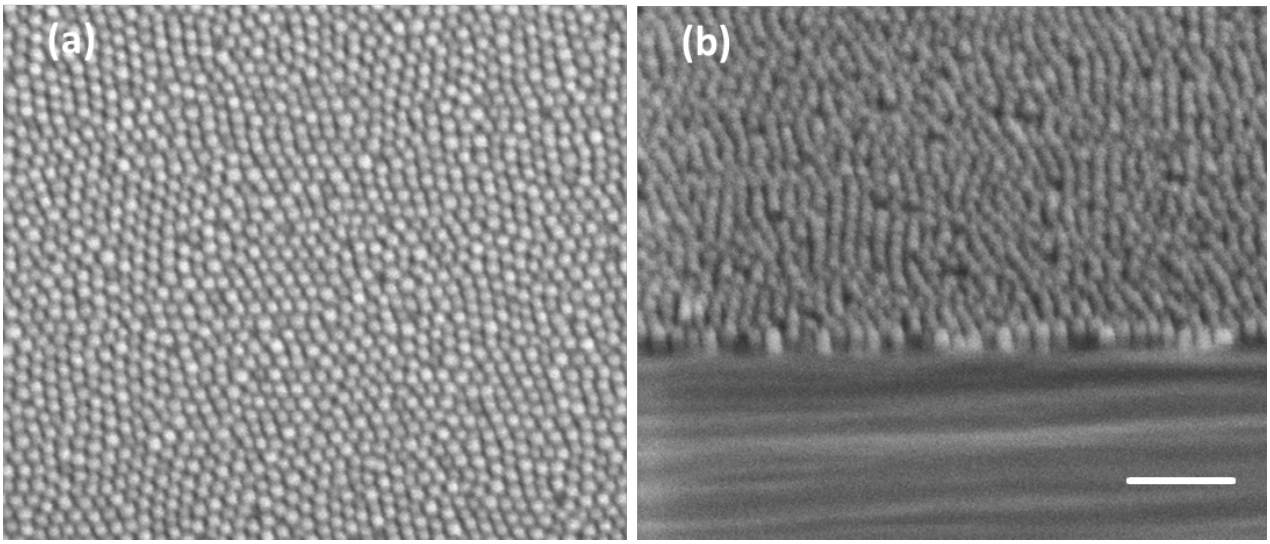

Figure. 4.9 Top view (a) and tilted (b) SEM images of SD39 pattern transfer onto silicon substrate by chlorine RIE. The SDs are directly spin-cast on the substrate without any annealing process and the transferred pattern is well replicated from the mask. Scale bar: 200 nm.

They also show higher resistance over silicon under chlorine RIE as demonstrated by the SEM images in Fig. 4.9 using SD39 mask. Unlike the isotropic oxygen plasma etching for polymer and fluorine plasma etching for silicon, the silicon etching by chlorine plasma is highly anisotropic.(*34*) Therefore, regular arrays of silicon nano-pillars are obtained by direct application of chlorine plasma to the oxidized PDMS mask. As the chlorine RIE also etches the oxidized PDMS slowly, the mask can be fully removed simultaneously, which is evidenced by the absence of the carbon peak in X-ray photoelectron spectroscopy (XPS). The selectivity of this mask under these conditions is estimated to be 7.

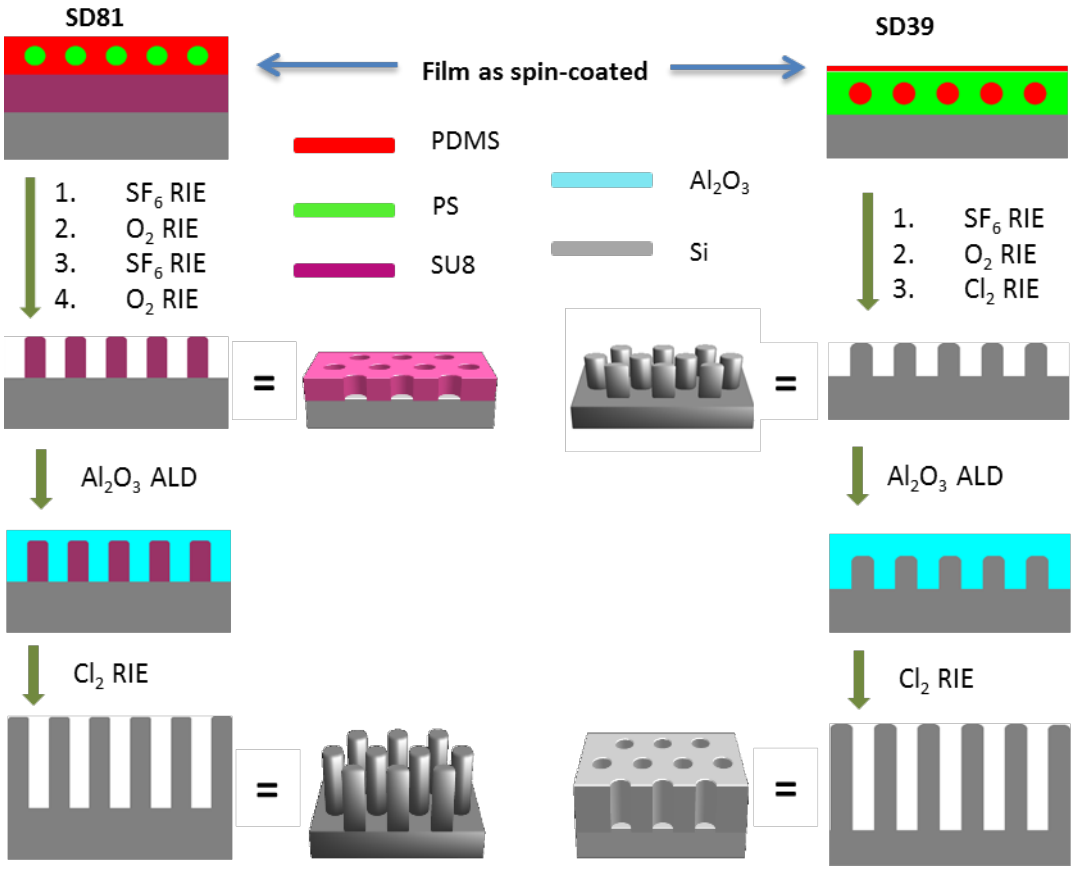

Scheme. 3 Illustration of the overall pattern transfer process in this study.

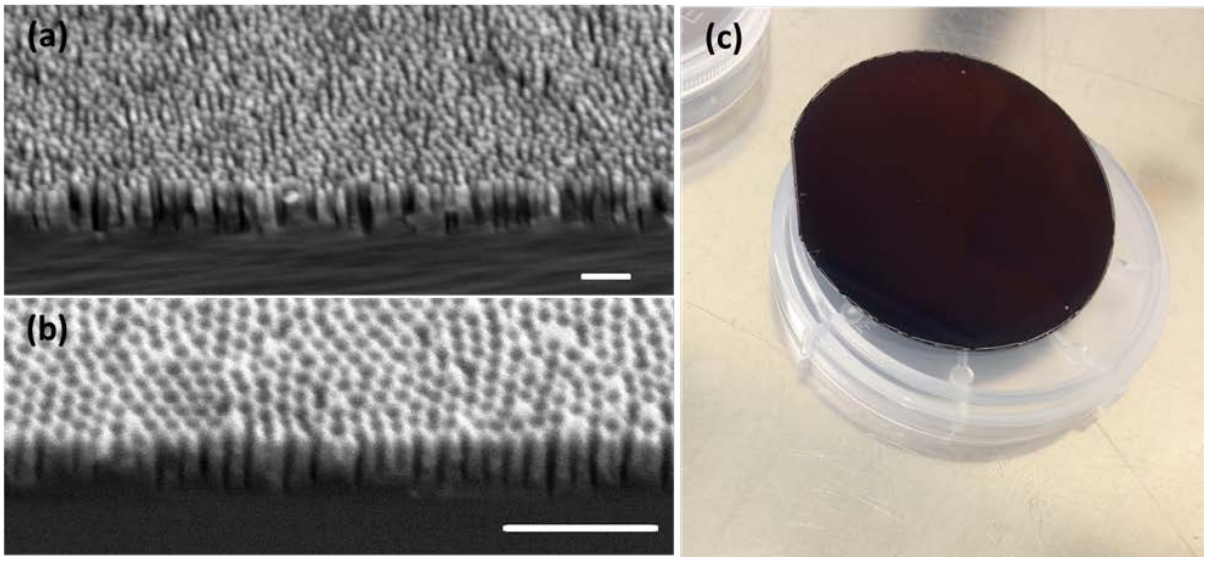

Figure 4.10 Tilted SEM images of (a) silicon nano-pillar arrays made by Al_2O_3 hard mask derived from SU-8 (50nm) patterned by SD81 and (b) silicon nano-mesh arrays made by Al_2O_3 hard mask derived from SD39. Wafer scale black silicon can be created by this direct lithography process without defects (c). Scale bar: 200 nm.

High-aspect ratio nanostructured silicon has many important applications. In order to improve the dry etch selectivity, Al_2O_3 hard mask is created in situ by ALD, which is widely used in nanolithography processes,(*35-37*) as shown in scheme 3 and Fig 4.10. 26 nm of Al_2O_3 is deposited conformably onto the pre-patterned substrates, which is sufficient to fill the pores (Fig. 4.11). In a single chlorine RIE step, after the breakthrough of the top layer, part of the Al_2O_3 mask is removed and the remaining mask acts as the hard mask for silicon etching. This process causes a reversal of the pattern relative to the initial mask pattern. Alternatively, we also tested several fluorine-based RIE recipes after the break-through step, including Bosch process and pseudo Bosch process,(*21, 38*) in which the etching of Al_2O_3 mask is negligible.(*39*) However, the pattern is readily destroyed even at very shallow etching, which indicates that at very small

length scale, the etching by SF_6 and passivation by C_4F_8 need to be finely adjusted in order to avoid undercutting. On the other hand, due to the high anisotropic etching nature, it is straightforward to apply chlorine RIE to break through the mask and transfer pattern to the silicon substrate in a single dry etch step. As a result, high-density and high aspect ratio (exceeding 20) arrays of silicon nano-pillars or nano-wells with sub-15 nm feature size (patterned by SD39) are fabricated over wafer scale (Fig. 4c). The selectivity is estimated to be 25 at the test condition and the Al_2O_3 mask can be easily removed by HF (40%) solution (confirmed by XPS).

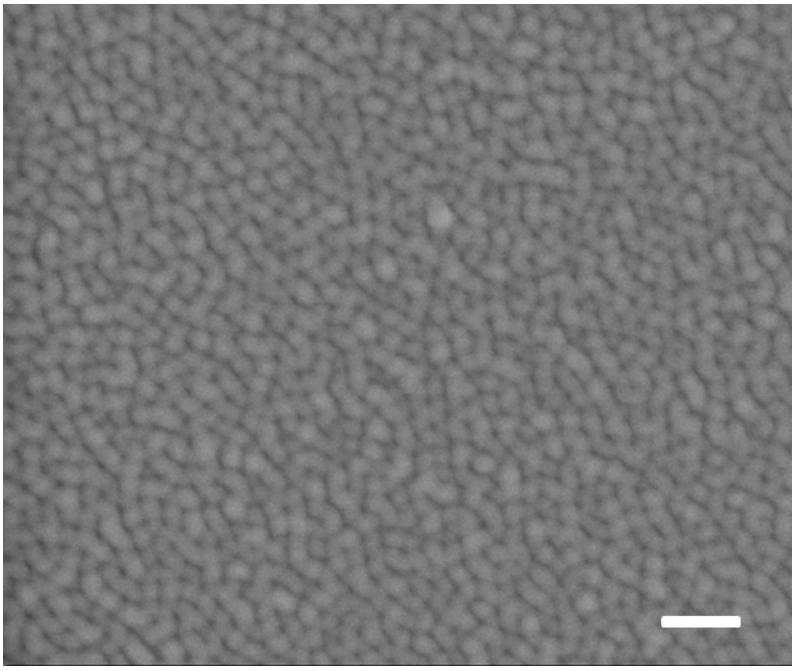

Figure 4.11. Top-view SEM image of SU-8 patterned by SD81after Al_2O_3 ALD. Scale bar: 200 nm.

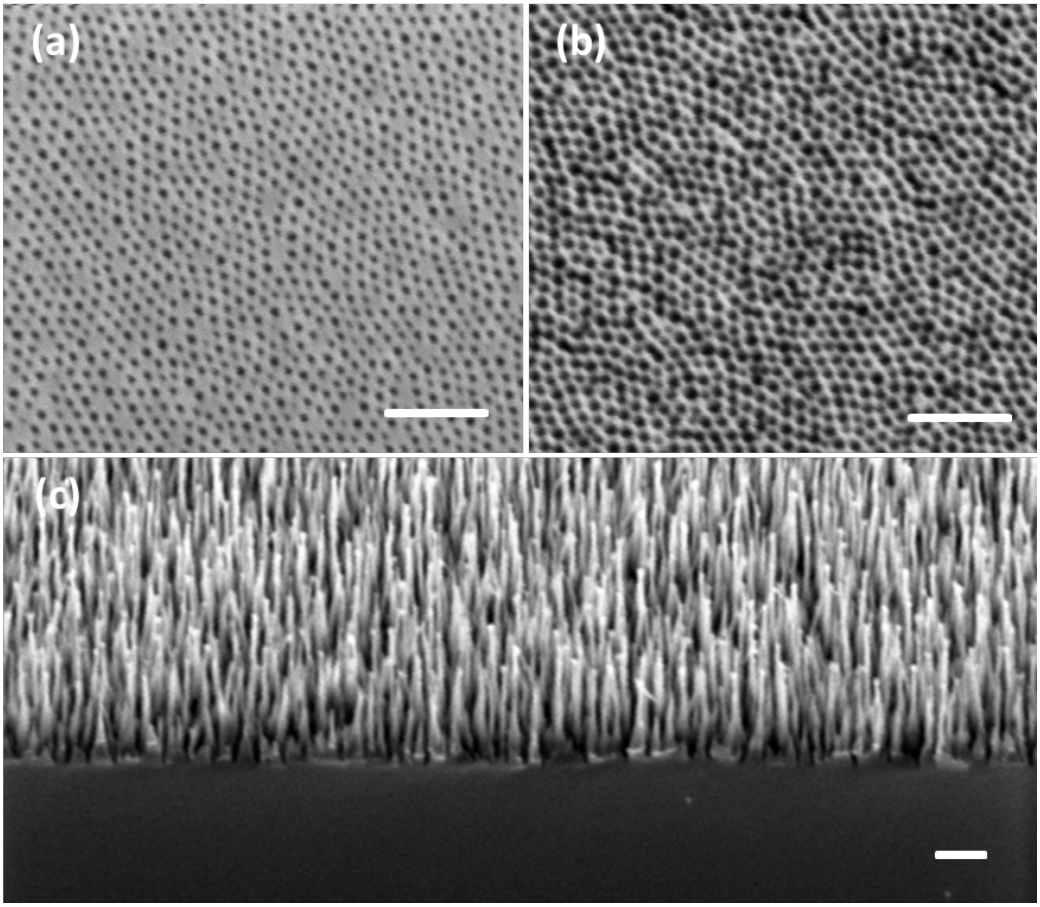

Figure 4.12 Top SEM image of silicon nano-well arrays made by Al_2O_3 hard mask derived from SD39, and etched by chlorine RIE for (a) 200 s and (b) 250 s. (c) Tilted SEM image of silicon nano-pillar arrays made by Al_2O_3 hard mask derived from SD81, etched by chlorine RIE for 450 s. Scale bar: 200 nm.

By changing the etching time of chlorine RIE, the lateral feature size and the etching depth can also be tuned. In Fig. 4.11a,b, it is clear that the holes' diameter increases with the increasing etching time for the silicon nano-wells patterned by SD39. A similar phenomenon is observed as well for the silicon nano-pillars derived from SD81 shown in Fig. 4.12c, as compared to Fig. 4.10a.

4.5 Concluding remarks

In conclusion, an extremely simple and fast BCP nanolithography process has been demonstrated on various substrates with complete coverage over wafer scale. Monolayer packed sphere morphology is kinetically captured during spin-casting using selective solvents for cylindrical SDs, with relatively low size distribution. Due to the high etching contrast between PS and PDMS domain under O_2 RIE, the pattern is successfully created and transferred to the substrates. We also show that by in-situ application of an Al_2O_3 hard mask, high-aspect ratio nanostructured silicon can be fabricated under highly anisotropic chlorine RIE with tunable feature size and depth. This conceptual approach provides a powerful and facile toolset to obtain large-scale nano-patterning on various substrates without any annealing and surface modification process, which are difficult to realize by conventional methods.

4.6 References

1. C. Lu, R. H. Lipson, Interference lithography: a powerful tool for fabricating periodic structures. *Laser Photonics Rev* **4**, 568 (Jul, 2010).
2. C. M. Bates, M. J. Maher, D. W. Janes, C. J. Ellison, C. G. Willson, Block Copolymer Lithography. *Macromolecules* **47**, 2 (Jan 14, 2014).
3. J. Bang, U. Jeong, D. Y. Ryu, T. P. Russell, C. J. Hawker, Block Copolymer Nanolithography: Translation of Molecular Level Control to Nanoscale Patterns. *Adv Mater* **21**, 4769 (Dec 18, 2009).
4. X. D. Gu, I. Gunkel, T. P. Russell, Pattern transfer using block copolymers. *Philos T R Soc A* **371**, (Oct 13, 2013).
5. B. H. Kim, J. Y. Kim, S. O. Kim, Directed self-assembly of block copolymers for universal nanopatterning. *Soft Matter* **9**, 2780 (2013).
6. H. Q. Hu, M. Gopinadhan, C. O. Osuji, Directed self-assembly of block copolymers: a tutorial review of strategies for enabling nanotechnology with soft matter. *Soft Matter* **10**, 3867 (2014).

7. K. Koo, H. Ahn, S. W. Kim, D. Y. Ryu, T. P. Russell, Directed self-assembly of block copolymers in the extreme: guiding microdomains from the small to the large. *Soft Matter* **9**, 9059 (2013).
8. H. C. Kim, T. P. Russell, Ordering in thin films of asymmetric diblock copolymers. *J Polym Sci Pol Phys* **39**, 663 (Mar 15, 2001).
9. C. Sinturel, M. Vayer, M. Morris, M. A. Hillmyer, Solvent Vapor Annealing of Block Polymer Thin Films. *Macromolecules* **46**, 5399 (Jul 23, 2013).
10. P. Mansky, Y. Liu, E. Huang, T. P. Russell, C. J. Hawker, Controlling polymer-surface interactions with random copolymer brushes. *Science* **275**, 1458 (Mar 7, 1997).
11. K. W. Gotrik *et al.*, Morphology Control in Block Copolymer Films Using Mixed Solvent Vapors. *Acs Nano* **6**, 8052 (Sep, 2012).
12. M. S. She, T. Y. Lo, R. M. Ho, Long-Range Ordering of Block Copolymer Cylinders Driven by Combining Thermal Annealing and Substrate Functionalization. *Acs Nano* **7**, 2000 (Mar, 2013).
13. Z. Q. Lin *et al.*, A rapid route to arrays of nanostructures in thin films. *Adv Mater* **14**, 1373 (Oct 2, 2002).
14. S. Kim, R. M. Briber, A. Karim, R. L. Jones, H. C. Kim, Environment-controlled spin coating to rapidly orient microdomains in thin block copolymer films. *Macromolecules* **40**, 4102 (Jun 12, 2007).
15. R. M. Ho *et al.*, Solvent-induced microdomain orientation in polystyrene-b-poly (L-lactide) diblock copolymer thin films for nanopatterning. *Polymer* **46**, 9362 (Oct 24, 2005).
16. W. A. Phillip, M. A. Hillmyer, E. L. Cussler, Cylinder Orientation Mechanism in Block Copolymer Thin Films Upon Solvent Evaporation. *Macromolecules* **43**, 7763 (Sep 28, 2010).
17. M. F. Zhang *et al.*, Highly ordered nanoporous thin films from cleavable polystyrene-block-poly(ethylene oxide). *Adv Mater* **19**, 1571 (Jun 18, 2007).
18. G. Riess, Micellization of block copolymers. *Prog Polym Sci* **28**, 1107 (Jul, 2003).
19. M. Faustini *et al.*, Self-assembled titanium calcium oxide nanopatterns as versatile reactive nanomasks for dry etching lithographic transfer with high selectivity. *Nanoscale* **5**, 984 (2013).
20. J. P. Spatz, S. Sheiko, M. Moller, Substrate-induced lateral micro-phase separation of a diblock copolymer. *Adv Mater* **8**, 513 (Jun, 1996).
21. T. Ghoshal, R. Senthamaraikannan, M. T. Shaw, J. D. Holmes, M. A. Morris, "In situ" hard mask materials: a new methodology for creation of vertical silicon nanopillar and nanowire arrays. *Nanoscale* **4**, 7743 (2012).
22. M. K. Mayeda, J. Hayat, T. H. Epps, J. Lauterbach, Metal oxide arrays from block copolymer thin film templates. *J Mater Chem A* **3**, 7822 (2015).
23. S. Ndoni, P. Jannasch, N. B. Larsen, K. Almdal, Lubricating effect of thin films of styrene-dimethylsiloxane block copolymers. *Langmuir* **15**, 3859 (May 25, 1999).
24. J. W. Jeong, W. I. Park, M. J. Kim, C. A. Ross, Y. S. Jung, Highly Tunable Self-Assembled Nanostructures from a Poly(2-vinylpyridine-b-dimethylsiloxane) Block Copolymer. *Nano Lett* **11**, 4095 (Oct, 2011).
25. T. Y. Lo *et al.*, Phase Transitions of Polystyrene-b-poly(dimethylsiloxane) in Solvents of Varying Selectivity. *Macromolecules* **46**, 7513 (Sep 24, 2013).

26. W. B. Bai *et al.*, Thin Film Morphologies of Bulk-Gyroid Polystyrene-block-polydimethylsiloxane under Solvent Vapor Annealing. *Macromolecules* **47**, 6000 (Sep 9, 2014).
27. J. E. Mark, *Polymer data handbook*. (Oxford University Press, Oxford ; New York, ed. 2nd, 2009), pp. vii, 1250 p.
28. C. L. Yaws, *Thermophysical properties of chemicals and hydrocarbons*. (ed. Second edition., 2014), pp. viii, 991 pages.
29. T. Li, L. Schulte, O. Hansen, S. Ndoni, Nanoporous gyroid TiO2 and SnO2 by melt infiltration of block copolymer templates. *Micropor Mesopor Mat* **210**, 161 (Jul 1, 2015).
30. J. G. Son, K. W. Gotrik, C. A. Ross, High-Aspect-Ratio Perpendicular Orientation of PS-b-PDMS Thin Films under Solvent Annealing. *Acs Macro Lett* **1**, 1279 (Nov, 2012).
31. V. V. Starkov *et al.*, SU8 photoresist as an etch mask for local deep anodic etching of silicon. *Phys Status Solidi A* **197**, 150 (May, 2003).
32. S. M. Kim, S. J. Ku, G. C. Jo, C. H. Bak, J. B. Kim, Fabrication of versatile nanoporous templates with high aspect ratios by incorporation of Si-containing block copolymer into the lithographic bilayer system. *Polymer* **53**, 2283 (May 9, 2012).
33. S. J. Ku *et al.*, Highly ordered freestanding titanium oxide nanotube arrays using Si-containing block copolymer lithography and atomic layer deposition. *Nanotechnology* **24**, (Mar 1, 2013).
34. K. R. Williams, R. S. Muller, Etch rates for micromachining processing. *J Microelectromech S* **5**, 256 (Dec, 1996).
35. Y. C. Tseng *et al.*, Enhanced polymeric lithography resists via sequential infiltration synthesis. *J Mater Chem* **21**, 11722 (2011).
36. Y. C. Tseng, Q. Peng, L. E. Ocola, J. W. Elam, S. B. Darling, Enhanced Block Copolymer Lithography Using Sequential Infiltration Synthesis. *J Phys Chem C* **115**, 17725 (Sep 15, 2011).
37. A. Andreozzi *et al.*, The fabrication of tunable nanoporous oxide surfaces by block copolymer lithography and atomic layer deposition. *Nanotechnology* **22**, (Aug 19, 2011).
38. G. Boulousis, V. Constantoudis, G. Kokkoris, E. Gogolides, Formation and metrology of dual scale nano-morphology on SF(6) plasma etched silicon surfaces. *Nanotechnology* **19**, (Jun 25, 2008).
39. L. Sainiemi, S. Franssila, Mask material effects in cryogenic deep reactive ion etching. *J Vac Sci Technol B* **25**, 801 (May-Jun, 2007).

Chapter 5

Summary and Suggestions for Future Work

5.1 Summary

The detailed and efficient control of materials self-assembly on length scale of nano-meter has been the essential part in the optimization of micro- and nano-technology. There is a considerable scientific and technological challenge to achieve structural materials with sub-20 nanometers. The aim of this thesis is to explore block copolymer self-assembly for functional nano-materials on the scale where the traditional technique is difficult to operate and thus enhance the specific materials properties. Firstly, the unique double gyroid structure makes it ideal for interconnected three-dimensional materials fabrication. The PB-PDMS used in this study has many advantages compared to the BCP reported in the literatures. Due to crosslinking, it is solvent-resistant which allows for a wide variety of chemical precursors infiltration. And it can also be chemically bonded to the substrates. The relatively high thermal stability makes it suitable for ALD process at the optimum deposition temperature. This study shows the great potential of the templating method for novel nano-device manufacture.

Perhaps the most intriguing demonstration of this study is the versatile and facile BCP nanolithography process for nanofabrication. Well-ordered perpendicular cylindrical pattern can form directly on various substrates regardless of their surface energy in an efficient solvent annealing process. Besides that, the remaining oxidized-PDMS mask after oxygen plasma shows excellent pattern transfer properties. This method greatly simplifies the main-stream BCP

lithography methodology. An in-situ alumina hard mask is also demonstrated to give high-aspect—ratio nanostructures. This technique essentially could benefit nearly all nanotechnologies where the small length scale and scalability is important as a facile nanofabrication method.

5.2 Suggestions for Future Work

The demonstrated BCP nanolithography can find numerous applications in next-generation nano-device fabrication. This technique has attracted several research groups at DTU for collaboration at different nanotechnology topics, even though it is freshly new developed. For an example, the nano-patterned graphene provides an ideal platform to study the plasmonic properties. This project is closely co-studied with the group of structured electromagnetic materials lead by Sanshui Xiao.

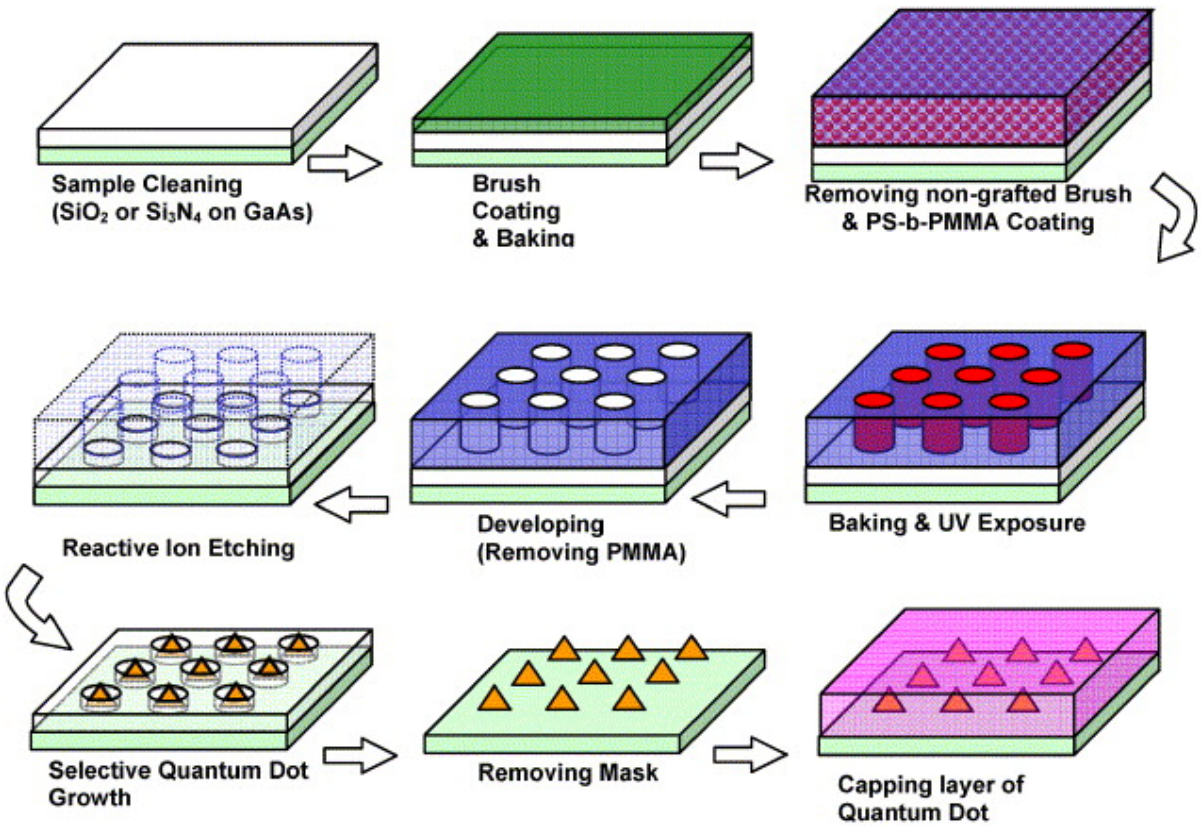

Figure 5.1. Diblock copolymer pattern formation and transfer procedure.(*1*)

Inspired by the work shown in the Fig. 5.1, the research study of quantum dot (QD) epitaxial growth on both indium phosphide (InP) and silicon (Si) based platforms with the aim of creating superior gain material emitting in the 1.5-1.6 μm wavelength range, is collaborated with the group of nano-photonic device. Nanostructures are the key to achieving the set goals. The advantage of this BCP lithography is simple nanofabrication. The development of epitaxial growth technology of III‐V materials on Si combines the benefits of high optical quality III‐V QD gain material with low cost silicon photonics, which is a key platform to push towards increased integration, higher speed and lower energy consumption.

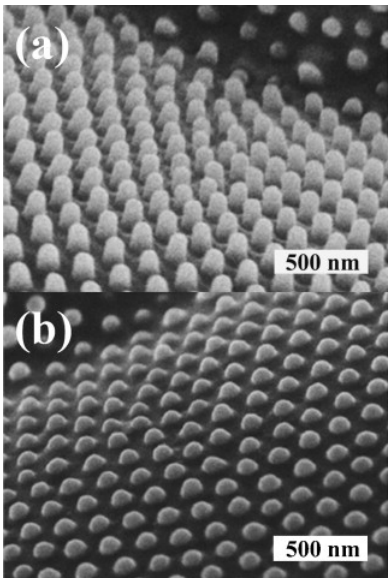

Figure 5.2. Corneal nipple arrays in the Polygonia c-aureum (a) and lycaenid Pseudozizeeria maha (b). (*2*)

The nano-patterned silicon substrates can find many important applications. One example is to be taken as the mold materials for polymer films by injection molding for high-performance anti-reflection and anti-fogging properties (*3*). The periodic anti-reflection surfaces were first discovered in nature while inspecting the eyes of night-flying moths. Scientists have successfully reproduced the moth-eye structures with interference lithographic techniques, precisely fabricating a regular array as shown in Fig. 5.2. On the other hand, recently it was found that such a structure can also provide anti-fogging properties (*4*) .

The high-aspect-ratio silicon nano-pillars can be used as Surface Enhanced Raman Scattering substrates (SERs) as shown in Fig. 5.3 (*5*). The silicon pillar showed in Fig 5.6 can offer much higher density which can greatly increase the Raman signal. This project is currently collaborated with Anja’s group.

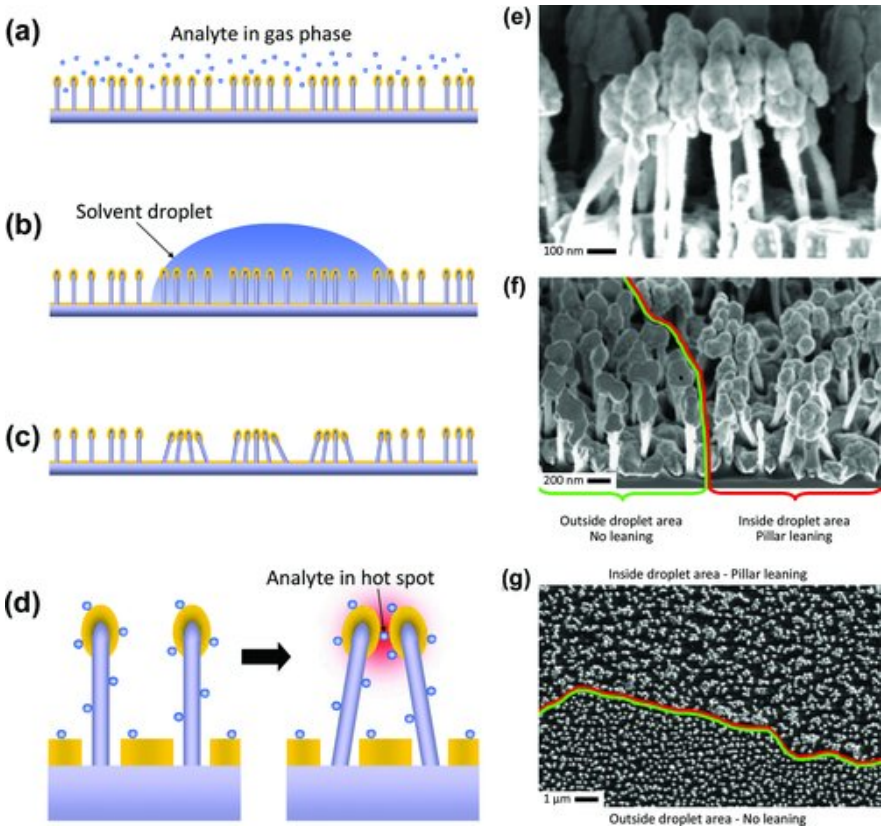

Figure 5.3 Concept of the leaning nanopillar substrate. a)–c), Schematic of the leaning mechanism. d) Schematic of hypothesized enhancement mechanism. When the solvent evaporates, surface tension will pull the silicon nanopillars together, trapping the analyte at the hot spot and giving rise to enhanced Raman signal. e) SEM image of a cluster of leaning silver coated silicon nanopillars. f) Tilted SEM image of the outer perimeter of the evaporated solvent droplet area. The nanopillars to the right have leaned to form hot spots while the nanopillars to the left remain vertical and free standing. g) SEM image of nanopillar surface seen perpendicular to the surface. The line indicates the outer perimeter of the evaporated solvent droplet. Bottom: individual freestanding nanopillars. Top: clusters of nanopillars have formed.(*5*)

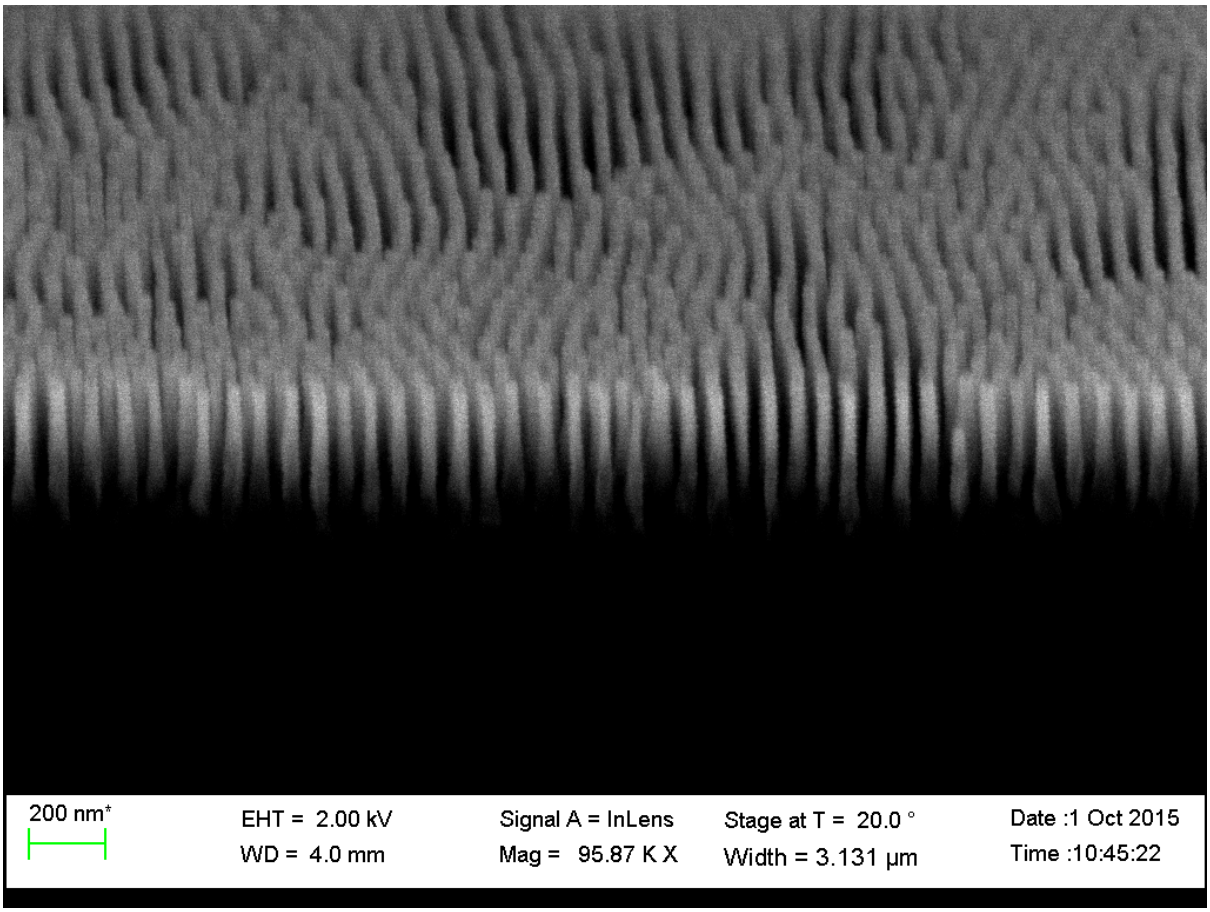

Figure 5.4. SEM image of high-aspect-ratio silicon pillars patterned using the block copolymer lithography introduced in this thesis.

5.3 References

1. J. H. Park *et al.*, Selective MOCVD growth of single-crystal dense GaAs quantum dot array using cylinder-forming diblock copolymers. *J Cryst Growth* **297**, 283 (Dec 29, 2006).
2. D. G. Stavenga, S. Foletti, G. Palasantzas, K. Arikawa, Light on the moth-eye corneal nipple array of butterflies. *P Roy Soc B-Biol Sci* **273**, 661 (Mar 22, 2006).
3. Y. F. Li, J. H. Zhang, B. Yang, Antireflective surfaces based on biomimetic nanopillared arrays. *Nano Today* **5**, 117 (Apr, 2010).
4. Z. Q. Sun *et al.*, Fly-Eye Inspired Superhydrophobic Anti-Fogging Inorganic Nanostructures. *Small* **10**, 3001 (Aug 13, 2014).
5. M. S. Schmidt, J. Hubner, A. Boisen, Large Area Fabrication of Leaning Silicon Nanopillars for Surface Enhanced Raman Spectroscopy. *Adv Mater* **24**, Op11 (Mar 8, 2012).

Appendix A:

http://www.sciencedirect.com/science/article/pii/S1387181115001225

Appendix B:

http://pubs.rsc.org/en/content/articlelanding/2015/nr/c5nr06815k#!divAbstract

Appendix C:

http://pubs.rsc.org/EN/content/articlelanding/2015/ra/c5ra21188c#!divAbstract

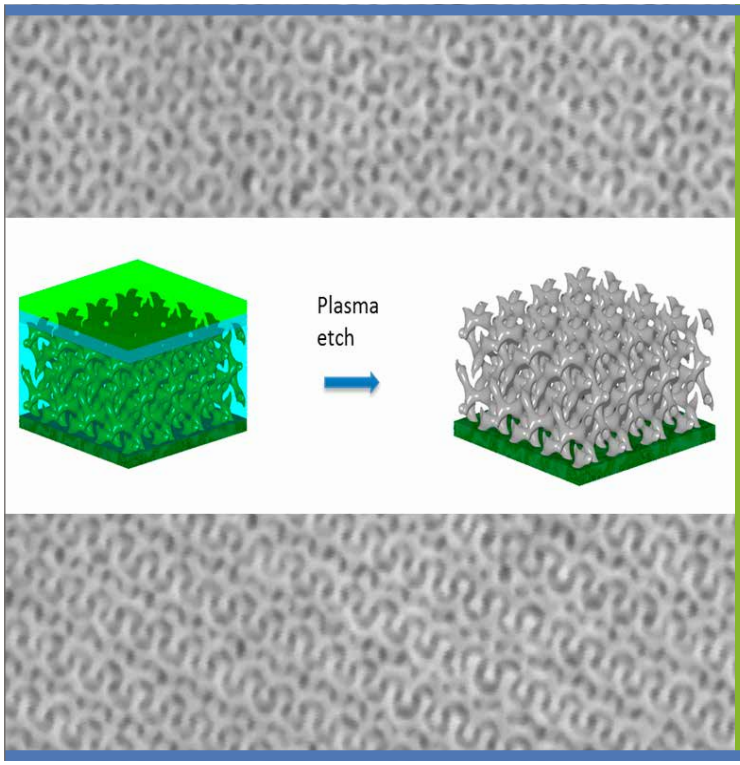

Published by:
DTU Nanotech
Department of Micro- and Nanotechnology
Technical University of Denmark
Ørsteds Plads, building 345B
DK-2800 Kgs. Lyngby